Thesis

# Transport Phenomena and Quantum Phase Transitions in Mesoscopic Systems

Yuji Hamamoto
Department of Physics, University of Tokyo
December, 2009

# Abstract

In this thesis, we study theoretically transport properties of various mesoscopic systems. Our main goal is to reveal dynamic response of a mesoscopic capacitor composed of a quantum dot and a lead, where a unique quantization phenomenon of charge relaxation resistance has been experimentally observed recently. In order to perform nonperturbative analyses of mesoscopic systemst, we demonstrate the path-integral Monte Carlo (PIMC) simulations using the cluster algorithm. Three target systems are considered. The first one is the single impurity problem in a Tomonaga-Luttinger liquid with spin degeneracy, to which we demonstrated the performance of the PIMC method. By analyzing the low-temperature behavior of the charge and spin conductances, we identify the phase diagram for an intermediate impurity strength. We compare our results with the previous results of the standard perturbative renormalization group for weak and strong impurity backscatterings. Next we consider a large quantum dot connected to a bulk lead by a single mode point contact. We extend the cluster algorithm so that it takes into account the charging effect and analyze the Coulomb blockade phenomena in the quantum dot. By means of the PIMC method, we verify the theoretical prediction that the capacitance diverges logarithmically due to the two-channel Kondo effect at charge degeneracy points for arbitrary dot-lead connection. Finally, we tackle the dynamic response of a mesoscopic capacitor, where both transport and Coulomb blockade are important for the quantization of the charge relaxation resistance. By means of perturbation theory, renormalization group technique, and the path-integral Monte Carlo method, the charge relaxation resistance is evaluated in the whole range of dot-lead coupling. We predict that the charge relaxation resistance is universal even in the presence of strong Coulomb blockade for the Luttinger parameter $K > 1/2$, while the Kosterlitz-Thouless transition dramatically influences the universal nature of the charge relaxation resistance for $K < 1/2$.

# Acknowledgements

I am deeply grateful to Prof. Takeo Kato whose comments and suggestions were innumerably valuable throughout the course of my study. I would also like to thank Takeshi Matsuo who helped me to learn the path-integral Monte Carlo method. Special thanks go to Ken-Ichiro Imura who taught me the impurity problems in Tomonaga-Luttinger liquids and also gave me warm encouragements. I am also indebt to Yasuhiro Utsumi whose comments made enormous contribution to my understanding of Coulomb blockade in open quantum dots. I would like to give heartful thanks to Prof. Kensuke Kobayashi who introduced me to the fertile field in mesoscopic physics, i.e., dynamical transport in mesoscopic systems. I also wish to acknowledge to Prof. Thierry Martin and Thibaut Jonckheere for their long-term collaborations and invaluable discussions in the course of our study on dynamic response of mesoscopic capacitors. I am sincerely grateful to Tatsuya Fujii for insightful comments on the renormalization group approach. My thanks go to all the people of Institute for Solid State Physics, University of Tokyo. In particular, I would like to thank my colleagues, Tomohiro Otsuka, Yasuyuki Kato, Toshihiro Sato, and Shunsuke Kirino, and the members of Kato Group, Kazuyoshi Yoshimi, Hiroshi Shinaoka, Itofumi Takeuchi, Emi Yukawa, Eiki Iyoda, and Noritaka Tamura for great discussion on physics and fun time. I am also indebt to Hiroko Eguchi whose efforts in cumbersome paperwork enabled me to focus on my study. I would also like to express my gratitude to my family for their moral support and warm encouragements.

Finally, I acknowledge the financial support of the Japan Society for the Promotion of Science (JSPS) that made it possible to complete my thesis. The computation in this thesis was done using the facilities of the Supercomputer Center, Institute for Solid State Physics, University of Tokyo.

# Contents

# Chapter 1

# Introduction

## 1.1 Motivation

Recent nanofabrication techniques allow researchers to confine electrons in low-dimensional structures with nano scale such as quantum wires and quantum dots. These nanostructures are called mesoscopic systems and have been studied energetically both by experimentalists and theorists ever since 1980's. In early studies, quantum coherence of electrons and quantum-classical crossover at intermediate length scale were of central interest [1, 2, 3]. Nowadays, one can design nanostructures as needed and actively control the quantum-mechanical states of inside electrons. Indeed there are a number of experiments which demonstrate coherent manipulation of electronic states in various systems [4]. Reflecting the high controllability, there is growing interest in the application of the nanostructurs to quantum information in recent years [5].

Among the nanostructures experimentally realizable, quantum dot systems provide attractive playgrounds for researchers, since they have several advantages in application to quantum information technologies. For example, the quantum bit (qubit) is an essential building block for quantum computation and can be realized as superposition of, e.g., different charge (or spin) states in a quantum dot. One can manipulate dynamically the qubits thus obtained by controlling parameters such as a gate voltage, a source-drain bias, and an external magnetic field. Recently one-qubit [6] and two-qubit [7] operations have been demonstrated in double quantum dot systems. From the viewpoint of quantum communication, on the other hand, the coherent single-electron source fabricated in a quantum dot system [8] is another promissing candidate for the application. The creation of a single-electron source is expected to be simpler than a single-photon source because of Fermi statistics and Coulomb interaction.

Toward future developments in rapid manipulation of quantum dot systems, it

is highly demanded to reveal *dynamical* properties of *coherent* transport phenomena. Despite the long history of mesoscopic physics, it is only quite recent that experiments on dynamical transport in the coherent regime have become possible. One of the simplest examples is the measurement of GHz-frequency response of a mesoscopic capacitor, which is composed of a quantum dot and a lead [9]. Surprisingly, dynamical resistance through a quantum point contact (QPC) is quantized at $h/2e^2$, which is independent of transparency of the QPC. This behavior is utterly different from that for the dc resistance determined by the Landauer-Büttiker formula [10, 11, 12], which explicitly depends on the transmission probability. Thus, in the coherent regime, even the simplest case provides a challenging problem leading to a counterintuitive result.

To understand the dynamical properties of the mesoscopic systems, one should also take into account the fact that transport phenomena in nanostructures are frequently affected by interactions between electrons. For example, in a small quantum dot, the cost of charging energy suppresses electron transmission and ensures a well-defined electron number in the dot, which is called Coulomb blockade [13]. On the other hand, an interacting electron system confined one-dimensionally is a Tomonaga-Luttinger liquid at low temperature and exhibits characteristic transport properties [14, 15, 16, 17]. It is also well-known that in a quantum dot system conduction electrons in the lead and a localized electron in the dot form a spin-singlet ground state below a characteristic temperature, which is called the Kondo effect. So far, these many-body effects have been investigated mainly in the static or dc case. However little is known about how electron interactions modify the dynamical transport in the coherent regime.

Motivated by the circumstances mentioned above, we in this thesis aim to reveal the dynamical properties of a mesoscopic capacitor in the presence of strong electron interactions. Especially, we are interested in the regime with sufficiently large transmission, where electronic transport is expected to be phase-coherent. In order to investigate the intermediate regime, which is in general difficult to treat analytically, we employ the path-Integral Monte Carlo (PIMC) method. The PIMC method has become applicable to such an intermediate region thanks to the cluster algorithm, which has been recently developed in the context of resistively shunted Josephson junctions by Werner and Troyer [18]. In Chap. 3, we extend their algorithm to an incoherent quantum dot with spinful electrons and analyze the static property, or the capacitance. In Chap. 4, we apply the PIMC simulation to dynamic response in a mesoscopic capacitor and display our main results.

In the rest of this chapter, we first review theoretical studies of dynamical resistance in the coherent regime, as well as the recent experiment of the ac responses in a quantum dot in Sec. 1.2. Problems left unsolved on the dynamical responses in nanostructures are also summarized. In Sec. 1.3, we briefly review the known many-body effects. Finally, we describe the contents of this thesis in Sec. 1.4.

## 1.2 ac transport in a mesoscopic capacitor

To make the problem clearer, let us first review prior studies on the dynamical response of a mesoscopic system. The system we have in mind is a coherent quantum dot, also referred to as a mesosocpic capacitor, depicted in the left panel of Fig. 1.1. The dot is connected to the lead via a $M$-channel quantum point contact (QPC) and is capacitively coupled to a gate voltage. One way of characterizing the transport properties of such a system is to apply an oscillating gate voltage and measuring the resistance through the QPC. One can introduce $RC$ time $\tau_{RC}$ by analogy to the classical $RC$ circuit. If one denotes the resistance through the QPC by $R_q$ and the capacitance of the dot by $C_\mu$, the charge relaxation time of the mesoscopic capacitor reads $\tau_{RC} = 1/R_q C_\mu$. It is clear from the circuit equation that the admittance of the mesoscopic capacitor can be expanded at low-frequency regime $\omega \ll 1/\tau_{RC}$ as

$$G(\omega) = \left( R_q + \frac{1}{-i\omega_n C_\mu} \right)^{-1} \simeq -i\omega C_\mu + \omega^2 {C_\mu}^2 R_q + O(\omega^3). \tag{1.1}$$

The quantum resistance $R_q$ appearing in the quadratic term in $\omega$ is referred to as *charge relaxation resistance*. In their pioneering works [19, 20], Büttiker *et al.* have applied the self-consistent scattering theory to the mesoscopic capacitor and derived a low-frequency expansion similar to Eq. (1.1). The charging effect in the dot is taken into account through an internal effective potential determined self-consistently. The charge relaxation resistance thus obtained is represented as

$$R_q = \frac{h}{2e^2} \frac{\int \mathrm{d}E(-\mathrm{d}f/\mathrm{d}E)\mathrm{Tr}[\mathbf{S}^\dagger(E)\partial\mathbf{S}(E)/\partial E]^2}{\{\int \mathrm{d}E(-\mathrm{d}f/\mathrm{d}E)\mathrm{Tr}[\mathbf{S}^\dagger(E)\partial\mathbf{S}(E)/\partial E]\}^2}, \tag{1.2}$$

where $\mathbf{S}$ denotes a $M \times M$ scattering matrix. Surprisingly enough, the charge relaxation resistance for a single channel ($M = 1$) is quantized at $R_q = h/2e^2$ at

Figure 1.1: (left) Schematic figure of a mesoscopic capacitor. (right) Charge relaxation resistance as a function of the gate voltage on the point contact $V_G$. Taken from Ref. [9].

zero temperature. The quantization of the charge relaxation resistance essentially differs from the quantized dc resistance in quantum wires and (integer) quantum Hall edges in two points. The quantized value of $R_q$ per channel equals half a resistance quantum $h/2e^2$; clearly, the factor 1/2 in the quantized value has nothing to do with spin degeneracy. More importantly, the quantized resistance is achieved irrespective of transmission through the QPC or the gate voltage, due to cancellation of the scattering matrices at $T = 0$. These two peculiarities suggest breakdown of the Kirchhoff's law in the quantum $RC$ circuit at low frequencies $\omega \ll 1/\tau_{RC}$ in the sense that the impedance of the quantum resistor, i.e., QPC is not given by its dc resistance.

Although the above theory was presented more than a decade ago, recently there has been a renewed interest in the quantized charge relaxation resistance owing to the progress in experimental techniques in the ac regime. Gabelli *et al*. has experimentally confirmed the theoretical prediction by measuring charge relaxation resistance of a mesoscopic capacitor shown in the left panel of Fig. 1.1 [9]. The mesoscopic capacitor is realized electrostatically in a two-dimensional electron gas (2DEG). A magnetic field $B = 1.3$ T is applied perpendicular to the 2DEG, so that integer Hall edge states are realized along the edge of the system. The QPC voltage $V_G$ controls transmission through the QPC and in the present case only a single mode is transmitted. The gate voltage in the dot oscillates with frequency $\omega \sim 1$ GHz, which is sufficiently small compared to the inverse $RC$ time $1/\tau_{RC} \sim 100$ GHz. Thus one can expect that charge relaxation condition $\omega \ll 1/\tau_{RC}$ is guaranteed in this frequency regime. Note that the frequency $\omega$ should be larger than the temperature experimentally achievable $\sim 1$ GHz, otherwise the observed quantity would be smeared out by thermal fluctuations. It is clear from the circuit equation $Z = R_q + 1/(-i\omega C_\mu)$ that in experiments $R_q$ can be obtained as the real part of impedance $Z$. In the right panel of Fig. 1.1, the charge relaxation resistance, or $\mathrm{Re}(Z)$, is shown as a function the QPC gate voltage $V_G$. The data is roughly equal to $h/2e^2$ in consistency with the theory, at least for large $V_G$ (weak reflection). Note that the abrupt increase in $R_q$ for small $V_G$ indicates pinch-off of the transmission channel.

Stimulated by the experimental realization of the quantized charge relaxation resistance, Nigg *et al.* have developed a more realistic theory based on a tunnel Hamiltonian [21]. In their theory, the charging effect in the quantum dot is treated within the Hartree-Fock approximation. $R_q$ calculated in the low-frequency limit $\omega \ll 1/\tau_{RC}$ is again quantized at $h/2e^2$. The charge relaxation resistance seems to be robust even in the presence of the charging effect, judging from the results in Refs. [19, 21]. However, it should be noted that these results are obtained based on mean-field-type approximations and are valid only when the charge fluctuation is small. This suggests that on the degeneracy points, where two neighboring charge states, e.g., $Q = ne$ and $Q = (n + 1)e$ (with an integer $n$) are degenerate,

large charge fluctuations may modify the dynamical properties of the mesoscopic capacitor. Indeed, it has been predicted that in incoherent quantum dots the ground state on the degeneracy points are drastically affected by the Kondo effect due to pseudo spin both in the weak and strong coupling limits [22, 23]. Then a question arises; is the charge relaxation resistance still quantized even in the presence of the Kondo physics? This is the topic in Chap. 4 and we see that the Kondo physics is the key to understanding the dynamic resistance on the degeneracy points.

## 1.3 Electron interactions in mesoscopic systems

Electrons confined in low-dimensional structures with nano scale are subject to strong electron interactions. In this section, we give a few examples of interaction related to the problems in Chap. 3 and Chap. 4, and describe how each interaction influences the transport phenomena.

### 1.3.1 Tomonaga-Luttinger liquid

In one-dimensional (1D) electron systems the usual Fermi liquid behavior is destroyed by the interaction between electrons. As a consequence, low-energy excitations in the interacting 1D electron system are density fluctuations of charge and spin modes, and the ground state is called a Tomonaga-Luttinger liquid (TLL) [14, 15, 16, 17]. The peculiar behaviors of a TLL are experimentally observed in fractional quantum Hall edges [24, 25, 26] and single-wall carbon nanotubes [27, 28, 29]. Conventionally, a TLL is formulated with the bosonization method as follows. For simplicity, we here consider the spinless case. If the dispersion relation is linearized around the Fermi level at low temperatures, the Hamiltonian for free electrons reads

$$H_{\text{free}} = v_F \sum_{r=\pm} \sum_{k} (rk - k_F) {c_{r,k}}^{\dagger} c_{r,k}, \tag{1.3}$$

where $c_{\pm,k}$ is the annihilation operator for an electron with momentum $k$ moving in the $\pm x$ direction. Due to the two branches of linear dispersion in Eq. (1.3), charge and current fluctuations behave as bosonic operators. Then, one can express the Hamiltonian for the interacting 1D electron system in the quadratic form

$$H_0 = \int \frac{\mathrm{d}x}{2\pi} \left[ \frac{u}{K} \left( \frac{\partial \phi}{\partial x} \right)^2 + uK \left( \frac{\partial \theta}{\partial x} \right)^2 \right], \tag{1.4}$$

where $\phi$ and $\theta$ are canonically conjugated bosonic fields satisfying the commutation relation

$$[\phi(x), \theta(x')] = \frac{i\pi}{2} \mathrm{sgn}(x - x'). \tag{1.5}$$

$u \equiv v_F/K$ is the sound velocity, and $K$ is a positive parameter describing (short-range) interactions between electrons:

$$\begin{cases} K < 1 & \text{repulsive} \\ K = 1 & \text{noninteracting} \\ K > 1 & \text{attractive.} \end{cases} \tag{1.6}$$

Eq. (1.4) is obviously the Hamiltonian for an elastic string, which allows us to calculate exactly various correlation functions. For example, we can calculate the two point correlation function $\langle\phi(x_1,\tau)\phi(x_2,0)\rangle$ in the imaginary-time representation to estimate dc conductance between $x_1$ and $x_2$

$$G(x_1,x_2) = \lim_{i\omega_n\to 0} \frac{e^2}{h}\frac{2|\omega_n|}{\pi}\int_0^\beta d\tau\langle\phi(x_1,\tau)\phi(x_2,0)\rangle e^{i\omega_n\tau} = \frac{e^2}{h}K. \tag{1.7}$$

Thus the interaction parameter $K$ can be also regarded as dimensionless conductance of a homogeneous TLL. Note that the factor $K$ reflects interactions in the leads ($x < x_1, x_2 < x$) not in the wire ($x_1 < x < x_2$). This can be seen by replacing the TLL leads ($K \neq 1$) with Fermi-liquid leads ($K = 1$), i.e.,

$$K(x) = \begin{cases} K_L = 1 & x < x_1, x_2 < x \\ K_W \neq 1 & x_1 < x < x_2. \end{cases} \tag{1.8}$$

The conductance for the inhomogeneous interactions (1.8) is calculated [30] as

$$G = \frac{e^2}{h}K_L = \frac{e^2}{h} \tag{1.9}$$

and recovers the Landauer's formula without scatterers.

The transport property of a TLL is dramatically modified by introducing scatterers such as nonmagnetic impurities or single-mode point contacts [31, 32, 33, 34]. For example, if a local scatter with barrier height $V_0$ is introduced at the origin $x = 0$ [31], the Hamiltonian describing an electron reflected by the scatterer reads

$$H_V = -V_0[{\psi_+}^\dagger(x=0)\psi_-(x=0) + \text{H.c.}] = -V\cos[2\phi(x=0)]. \tag{1.10}$$

where the reflection strength $V \propto V_0$. Noticing the fact that the total Hamiltonian $H_0 + H_V$ is quadratic in $\phi(x \neq 0)$'s, one can integrate out these fields away from the origin to derive an effective action

$$S = \frac{1}{\pi K\beta}\sum_{\omega_n}|\omega_n||\tilde{\phi}(\omega_n)|^2 - V\int d\tau\cos[2\phi(\tau)], \tag{1.11}$$

where $\phi(\tau) \equiv \phi(x = 0, \tau)$ and $\tilde{\phi}(\omega_n)$ is the Fourier transform of $\phi(\tau)$. One can also start from a fractional quantum Hall edge state and derive the same model, where $K$ is replaced with the filling factor $\nu = 1/m$ with an odd integer $m$. The perturbative renormalization group (RG) [35] is a useful technique to analyze the ground state of the single-impurity problem (1.11) for small $V$. By integrating out high-frequency modes, one obtains the scaling equations

$$\frac{\mathrm{d}V_n}{\mathrm{d}l} = (1 - n^2 K)V_n \qquad (V_1 \equiv V), \tag{1.12}$$

where $V_n$ denotes reflection strength associated with the $n$th-order scattering process, and $\mathrm{d}l = -\mathrm{d}D/D$ with the bandwidth $D$. It is clear from Eq. (1.12) that, as the energy is lowered, at least $V_1$ grows if $K < 1$, while all the $V_n$'s decay to zero if $K > 1$. A similar RG treatment is possible by taking the strong scatterer limit as the starting point. In this case, two semi-infinite TLLs are connected via a weak link with tunneling strength $t$, and the RG equation for $n$th-order tunneling process reads

$$\frac{\mathrm{d}t_n}{\mathrm{d}l} = \left(1 - \frac{n^2}{K}\right) t_n \qquad (t_1 \equiv t). \tag{1.13}$$

This equation means that, as the energy is lowered, at least $t_1$ grows if $K > 1$, while all the $t_n$'s decay to zero if $K < 1$. The results of the RG equations (1.12) and (1.13) are summarized in the left panel of Fig. 1.2. For repulsive interactions $K < 1$, electrons are perfectly reflected by the scatterer at $T = 0$ (insulator phase); for attractive interactions $K > 1$, electrons are perfectly transmitted through the scatterer at $T = 0$ (conductor phase).

Although the RG equations (1.12) and (1.13) are applicable only in the limits $V \to 0$ and $t \to 0$, respectively, the above discussion has been verified in the nonperturbative regime based on the path-integral Monte Carlo method [36]. Moreover, $H_0 + H_V$ is equivalent to the boundary sine-Gordon model and therefore is exactly solvable by means of the thermodynamic Bethe Ansatz [37]. Experiments in the fractional quantum Hall regime at filling $\nu = 1/3$ have also turned out to support the above theory as shown in the right panel of Fig. 1.2.

### 1.3.2 The Coulomb blockade effect

In a quantum dot system with small geometrical capacitance $C_g$, tunneling of electrons between the dot and a lead is in general exponentially suppressed by the charging energy at low temperatures. This phenomenon is called the Coulomb blockade. Since the electrostatic energy of the quantum dot system is given by

$$H_C = \frac{Q^2}{2C_g} + QV_g, \tag{1.14}$$

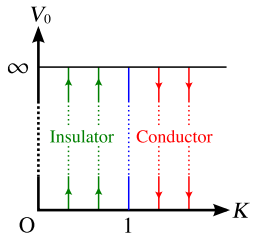


Figure 1.2: (left) Schematic flow diagram for the single-impurity problem in an interacting 1D electron system. The ground state is an insulator for repulsive interactions ($K < 1$), while it is a perfect conductor for attractive interactions ($K > 1$). (right) Temperature dependence of conductance through a point contact in the fractional quantum Hall regime with filling $\nu = 1/3$. The scaling behavior $G \propto T^4$ is in good agreement with theoretical prediction $G \propto T^{2/\nu-2}$ [See Eq. 1.13]. Taken from Ref. [24].

where $Q$ is the dot charge and $V_g$ is the gate voltage, the charge state in the dot is controlled by tuning $V_g$. Especially, when $V_g$ is tuned to a point where two neighboring charge states $Q = en$ and $Q = e(n + 1)$ are degenerate, the cost of the electrostatic energy vanishes. Therefore, one observes periodic peaks of conductance through the quantum dot as a function of $V_g$.

Electron transport in the Coulomb blockade regime has been studied theoretically in many literatures, most of which have dealt with weak tunneling of electrons between leads and a quantum dot [38]. Electron transport is then described by a classical master equation with tunneling rates for various processes, where quantum coherence of electrons is not maintained during the tunneling events. In this sense, such a transport is regarded as *incoherent*, although the transition rate itself is determined by quantum tunneling through a quantum point contact (QPC) between a lead and a dot.

If it is possible to suppress backward scattering on the QPC adjusting its gate voltage, one needs to consider strong quantum fluctuation due to electron transfer between a lead and a dot. Such a situation, called the strong tunneling regime, cannot be treated with the conventional theory based on the rate equation. Strong tunneling has been studied theoretically by Matveev [23] based on a simple model of a quantum dot coupled to a lead through a point contact as shown in the left panel of Fig. 1.3. Since electron transport in this system is governed mainly by a single transmission channel near the point contact, Matveev has considered a simple one-dimensional model. For a spinless electron system, the Hamiltonian is written as

$$H = H_{\rm kin} + H_V + H_C \tag{1.15}$$

$$H_{\rm kin} = v_F \int_{-\infty}^{L} {\rm d}x[{\psi_+}^\dagger(x)(i\nabla - k_F)\psi_+(x) + {\psi_-}^\dagger(x)(-i\nabla - k_F)\phi_-(x)], \tag{1.16}$$

$$H_V = \int_{-\infty}^{L} {\rm d}x V(x)[{\psi_+}^\dagger(x) + {\psi_-}^\dagger(x)][\psi_+(x) + \psi_-(x)], \tag{1.17}$$

$$H_C = \frac{(Q - eN_g)^2}{2C_g}, \quad Q = e\int_0^L {\rm d}x[{\psi_+}^\dagger(x)\psi_+(x) + {\psi_-}^\dagger(x)\psi_-(x)]. \tag{1.18}$$

Here, $H_{\rm kin}$ describes a kinetic energy for the right-(left-)going electrons denoted by $\psi_+(x)$ [$\psi_-(x)$]. The potential energy term $H_V$ describes the effect of the energy barrier $V(x)$ near the point contact, and $H_C$ is the charging energy for a quantum dot with a size $L$. In this model, short-range interactions are neglected by assuming that they are well screened by other electrons outside the transmission channel; only the long-range Coulomb interaction is taken into account through the charging energy $H_C$. For further analysis, we take a delta-function-type potential ($V(x) = V_0\delta(x)$) at the origin, and apply the bosonization method to the present model. The bosonized Hamiltonian for a sufficiently large quantum dot ($L \to \infty$) is given by

$$H_{\rm kin} = \int \frac{{\rm d}x}{4\pi}\left[u\left(\frac{\partial\phi}{\partial x}\right)^2 + u\left(\frac{\partial\theta}{\partial x}\right)^2\right], \tag{1.19}$$

$$H_V = V\cos[2\phi(x=0)], \tag{1.20}$$

$$H_C = \frac{1}{\pi^2}E_C[\phi(x=0) - \pi N_g]^2, \tag{1.21}$$

where $V = V_0 D/\pi v_F$, and $D$ is the bandwidth. Thus, the bononization approach has an advantage that the charging energy is easily formulated in terms of bosonic fields.

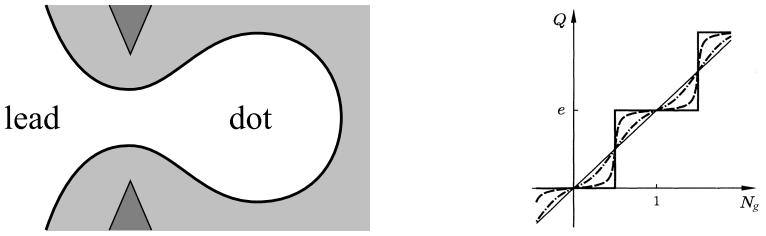


Figure 1.3: (left) Simple quantum dot system composed a dot and a lead. (right) Coulomb blockade of the dot charge $Q$.

In Ref. [23], Matveev has studied the behavior of a quantum dot with strong tunneling by means of the perturbative calculation with respect to the potential barrier $V$. His result is summarized as follows. For $V = 0$, the charge $Q = e\langle\phi\rangle/\pi$ is proportional to the gate voltage $N_g$ as shown with the straight line in the right panel of Fig. 1.3. As $V$ increases gradually from zero, the $V_g$-$Q$ curve starts to oscillate slightly around the straight line. For larger $V$, electron transfer is governed by weak tunneling processes, and the well-known step-like dependence called the Coulomb staircase is recovered. In Chap. 4 of this thesis, the ac response of a quantum dot system with a *finite* length $L$ is studied by formulating the effective action in a similar way based on the bosonization method.

In addition to the spinless case, Matveev has also considered the spin degree of freedom both in the weak- and strong-tunneling limits and has found that the low-energy transport properties are governed by the two-channel Kondo effect due to a pseudo spin [22, 23]. In Chap. 3 of this thesis, we consider the same problem in the intermediate region by means of the path-integral Monte Carlo method.

### 1.3.3 The Kondo effect

How localized electrons interact with delocalized electrons is a central question to many problems in solid-state physics. The simplest manifestation of this situation is the Kondo effect, which occurs when a magnetic impurity is placed in a metal [39, 40]. Nowadays, it is well known that a spin-singlet state is formed between the localized electron with a spin and conduction electrons near the Fermi energy, below a characteristic temperature called the Kondo temperature. The formation of the Kondo singlet state was theoretically predicted also for quantum dot systems [41, 42], and has been examined experimentally through electron transport [43, 44]. The coherent ac transport of quantum dots in presence of the Kondo effect for real spins is an attracting problem, although it is out of the scope of this thesis.

The essence of the Kondo effect can be studied with the Kondo Hamiltonian written as

$$H_K = \sum_{k,\sigma} v_F k c^\dagger_{k,\sigma} c_{k,\sigma} + \frac{J_\parallel}{4}\sigma_z(c_\uparrow{}^\dagger c_\uparrow - c_\downarrow{}^\dagger c_\downarrow) + \frac{J_\perp}{2}\left(\sigma_+ c_\downarrow{}^\dagger c_\uparrow + \sigma_- c_\uparrow{}^\dagger c_\downarrow\right). \quad (1.22)$$

Here, $v_F$ is the Fermi velocity, $c_{k,\sigma}$ is an annihilation operator of a conduction electron, and $c_\sigma = L^{-1/2}\sum_k c_{k,\sigma}$ is the Wannier operator of the conduction electron at the impurity site. The conduction electrons interact with the localized spin $\boldsymbol{S} = \boldsymbol{\sigma}/2$, through the exchange couplings, $J_\parallel$ and $J_\perp$. The $J_\parallel$ term describes the scattering process where the spin polarization is unchanged, while the $J_\perp$ term describes spin-flip scattering. The Kondo effect for real spins corresponds to the

isotropic case ($J_\perp = J_\parallel$) due to the SU(2) symmetry, while the charge-Kondo effect is described by the above Hamiltonian with spin anisotropy ($J_\perp \neq J_\parallel$).

A simple approach to examine the formation of the spin-singlet state in the Kondo model is the poor-man's scaling [45]. Here, we review a more sophisticated scaling approach, which gives the same renormalization group equations [46, 47]. The partition function for the impurity in the instanton-gas representation is derived from the Kondo model as

$$Z_K = \sum_{m=0}^{\infty} \left(\frac{\rho J_\perp}{2\tau_c}\right)^{2m} \int_0^\beta \mathrm{d}\tau_{2m} \int_0^{\tau_{2m}} \mathrm{d}\tau_{2m-1} \cdots \int_0^{\tau_2} \mathrm{d}\tau_1 \times \exp\left[(2-\bar{\varepsilon}) \sum_{j>k}^{2m} (-1)^{j+k} \log \frac{\tau_j - \tau_k}{\tau_c}\right], \tag{1.23}$$

where the condition $\tau_{j+1} - \tau_j > \tau_c$ with the short-time cutoff $\tau_c$ is assumed. The phase factor $\bar{\varepsilon}$ is related to $J_\parallel$ as $\bar{\varepsilon} = 2\rho J_\parallel$ up to the first order in $J_\parallel$, where $\rho = (2\pi v_F)^{-1}$ is the density of states of conduction electrons. If we change the cutoff from $\tau_c$ to $\tau_c + \mathrm{d}\tau_c$, i.e., if we carry out a partial integration of high-energy degrees of freedom such that the the partition function remains invariant, we obtain a set of differential equations describing the scaling behavior of each parameter. Up to second order in $\rho J_\parallel$ these scaling equations are given by

$$\frac{\mathrm{d}\bar{\varepsilon}}{\mathrm{d}l} = (2-\bar{\varepsilon})(\rho J_\perp)^2, \tag{1.24}$$

$$\frac{\mathrm{d}\rho J_\perp}{\mathrm{d}l} = \frac{\bar{\varepsilon}}{2}\rho J_\perp, \tag{1.25}$$

where $\mathrm{d}l = -\mathrm{d}D/D$ with the bandwidth $D$. The behavior of these equations are understood by plotting the scaling trajectories in the $\bar{\varepsilon}$-($\rho J_\perp$) plane as shown in Fig. 1.4. The trajectories are classified into two types of flow; one is toward the weak coupling $J_\perp \to 0$, and the other is toward the strong coupling $J_\perp \to \infty$. The former reaches one of the ferromagnetic Kondo fixed points (line) at zero temperature, while the latter to the antiferromagnetic Kondo fixed point. In the former case, the ground state is doublet due to the spin degeneracy, and the spin-flip process is completely suppressed at zero temperature. In the latter case, the Kondo singlet between the localized spin and the conduction electrons is formed below the Kondo temperature $T_K \sim \tau_c^{-1} \exp(-1/\rho J_\perp)$. In Chap. 4, we will see that the difference between the ferro- and antiferro-magnetic Kondo fixed points is essential to the understanding of interaction effect on the dynamic response of a mesoscopic capacitor.

We note that the above discussion is closely related to the problem of dissipative quantum effects. For the dissipative two-state system, the corresponding

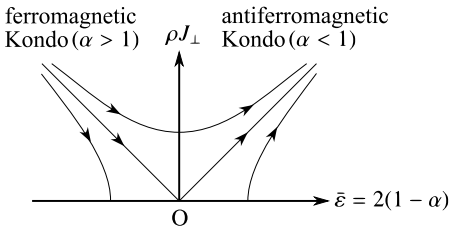


Figure 1.4: The scaling trajectories of $(\bar{\varepsilon}, \rho J_\perp)$.

partition function can be written in the form similar to Eq. (1.23), and the localization transition of a quantum Brownian particle subject to a double-well potential has been discussed theoretically in Refs [48, 49, 50]. Dynamics in this system has been studied theoretically with the Monte Carlo method [51, 52], the numerical renormalization group calculation [53, 54], and an analytical approach [55].

## 1.4 Contents

This thesis is organized as follows. In Chap. 2, we first explain in detail the path-integral Monte Carlo method employed in this thesis. We demonstrate its performance by applying it to a simple example of the dc transport through an impurity located in a spinful Tomonaga-Luttinger liquid. In Chap. 3, we extend the PIMC method to investigate the Coulomb blockade in quantum dot systems. In Chap. 4, which is the main part of this thesis, we discuss dynamic response of a mesoscopic capacitor in the presence of electron interactions.

# Chapter 2

# Path-Integral Monte Carlo Method

In order to study the non-perturbative regions of the models treated in this thesis, we perform numerical simulations based on the path-integral Monte Carlo method (PIMC). For efficient Monte Carlo sampling, it is important to adopt intelligent algorithms optimized for each model. In this chapter, we first illustrate our update scheme taking the impurity problem in a spinless Tomonaga-Luttinger liquid (TLL) as an example. To demonstrate performance of the PIMC method, we actually apply the PIMC simulation to the impurity problem in a *spinful* TLL. By analyzing the low-temperature behavior of the conductances, we identified four distinct phases characterized by either perfect transmission or reflection of charge and spin channels for an intermediate scattering strength. We compare our results with the previous results of the standard perturbative renormalization group (RG) for weak and strong impurity backscattering.

This chapter is organized as follows. We explain fundamentals of the PIMC method in Sec. 2.1, and state details of update schemes of the PIMC simulation for the impurity problem in a spinless TLL in Sec. 2.2. Actual simulation for an impurity in spinful TLLs is performed in Sec. 2.3, where we present the zero-temperature phase diagram deduced from our data, and then make a comparison with the known RG result.

## 2.1 Fundamentals

In general field-theoretic problems, we are interested in the average of some observable $O$:

$$\langle O \rangle = \frac{\int \mathcal{D}\phi \, O[\phi] \, \mathrm{e}^{-S[\phi]}}{\int \mathcal{D}\phi \, \mathrm{e}^{-S[\phi]}}, \tag{2.1}$$

where $S[\phi]$ is the action describing the system. For the numerical evaluation of the average, the path integral over an infinite number of smooth paths is replaced with the sum over a finite number of discretized paths:

$$\langle O \rangle \simeq \frac{\sum_\phi O[\phi]\, \mathrm{e}^{-S[\phi]}}{\sum_\phi \mathrm{e}^{-S[\phi]}}. \tag{2.2}$$

In path-integral Monte Carlo simulations, this sum is evaluated with paths generated stochastically. However, it is inefficient to generate uniformly the paths since most of the paths thus generated scarcely contribute to the sum due to the Boltzman factor $e^{-S[\phi]}$. One way of improving the sampling efficiency is to generate a path $\phi^{(i)}$ according to an equilibrium distribution with probability $p(i) = \mathrm{e}^{-S[\phi^{(i)}]}$. Such a strategy is called importance sampling, and the thermal average is then replaced with the arithmetic mean

$$\langle O \rangle \simeq \frac{\sum_{\text{i.s.}} O[\phi]}{\sum_{\text{i.s.}} 1}. \tag{2.3}$$

In actual simulations, such an path is generated sequentially, $\phi^{(1)} \to \phi^{(2)} \to \phi^{(3)} \to \cdots$, so that transition of the path satisfies the condition of detailed balance

$$W(i \to j)p(i) = W(j \to i)p(j), \tag{2.4}$$

where $W(i \to j)$ denotes the probability of transition $\phi^{(i)} \to \phi^{(j)}$. The choice of $W(i \to j)$ is arbitrary as long as it satisfies Eq. (2.4). Here let us adopt the Metropolis algorithm; the transition $\phi^{(i)} \to \phi^{(j)}$ is always accepted if the energy is reduced $S[\phi^{(j)}] - S[\phi^{(i)}] < 0$, otherwise it is accepted with probability $\mathrm{e}^{S[\phi^{(i)}]-S[\phi^{(j)}]}$. For short

$$W(i \to j) = \min\{1, \mathrm{e}^{S[\phi^{(i)}]-S[\phi^{(j)}]}\}. \tag{2.5}$$

Note that $W(i \to j)$ identifies the accept probability for a given transition, not the transition itself; we need to design update schemes which generate the configurations of $\phi$ ergodically.

In a typical routine of the Metropolis algorithm, one repeats the following three steps (the operation "$\Leftarrow$" denotes substitution of right hand side into the left hand side):

1. $\phi^{(\text{old})} \Leftarrow \phi^{(\text{new})}$, and generate a new configuration $\phi^{(\text{new})}$ randomly.
2. Accept $\phi^{(\text{new})}$ with probability $p = \min\{1, \mathrm{e}^{S[\phi^{(\text{old})}]-S[\phi^{(\text{new})}]}\}$;
   Otherwise, $\phi^{(\text{new})} \Leftarrow \phi^{(\text{old})}$.
3. Measure $O[\phi^{(\text{new})}]$ and add it to the numerator of Eq. (2.3).

We note that before measurement one needs thermalization process, which is realized by repeating only the steps 1 and 2 so that the configuration of the path relaxes into an equilibrium one.

## 2.2 Single impurity problem in a spinless TLL

To be specific, we here describe the application of the PIMC method to the impurity problem in a spinless Tomonaga-Luttinger liquid [36]. As shown in the previous chapter [see Eq. (1.11)], this problem is described by the effective action

$$S = S_0 + S_V, \tag{2.6}$$

$$S_0 \equiv \frac{1}{\pi K\beta}\sum_{\omega_n}|\omega_n||\tilde{\phi}(\omega_n)|^2, \qquad S_V \equiv \int_0^\beta \mathrm{d}\tau \mathcal{V}(\phi(\tau)), \tag{2.7}$$

where $\tilde{\phi}(\omega_n)$ is the Fourier component of the path $\phi(\tau)$, and $\mathcal{V}(\phi) = -V\cos[2\phi(\tau)]$ is the potential. Hereafter, we consider a general potential form $\mathcal{V}(\phi)$. We discretize the imaginary time into $J$ time steps as $\tau_j = j\tau_c (j = 0, 1, \cdots, J-1)$ with the short time cutoff $\tau_c \equiv \beta/J$. For the discretized path defined as

$$\phi_j \equiv \phi(\tau_j), \qquad \tilde{\phi}_k \equiv \frac{\tilde{\phi}(\omega_k)}{\tau_c} = \sum_{j=0}^{J-1}\phi_j \mathrm{e}^{\frac{2\pi i}{J}jk}, \tag{2.8}$$

the action reads

$$S = \sum_{k=1}^{J/2}\frac{1}{2{\sigma_k}^2}|\tilde{\phi}_k|^2 + \tau_c\sum_{j=0}^{J-1}\mathcal{V}(\phi_j), \qquad {\sigma_k}^2 = \frac{J^2K}{8k}, \qquad {\sigma_{J/2}}^2 = \frac{JK}{2}, \tag{2.9}$$

where $\tilde{\phi}_{J-k} = {\tilde{\phi}_k}^*$ and ${\sigma_k}^2$ denotes standard deviation. In this thesis, we employ two types of update schemes for the PIMC simulation as explained in the following subsections.

### 2.2.1 Local update in the Fourier space

Since $S_0$ have a quadratic form in the Fourier space [56, 57], we modify the transition probability as

$$W(\text{old} \to \text{new}) = \mathrm{e}^{-S_0[\tilde{\phi}^{(\text{new})}]}\min\{1, \mathrm{e}^{S_V[\phi^{(\text{old})}]-S_V[\phi^{(\text{new})}]}\}, \tag{2.10}$$

and constitute the Metropolis algorithm (2.5) by accepting a new $\tilde{\phi}_{k\neq 0}$ generated according to the normal distribution with standard deviation $\sigma_k^2$ with probability

$$p = \min\{1, \mathrm{e}^{S_V[\phi^{(\text{old})}]-S_V[\phi^{(\text{new})}]}\}. \tag{2.11}$$

It is well-known that a random number $x$ normally distributed as $\propto \mathrm{e}^{-\frac{x^2}{2\sigma^2}}$ can be generated by means of the Box-Muller transformation

$$x = \sigma\sqrt{-2\log(1-r_1)}\cos 2\pi r_2 \quad \text{or} \quad \sigma\sqrt{-2\log(1-r_1)}\sin 2\pi r_2, \tag{2.12}$$

where $r_1$ and $r_2$ are random numbers uniformly distributed in the range of $[0, 1)$. Note that the Fourier component at $k = 0$, i.e., $\tilde{\phi}_0{}^{(\mathrm{new})}$ is randomly chosen from a uniform distribution ranging over $[0, \pi)$ and is accepted with probability (2.11).

### 2.2.2 Global update based on the cluster algorithm

Rewriting $S_0$ with $\phi_j$ in Eq. (2.9), we obtain the action in the imaginary-time representation:

$$S = -\sum_{j<j'} \kappa_{jj'} \phi_j \phi_{j'} + \tau_c \sum_j \mathcal{V}(\phi_j), \tag{2.13}$$

$$\kappa_{jj'} = -\frac{4}{KJ^2} \sum_{k=-J/2+1}^{J/2} |k| \mathrm{e}^{-\frac{2\pi i}{J} k(j-j')}, \tag{2.14}$$

where the interaction kernel $\kappa_{jj'}$ decays as $\sim |j - j'|^{-2}$ at low temperatures $J \to \infty$. If $\mathcal{V}(\phi)$ is a potential with plural minima, such as cosine potential and double-well potential, tunneling between the minima is strongly suppressed by the long-range interaction. As a result, a typical path stays most of time in the vicinity of potential minima and kink structures appears between the minima once in a while. Such paths can be generated efficiently by means of the cluster algorithm [58, 18]. First, a mirror axis $\phi = \phi^{\mathrm{axis}}$ is randomly chosen on one of the symmetry axes of $\mathcal{V}(\phi_j)$, and the displacement from it is defined as $\varphi_j \equiv \phi_j - \phi^{\mathrm{axis}}$. When one defines spin variables by the sign of the displacement of the field as $s_j = \varphi_j / |\varphi_j|$, the action (2.14) is rewritten into the long-range Ising model

$$S_0 = -\sum_{j<j'} \mathcal{K}_{jj'} s_j s'_j, \quad \mathcal{K}_{jj'} = \kappa_{jj'} |\varphi_j| |\varphi'_j|. \tag{2.15}$$

For this Ising model, we can apply the Swedsen-Wang cluster algorithm as follows. Each pair of sites $(j, j')$ is connected with bond probability

$$p_{jj'} = \max\{0, 1 - \mathrm{e}^{-2\mathcal{K}_{jj'}}\}, \tag{2.16}$$

and the cluster of connected sites is flipped against the mirror, i.e., $\phi_j{}^{(\mathrm{new})} = 2\phi^{\mathrm{axis}} - \phi_j{}^{(\mathrm{old})}$ for each $j$ included in the cluster. Note that one can build a cluster of sites in time $O(J \log J)$ using binary search [59].

## 2.3 Single impurity problem in a spinful TLL

In this section, we actually perform the PIMC simulation to solve the impurity problem in a spinful TLL [60]. The impurity problem in TLLs has been originally treated with perturbative renormalization group (RG) methods in the weak-

and strong-impurity limits [31, 32, 33]. Whether a conduction channel becomes perfectly transmitting or insulating at low temperatures is determined by the relevance of the corresponding backscattering or tunneling process. In contrast to the spinless case, in which RG analyses in the weak- and strong-backscattering limits seem to be smoothly connected, the phase diagrams of the spinful case show clear inconsistency in the two opposite limits, i.e., mismatch of RG flow, suggesting the existence of an intermediate (unstable) fixed point. From the standard perturbative RG approach, we can obtain little information about the phase diagram for an impurity with *intermediate* strength. In this section, we study the phase transition in the intermediate region of impurity strength using the PIMC simulation.

The single impurity in the spinful TLLs can be formulated in a similar way as the previous section. The effective action is written in terms of two bosonic fields corresponding charge and spin modes, $\phi_\rho(\tau)$ and $\phi_\sigma(\tau)$ as [31, 32, 33]

$$S = S_0 + S_1, \tag{2.17}$$

$$S_0 \equiv \sum_{\nu=\rho,\sigma} \frac{1}{2\pi K_\nu \beta} \sum_{\omega_n} |\omega_n||\tilde{\phi}_\nu(\omega_n)|^2, \tag{2.18}$$

$$S_1 \equiv V \int_0^\beta \mathrm{d}\tau \cos\phi_\rho(\tau) \cos\phi_\sigma(\tau), \tag{2.19}$$

where $\tilde{\phi}_\nu(\omega_n)$ denotes the Fourier component of $\phi_\nu(\tau)$. $S_0$ is rewritten in a nonlocal form along the imaginary time as

$$S_0 = -\sum_\nu \frac{1}{2K_\nu\beta^2} \int_0^\beta \mathrm{d}\tau\mathrm{d}\tau' \frac{\phi_\nu(\tau)\phi_\nu(\tau')}{\sin^2[(\pi/\beta)(\tau-\tau')]}, \tag{2.20}$$

which is used in the cluster algorithm explained in Sec. 2.2.2.

### 2.3.1 Perturbative renormalization group

In order to allow for a comparison of our numerical results with the known analytic viewpoints, here we briefly review the renormalization group (RG) picture presented in Refs. [31, 33]. In the weak backscattering limit, integration of the high-energy shell produces the effective higher-order scattering processes, whose amplitudes scale as

$$\frac{\mathrm{d}V(l)}{\mathrm{d}l} = \left[1 - \frac{1}{2}(K_\rho + K_\sigma)\right] V(l), \tag{2.21}$$

$$\frac{\mathrm{d}V_\rho(l)}{\mathrm{d}l} = (1-2K_\rho)V_\rho(l), \qquad \frac{\mathrm{d}V_\sigma(l)}{\mathrm{d}l} = (1-2K_\sigma)V_\sigma(l). \tag{2.22}$$

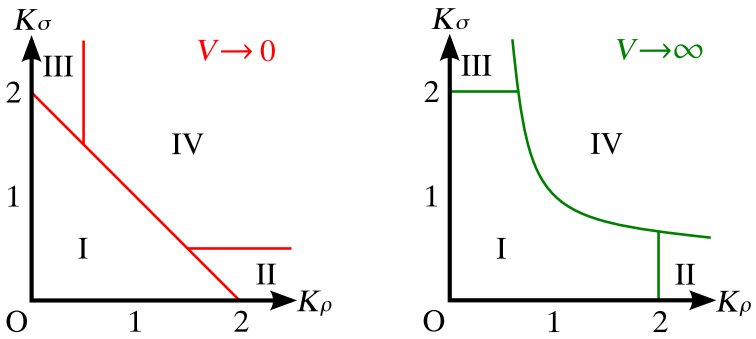


Figure 2.1: Phase diagram of the ground state in the $K_\rho$-$K_\sigma$ plain in the weak (left) and strong backscattering limits. (I) Both charge and spin are insulating; (II) Charge is conducting, while spin is insulating; (III) Charge is insulating, while spin is conducting; (IV) Both charge and spin are conducting.

Here the bandwidth is renormalized as $D' = De^{-l}$. $V(l)$ reflects a single electron, i.e., ${\psi_+}^\dagger\psi_-$+H.c., while $V_\rho(l)$ [$V_\sigma(l)$] reflects two charges (spins), i.e., $\psi^\dagger_{+,\uparrow}\psi_{-,\uparrow}\psi^\dagger_{+,\downarrow}\psi_{-,\downarrow}$+ H.c. ($\psi^\dagger_{+,\uparrow}\psi_{-,\uparrow}\psi^\dagger_{-,\downarrow}\psi_{+,\downarrow}$+H.c.). From these scaling equations, the phase diagram for weak backscattering are deduced as shown in the left panel of Fig. 2.1, where the phase boundaries are $K_\rho + K_\sigma = 2$, $K_\rho = 1/2$, and $K_\sigma = 1/2$. In region I, $V$ grows toward zero temperature ($l \to \infty$), which means perfect reflection of electrons at the potential barrier, hence an insulating phase. On the other hand, in region IV all the scattering amplitudes vanish toward zero temperature, so electrons can freely go through the barrier, hence a conducting phase. In region II (III), only $V_\sigma$ ($V_\rho$) grows at low temperatures while the other scattering amplitudes vanish.

In the opposite limit $V \to \infty$, the scaling equations are derived with help of the duality transformation as

$$\frac{\mathrm{d}t(l)}{\mathrm{d}l} = \left[1 - \frac{1}{2}\left(\frac{1}{K_\rho} + \frac{1}{K_\sigma}\right)\right] t(l), \tag{2.23}$$

$$\frac{\mathrm{d}t_\rho(l)}{\mathrm{d}l} = \left(1 - \frac{2}{K_\rho}\right) t_\rho(l), \quad \frac{\mathrm{d}t_\sigma(l)}{\mathrm{d}l} = \left(1 - \frac{2}{K_\sigma}\right) t_\sigma(l), \tag{2.24}$$

where $t$, $t_\rho$, and $t_\sigma$ are amplitudes of the single-electron tunneling, the (two-electron) charge tunneling, and the (two-electron) spin tunneling. From these scaling equations, the phase diagram for strong backscattering is obtained as shown in the right panel of Fig. 2.1, where the phase boundaries are $1/K_\rho + 1/K_\sigma = 2$, $K_\rho = 2$, and $K_\sigma = 2$.

The phase diagrams for the two limiting cases are thus obtained. Then, it is natural to ask what happens for an intermediate value of the scattering potential $V$. In order to illustrate this question visually, the three-dimensional phase diagram

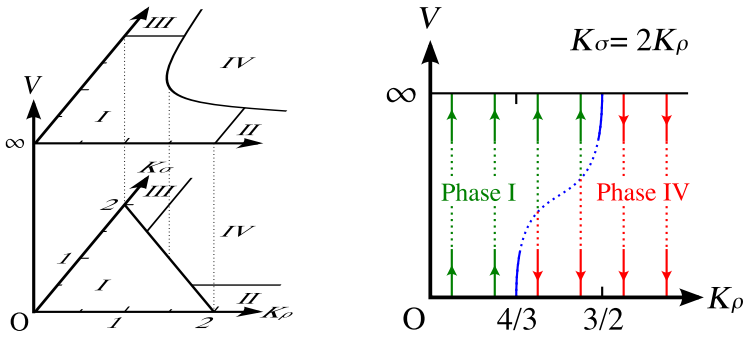


Figure 2.2: Left panel: Three-dimensional phase diagram in the $(K_\rho, K_\sigma, V)$-space. The phase boundaries are analytically obtained in the following two limits: for a weak impurity ($V \to 0$), the phase boundaries are three straight lines $K_\rho + K_\sigma = 2$, $K_\rho = 1/2$, and $K_\sigma = 1/2$; for a strong impurity ($V \to \infty$), the phase boundaries are a hyperbola $K_\rho^{-1} + K_\sigma^{-1} = 2$ and two straight lines $K_\rho = 2$ and $K_\sigma = 2$. The dotted lines connect the three points in the $V = 0$ and $V = \infty$ planes, at which the phase boundaries coincide in the both planes. Right panel: Expected RG flows on the intersection $K_\sigma = 2K_\rho$.

in the $(K_\rho, K_\sigma)$-plane is shown in the left panel of Fig. 2.2. The results of the perturbative RG for $V \to 0$ and $V \to \infty$ indicate that the four phases are smoothly connected between the two limiting values of $V$. Because the phase boundaries are different between the two limiting cases, they should vary as a function of $V$. The right panel of Fig. 2.2 shows the expected RG flows on the intersection $K_\sigma = 2K_\rho$. Here, we assumed that $K_\rho$ and $K_\sigma$ are not renormalized because the impurity should not change the bulk properties of the 1D electron system. We find that the phase boundary between region I and IV is shifted from $K_\rho = 4/3$ to $K_\rho = 3/2$ as $V$ increases. This indicates that there exists a phase transition characterized by an unstable fixed point at an intermediate value of $V$ in the range $4/3 < K_\rho < 3/2$ on this intersection.

While the RG approach with the help of duality transformation revealed the RG flow in the limit of weak- and strong-backscattering barriers, there is little hope to obtain further information on the RG flow in the whole parameter space, most of which belongs to the non-perturbative regime. In the rest of this chapter, we instead appeal to a numerical method, i.e., a PIMC simulation for the effective action $S$ given by Eq. (2.17), and examine transport properties of a spinful TLL with an impurity for non-perturbative backscattering potential barrier.

### 2.3.2 The path-integral Monte Carlo method

The basic strategy for construction of the path-integral Monte Carlo method adopted here is the same as the example explained in Sec. 2.2. Here, we briefly explain the PIMC method by emphasizing some points specific to the spinful model. The discretized action of the present problem is given by

$$S = S_0 + S_1 \tag{2.25}$$

$$S_0 = \sum_{\nu=\rho,\sigma} \sum_{k=1}^{J/2} \frac{1}{2{\sigma_{\nu k}}^2} |\tilde{\phi}_{\nu k}|^2, \tag{2.26}$$

$$S_1 = V\tau_c \sum_{j=0}^{J-1} \cos\phi_{\rho j} \cos\phi_{\sigma j}, \tag{2.27}$$

$${\sigma_{\nu k}}^2 \equiv \begin{cases} K_\nu J^2/4k & k = 1, 2, \cdots, J/2-1 \\ K_\nu J & k = J/2 \end{cases}, \tag{2.28}$$

where $\tau_c \equiv \beta/J$ is the short-time cutoff, and $\tilde{\phi}_{\nu k} = \tilde{\phi}^*_{\nu,J-k} = \sum_j \phi_{\nu j} \mathrm{e}^{\frac{2\pi i}{J} jk}$. For the present model, we consider three types of update schemes as explained below.

### 2.3.3 Local update

In a local update in the Fourier space, a new value of $\tilde{\phi}_{\nu k}$ $(k > 0)$ is randomly generated from a normal distribution with the variance ${\sigma_{\nu k}}^2$ given in (2.28) by means of the Box-Müller method. This update is accepted with a probability

$$p = \min\{1, \mathrm{e}^{-({S_1}^{\mathrm{new}} - {S_1}^{\mathrm{old}})}\}, \tag{2.29}$$

where ${S_1}^{\mathrm{new}} - {S_1}^{\mathrm{old}}$ is the variation of the potential term (2.27). For the $k = 0$ component $\tilde{\phi}_{\nu 0}$, a new value is generated from a uniform distribution ranged from $-\pi$ to $\pi$, and the update is accepted again with a probability (2.29).

### 2.3.4 Global update

A cluster update should be designed so that optimized paths for a given potential are efficiently generated. In the case of the double-cosine potential (2.27), an optimized path near the phase transition typically spends most of the time in potential minima, and also has some kink structures connecting adjacent potential minima, i.e., $(\phi_\rho, \phi_\sigma) = (n_\rho\pi, n_\sigma\pi)$ with integers $n_\rho$ and $n_\sigma$ such that $n_\rho + n_\sigma =$ odd for $V > 0$. In order to generate such kinks, we introduce two relative field variables $\varphi_{\nu j} \equiv \phi_{\nu j} - {\phi_\nu}^{\mathrm{mirror}}$ for $\nu = \rho, \sigma$ as shown in Fig. 2.3, where the reference ${\phi_\nu}^{\mathrm{mirror}}$ is appropriately chosen as described later. When one defines a spin variable by the

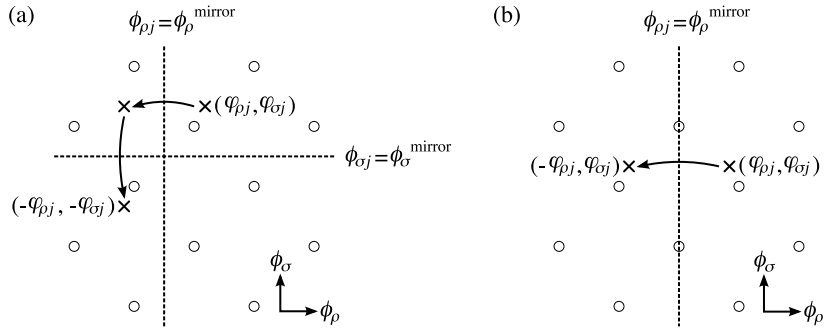


Figure 2.3: Cluster updates of field variables $\phi_{\rho j}$ and $\phi_{\sigma j}$ in a $\phi_\rho$-$\phi_\sigma$ plane, where $\varphi_{\nu j} \equiv \phi_{\nu j} - \phi_\nu{}^{\rm mirror}$. The empty circles represent the potential minima, and the dashed lines represent the reference fields $\phi_\rho{}^{\rm mirror}$ and $\phi_\sigma{}^{\rm mirror}$. Only the field variables at the $j$-th time step in a cluster are shown. (a) During one period of a double-field cluster update, a point $(\varphi_{\rho j}, \varphi_{\sigma j})$ is subject to mirror reflection twice, i.e., once with respect to $\phi_{\rho j} = \phi_\rho{}^{\rm mirror}$, and subsequently to $\phi_{\sigma j} = \phi_\sigma{}^{\rm mirror}$. (The whole process is $(\varphi_{\rho j}, \varphi_{\sigma j}) \to (-\varphi_{\rho j}, \varphi_{\sigma j}) \to (-\varphi_{\rho j}, -\varphi_{\sigma j})$.) (b) As for a charge-field cluster update, $\varphi_{\nu j}$ is subject to mirror reflection with respect to $\phi_\rho = \phi_\rho{}^{\rm mirror}$, i.e., $(\varphi_{\rho j}, \varphi_{\rho j}) \to (-\varphi_{\rho j}, \varphi_{\rho\ j})$. Similarly, $\varphi_{\sigma j}$ in a spin-field cluster is updated as $(\varphi_{\rho j}, \varphi_{\sigma j}) \to (\varphi_{\rho j}, -\varphi_{\sigma j})$.

sign of the relative field as $s_{\nu j} \equiv \varphi_{\nu j}/|\varphi_{\nu j}|$, the nonlocal term (2.20) is written in a discrete form as

$$S_0 = -\sum_\nu \sum_{j<j'} \kappa_{\nu jj'} s_{\nu j} s_{\nu j'}, . \tag{2.30}$$

Taking the bandwidth cutoff into account explicitly, the coupling coefficient $\kappa_{\nu jj'}$ is evaluated as

$$\kappa_{\nu jj'} \simeq -\frac{2|\varphi_{\nu j}||\varphi_{\nu j'}|}{K_\nu J^2} \sum_{k=-J/2+1}^{J/2} |k| e^{\frac{2\pi i}{J}(j-j')k}. \tag{2.31}$$

A cluster of spins is built by connecting sites with the bond probability determined by the exchange couplings $\kappa_{\nu jj'}$, and all the spins in the cluster is flipped with no rejection. If $\phi_\nu{}^{\rm mirror}$ is appropriately chosen so that the potential term $S_1$ remains unchanged after the cluster is flipped. In Fig. 2.3, two kinds of such rejection-free cluster update implemented in this chapter, named double-field cluster update and single-field cluster update, are illustrated.

In the double-field update illustrated in the left panel (a), one horizontal mirror and one vertical mirror are located along $\phi_\rho{}^{\rm mirror} = (n_\rho + 1/2)\pi$ and $\phi_\sigma{}^{\rm mirror} =$

$(n_\sigma + 1/2)\pi$, where $n_\rho$ and $n_\sigma$ are integers. The Ising spins are connected with bond probability

$$p_{jj'} = \max\{0, 1 - e^{-2\sum_\nu \kappa_{\nu jj'} s_{\nu j} s_{\nu j'}}\}. \tag{2.32}$$

Both the fields $\varphi_{\rho j}$ and $\varphi_{\sigma j}$ in the cluster are then reflected with respect to the two mirrors, i.e., $(\varphi_{\rho j}, \varphi_{\sigma j}) \to (-\varphi_{\rho j}, \varphi_{\sigma j}) \to (-\varphi_{\rho j}, -\varphi_{\sigma j})$. Note that the connected spins $s_{\nu j}$ and $s_{\nu j'}$ are not necessarily parallel, which is different from the original Swendsen-Wang algorithm. By means of this *double-field* cluster update, kink structures connecting nearest-neighbor potential minima are inserted efficiently.

In the single-field update is illustrated in the right panel (b) in Fig. 2.3, only a vertical mirror for the charge degree of freedom is located at ${\phi_\rho}^{\text{mirror}} = n_\rho \pi$ with an integer $n_\rho$. A cluster is constructed with bond probability

$$p_{\rho jj'} = \max\{0, 1 - e^{-2\kappa_{\rho jj'} s_{\rho j} s_{\rho j'}}\}. \tag{2.33}$$

The relative fields $\varphi_{\rho j}$ in the cluster are then reflected with respect to the vertical mirror, i.e., $(\varphi_{\rho j}, \varphi_{\sigma j}) \to (-\varphi_{\rho j}, \varphi_{\sigma j})$, while the spin fields are left unchanged. A similar cluster update is performed also for a horizontal mirror ${\phi_\sigma}^{\text{mirror}} = n_\sigma \pi$ with an integer $n_\sigma$. These *single-field* cluster updates insert kink structures between next-nearest-neighbor potential minima.

### 2.3.5 Linear conductance

In the PIMC simulation, we study zero-bias conductances of charge and spin channels to obtain the zero-temperature phase diagram for an intermediate value of $V$. In the linear response regime, they are calculated from analytic continuation

$$G_\nu = \lim_{i\omega_n \to 0} G_\nu(i\omega_n), \tag{2.34}$$

where the conductance at a Matsubara frequency is calculated from a correlation function given as

$$G_\nu(i\omega_n) = \frac{2e^2}{h} \frac{|\omega_n|}{\pi} \int_0^\beta \mathrm{d}\tau \langle \phi_\nu(\tau) \phi_\nu(0) \rangle e^{i\omega_n \tau}. \tag{2.35}$$

In the PIMC simulation, the spin and charge conductances are evaluated with Monte Carlo sampling for the correlation function in Eq. (2.35).

### 2.3.6 Results

This subsection is devoted to presenting our PIMC results. Phase transitions on the line of $K_\sigma = 1$ and 1.8 are deduced from numerical data in Sec. 2.3.6 and

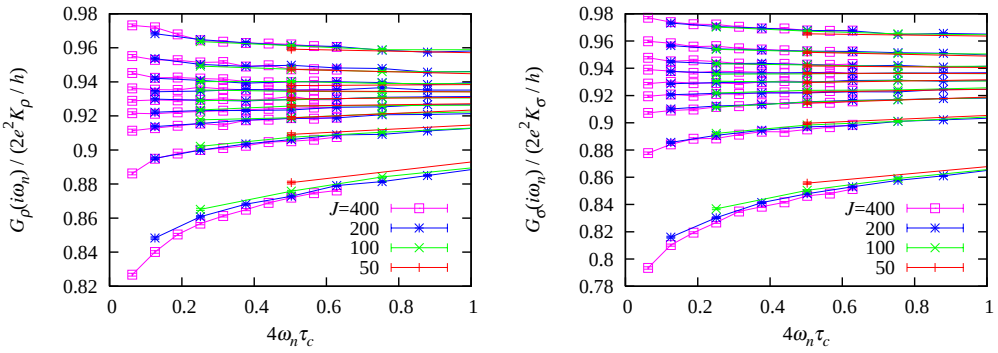


Figure 2.4: Charge conductance $G_\rho(i\omega_n)$ (left) and spin conductance $G_\sigma(i\omega_n)$ (right) for different values of $K_\rho$, plotted as a function of $\omega_n$. $K_\sigma$ is fixed at $K_\sigma = 1.0$ Symmetric coupling case ($K_\rho \simeq K_\sigma$). $J = 50$, 100, 200, and 400, and only the first ten points are shown for each Trotter number $J$. From top to bottom, the values of $K_\rho$ are 1.2, 1.1, 1.05, 1.025, 1.0, 0.975, 0.95, 0.9, and 0.8. Conductance curves (of both charge and spin) show an upward bend with decreasing $\omega_n$ when $K_\rho > 1.025$, whereas they are bent downward when $K_\rho < 0.975$.

Sec. 2.3.6, respectively. The whole phase diagram is discussed in Sec. 2.3.7 in comparison to the perturbative RG picture. In the present simulation, we fix the backscattering strength as $V\tau_c = 1$, and the temperature is varied from $J = 50$ to $J = 400$, where $J$ is inversely proportional to temperature as $J = \beta/\tau_c$.

**Phase transition at $K_\sigma = 1$**

In Fig. 2.4, we show the result on the $K_\sigma = 1$ line (SU(2) symmetric case), and plot the first ten points of $G_\nu(i\omega_n)$ as a function of $\omega_n$ for different values of $K_\rho$ near the phase boundary. For a given $K_\rho$, results for different $J$, i.e., for different temperatures are superposed to form a bundle of curves. For both $G_\rho(i\omega_n)$ and $G_\sigma(i\omega)$, one can see that the curves for $K_\rho > 1.025$ are bent upward with decreasing $\omega_n$ (in the limit of $\omega_n \to 0$), while the curves for $K_\rho < 0.975$ are bent downward. Note also that for a given $K_\rho$, the slope of different curves composing the same bundle always becomes steeper with decreasing temperature (increasing $J$). When the data shows such a monotonic dependence on temperature, one can determine the phase boundaries by simply identifying a turning point at which the bend of $G_\nu(i\omega_n)$ changes from upward to downward with decreasing $\omega_n$. In the present case, the phase transition appears to be located around $K_\rho = 1$ from Fig. 2.4.

To obtain the phase diagram, transition points are actually determined by trac-

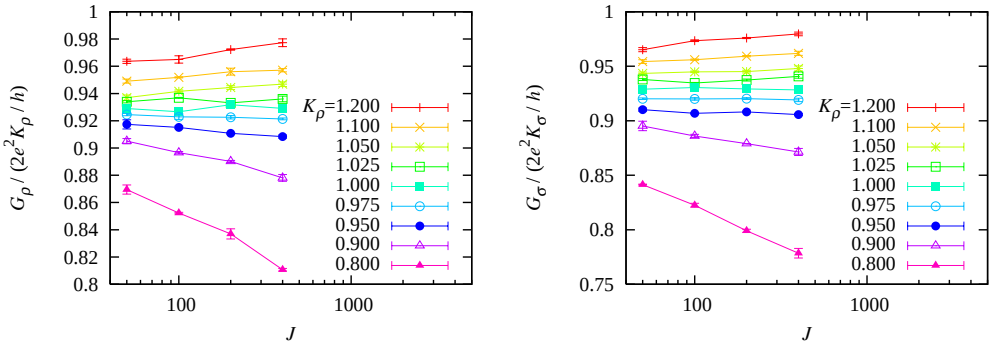


Figure 2.5: DC conductances of charge (left) and spin (right) channels for different values of $K_\rho$. $K_\sigma$ is fixed at $K_\sigma = 1.0$. Symmetric coupling case ($K_\rho \simeq K_\sigma$). Conductances are plotted as a function of the inverse temperature $J$. As expected from Fig. 3, both charge and spin conductances increase with decreasing temperature (increasing $J$) for $K_\rho > 1.025$, whereas they decrease for $K_\rho < 0.975$.

ing temperature dependence of dc conductances following Refs. [18, 61]. In Fig. 2.5, we plot the dc conductances as a function of the inverse temperature $J$, which are obtained by extrapolating the first five points on each curve in Fig. 2.4 to $\omega_n \to 0$. With decreasing temperature, the dc conductance (of both spin and charge) increases monotonically for $K_\rho > 1.025$, whereas it decreases monotonically for $K_\rho < 0.975$. Here, the charge and spin channels show a simultaneous transition from conducting to insulating phase in consistent with the RG results. Recall that in the RG picture (see Fig. 2.1) the IV and I phases touch at $(K_\rho, K_\sigma) = (1, 1)$ both in the weak- and strong-backscattering regimes, which suggests that the phase boundary at that point is a straight line independent of $V$ in the $(K_\rho, K_\sigma, V)$-space.

**Phase transition at $K_\sigma = 1.8$**

We plot the results of $G_\rho(i\omega_n)$ and $G_\sigma(i\omega_n)$ for the $K_\sigma = 1.8$ in Fig. 2.6. One can first observe that the charge and spin channels behave quite differently as a clear consequence of the anisotropy between $K_\rho$ and $K_\sigma$. The curves for charge conductance $G_\rho(i\omega_n)$ are bent upward for $K_\rho > 0.5$ with decreasing $\omega_n$, while the same curves for $K_\rho < 0.5$ are bent downward. In contrast to the case of $K_\sigma = 1$ in the previous subsection, the sign of the slope of the different curves composing the same bundle may change.

We show the corresponding dc conductances as a function of temperature in Fig. 2.7. The temperature dependence of the (charge) conductance $G_\rho$ shows a

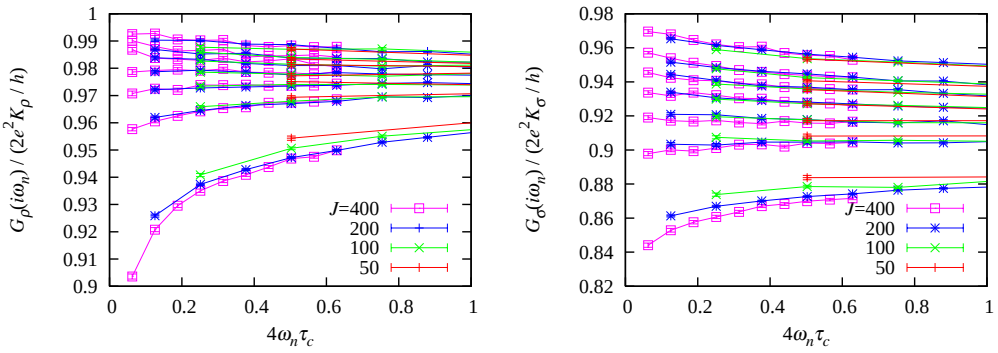


Figure 2.6: Charge conductance $G_\rho(i\omega_n)$ (left) and spin conductance $G_\sigma(i\omega_n)$ (right) for different values of $K_\rho$, plotted as a function of $\omega_n$. $K_\sigma$ is fixed at $K_\sigma = 1.8$. Asymmetric coupling case ($K_\rho \ll K_\sigma$). $J = 50$, 100, 200, and 400, and only the first ten points are shown for each Trotter number $J$. From top to bottom , the values of $K_\rho$ in the upper panel are 0.6, 0.55, 0.525, 0.5, 0.475, 0.45, and 0.4, while those in the lower panel are 0.5, 0.45, 0.425, 0.4, 0.375, 0.35, and 0.3. In this parameter regime, charge and spin channels behave quite differently.

monotonic behavior similar to the case of $K_\sigma = 1$. On the other hand, the temperature dependence of the spin conductance $G_\sigma$ is more peculiar: For example, if one focuses on the conductance curves for $K_\rho = 0.35$, their slopes are upward at higher temperatures, $J$ =50 or 100, whereas the same curves have an opposite slope at lower temperatures, $J = 200$ or 400. Such non-monotonic behaviors may be more clearly seen, if we look into the charge conductance in Fig. 2.7 for $K_\rho = 0.350$, 0.375, and 0.400. Similar crossover behaviors are observed whenever analyzing the boundary between phases I and III.

These monotonic temperature dependences are expected to reflect the non-monotonic flows of $V$ near the intermediate unstable fixed point. We note that the non-monotonic temperature dependences have already been reported in study of dissipative Josephson junctions in Ref. [61]. Since the precise location of such a non-trivial fixed point is unknown, one cannot immediately conclude that the spin channel is in the conducting phase, even if the conductance, e.g. for $K_\rho = 0.450$ or 0.500, tends to increase monotonically toward low temperatures up to $J = 400$. Possibly, it might turn insulating at a certain lower temperature which is numerically inaccessible. Since it is difficult to locate true phase boundaries at $T = 0$ in the presence of intermediate unstable fixed points, we instead identify the phase boundary at $T \neq 0$ by observing the temperature dependence near the lowest temperature $J \simeq 400$.

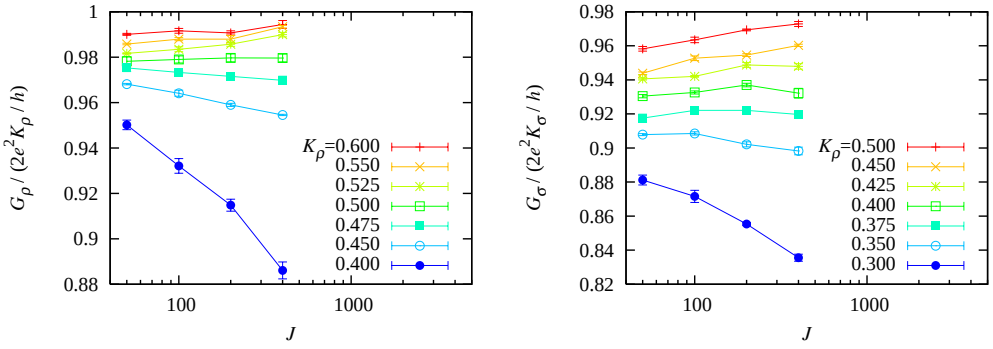


Figure 2.7: DC conductances of charge (upper) and spin (lower) channels for different values of $K_\rho$. $K_\sigma$ is fixed at $K_\sigma = 1.8$. Asymmetric coupling case ($K_\rho \ll K_\sigma$). Conductances are plotted as a function of the inverse temperature $J$. Upper : The temperature dependence for the charge channel shows monotonic increase ($K_\rho > 0.5$) or decrease ($K_\rho < 0.5$) with decreasing temperature. Lower : The spin conductance behaves non-monotonically for $K_\rho = 0.35$, 0.375, and 0.4, e.g., for $K_\rho = 0.375$, the conductance increases from $J = 50$ to $J = 100$, whereas it decreases from $J = 200$ toward $J = 400$.

### 2.3.7 Phase Diagram

Repeating the analyses outlined in the previous subsection for different sets of $K_\rho$ and $K_\sigma$ near the phase transition, we determine the whole phase boundaries in the $(K_\rho, K_\sigma)$-plane. In a left panel of Fig. 2.8, we show our phase diagram for a finite impurity strength $V\tau_c = 1$ obtained from the PIMC simulations at inverse temperature $J = \beta/\tau_c = 400$. Due to the symmetry of the action (2.17) in terms of $\rho$ and $\sigma$, the following discussion also holds true when the charge and spin degrees of freedom are interchanged.

The phase boundaries, denoted with solid lines, are indeed located between the two limits, which are shown in right two panels of Fig. 2.8. For nearly isotropic interactions $K_\rho \simeq K_\sigma$, our phase boundary at an intermediate coupling is close to the one for weak backscattering. The boundary between region III and IV is also close to the weak-backscattering phase boundary. On the other hand, for strongly anisotropic interactions $K_\rho \ll K_\sigma$, our phase boundary between I and III phases is much closer to the strong-backscattering phase boundary.

### 2.3.8 Discussion

For nearly isotropic interactions $K_\rho \simeq K_\sigma$, the system of $V\tau_c = 1$ is considered to be located in the weak-backscattering regime. This is indicated by the ob-

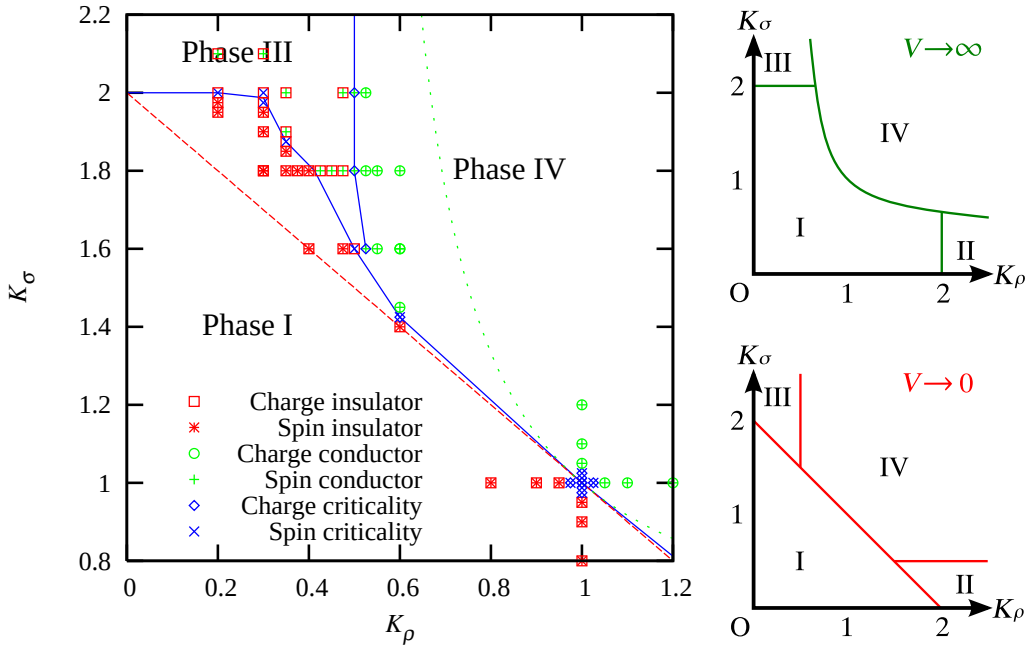


Figure 2.8: Phase diagram obtained from our PIMC simulations for the impurity strength $V\tau_c = 1$. For comparison, the RG results in the strong and weak barrier limits are shown in the upper-right and lower-right panels.

tained transition line between region I and IV similar to the weak-backscattering case, also by the large conductances of both the charge and spin channels (see, e.g., Fig. 2.5). For strongly anisotropic interactions $K_\rho \ll K_\sigma$, however, the I-III boundary resembles the one of the strong-backscattering case, i.e., $K_\sigma = 2$. Let us discuss what this feature indicates. For small $K_\rho$, the charge field is almost pinned around the potential minima. If we assume that this localized charge field does not affect the spin field, it is effectively described by a single-field action

$$S \simeq \frac{1}{2\pi K_\sigma \beta} \sum_{\omega_n} |\omega_n| |\tilde{\phi}_\sigma(\omega_n)|^2 + V \int d\tau \cos \phi_\sigma(\tau), \tag{2.36}$$

which leads naturally to the strong-backscattering phase boundary $K_\sigma = 2$. The assumption of decoupling between charge and spin fields is not trivial, because the I-III phase boundary is dependent on $K_\rho$ for weak barrier. Our result for the phase boundary between region I and III indicates that the coupling between two degrees of freedom vanishes by the potential barrier more sensitively than for the other perturbations.

## 2.4 Summary

In this chapter, we have explained intelligent update schemes of the PIMC method by taking impurity problems in TLLs as examples. We actually perform the PIMC simulation to solve the single impurity problem in a spinful TLL. Measuring the temperature dependence of the charge and spin conductances, we have obtained the phase diagram characterized by perfect conduction or insulation of the charge and spin channels for an intermediate impurity strength. We showed that the phase diagram obtained from our simulations is reasonably obtained in good consistency with the results of the perturbative RG analysis.

# Chapter 3

# Coulomb Blockade in an Open Quantum Dot

In this chapter, we study the Coulomb blockade in an open quantum dot connected to a bulk lead via a single mode point contact [62]. We extend the PIMC method introduced in Chap. 2 by taking into account the charging effect in the dot. The Coulomb oscillation of the average charge and capacitance of the dot is investigated, and is compared with known analytical results and those of numerical renormalization group. At the degeneracy point, we observe logarithmic divergence of the capacitance for strong backscattering at the point contact. This observation supports the conjecture that the nature of the present system at the degeneracy point is described by the two-channel Kondo problem for an *arbitrary* strength of tunneling.

This chapter is organized as follows. In Sec. 3.2, we state our model for an open quantum dot. In Sec. 3.33.3, we give details about the path-integral Monte Carlo method employed here. In Sec. 3.4, we present numerical results, and compare them with analytical results in some limits.

## 3.1 Introduction

As explained in Sec. 1.3, strong tunneling in a large quantum dot can be treated with a model consisting of a quantum dot and a half-infinite lead connected via a single mode point contact. The Coulomb blockade in such a structure has been studied theoretically by several authors [22, 23, 63, 64]. The peculiar nature of the large dot system is logarithmic divergence of the capacitance characterized by the analogy to the two-channel Kondo problem [65]; Matveev has revealed that with decreasing temperature the capacitance diverges logarithmically at the degeneracy points both in the weak and strong tunneling limits [22, 23]. The con-

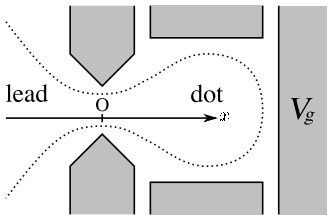


Figure 3.1: Schematic figure of an open quantum dot connected to a bulk lead by a single mode point contact. The dot is formed by applying negative voltage to the gates (gray regions). The solid line shows the boundary of the two-dimensional electron gas. The gate voltage $V_g$ controls the charge in the dot. The width of the constriction is adjusted so that only a single transverse mode is allowed to tunnel through the point contact.

sistency in these opposite limits suggests that the Coulomb blockade system at the degeneracy points can be described effectively by the two-channel Kondo model for an *arbitrary* strength of tunneling. One way of confirming this conjecture is to numerically study the intermediate tunneling regime. Recently, the two-channel Kondo effect has been studied by Lebanon *et al.* with the numerical renormalization group (NRG) method based on the tunneling Hamiltonian [64]. They showed that the two-channel Kondo behavior is observed in a broad range of tunneling strengths. Although their method is powerful enough to clarify properties of an open quantum dot in the intermediate tunneling regime, it is difficult to extend this approach to more complicated problems since numerical cost of matrix diagonalization in the NRG calculation becomes exponentially large as the orthogonal set of states in quantum dots increases. In this chapter, we present another numerical approach to the same problem, and show that our simulation leads to the same conclusion as in the NRG calculation. This result demonstrates that the PIMC approach is a powerful method to study dynamic response of quantum dot systems in the presence of electron interactions, which will be discussed in Chap. 4.

## 3.2 Model

We formulate a quantum dot strongly connected to a bulk lead shown in Fig. 3.1 using the bosonization method following Ref. [23]. The basic strategy is the same as in the spinless case discussed in Sec. 1.3.2. If the curvature of the constriction near the center of the point contact is smooth, the system is essentially one-dimensional (1D) [23] and is described by a Tomonaga-Luttinger liquid (TLL). The width of the constriction is adjusted so that only a single transverse mode is

allowed to tunnel through the point contact. Although the lead and the dot outside the constriction are two-dimensional (2D), transport through the point contact depends mainly on the one-dimensional behavior of electrons near the constriction. Then we can replace the 2D parts away from the constriction with 1D half-infinite leads, whose Hamiltonian is given in the bosonized form as

$$H_0 = \sum_{\nu=\rho,\sigma} \int \frac{\mathrm{d}x}{4\pi}\Big[\frac{u_\nu}{K_\nu}\Big(\frac{\partial\phi_\nu}{\partial x}\Big)^2 + u_\nu K_\nu\Big(\frac{\partial\theta_\nu}{\partial x}\Big)^2\Big], \tag{3.1}$$

where the subscriptions $\rho$ and $\sigma$ stand for a charge and spin mode, respectively. Here, $u_\nu$ is the sound velocity, and the bosonic fields $\phi_\nu$ and $\theta_\nu$ satisfy the commutation relation $[\phi_\nu(x), \partial\theta_{\nu'}(x')] = [\theta_\nu(x), \partial\phi_{\nu'}(x')] = 2\pi i\delta_{\nu\nu'}\delta(x - x')$. In the followings, we ignore the short-range interaction ($K_\rho = K_\sigma = 1$). The long-range Coulomb interaction is taken into account through the charging energy in the dot region as [23]

$$H_C = \frac{Q^2}{2C_0} + QV_g \simeq \frac{1}{\pi^2}E_C[\phi_\rho(x = 0) - \pi N_g]^2, \tag{3.2}$$

where $N_g \equiv -C_0V_g/e$. Note that the dot charge is expressed in terms of the bosonic field by means of the relation $Q = e\int_0^\infty \mathrm{d}x(-\partial_x\phi/\pi)$. We further assume a potential barrier $V_0\,\delta(x)$ at the center of constriction. The backscattering at the potential barrier is given by [23]

$$H_V = \frac{2V_0}{\pi v_F}D\cos\phi_\rho(x = 0)\cos\phi_\sigma(x = 0). \tag{3.3}$$

Here, $v_F$ is the Fermi velocity and $D$ is the bandwidth. The total Hamiltonian $H = H_0 + H_C + H_V$ describes the present problem.

By integrating out the boson fields in the bulk part ($x \neq 0$), the effective action is derived as

$$S \equiv S_0 + S_C + S_V, \tag{3.4}$$

$$S_0 = \frac{1}{2\pi\beta}\sum_{\nu=\rho,\sigma}\sum_{\omega_n}|\omega_n||\tilde{\phi}_\nu(\omega_n)|^2, \tag{3.5}$$

$$S_C = U\int d\tau\,[\phi_\rho(\tau) - \pi N_g]^2, \tag{3.6}$$

$$S_V = V\int d\tau\cos\phi_\rho(\tau)\cos\phi_\sigma(\tau), \tag{3.7}$$

where the spatial coordinate $x$ is omitted, and $\tilde{\phi}_\nu$ denotes the Fourier component of $\phi_\nu$. We have defined $U \equiv E_C/\pi^2$ and $V \equiv 2V_0D/\pi v_F$.

If an in-plane magnetic field is applied to the system as in Ref. [63], electrons are spin-polarized and the barrier height relatively shifts to $V_\uparrow = V_0(1-\delta)$ [$V_\downarrow = V_0(1+\delta)$] for electrons with up (down) spins, where $\delta$ is proportional to the Zeeman energy. Then, $S_V$ is replaced with

$$S_V = V \int d\tau [\cos\phi_\rho(\tau)\cos\phi_\sigma(\tau) + \delta \sin\phi_\rho(\tau)\sin\phi_\sigma(\tau)]. \tag{3.8}$$

## 3.3 The path-integral Monte Carlo method

For simplicity, here we consider the case without the Zeeman effect ($\delta = 0$). Discretizing the imaginary time into $J$ steps, we define the $j$th step on a discretized path as $\phi_{\nu j} \equiv \phi_\nu(j\beta/J)$, and its Fourier transform as $\tilde{\phi}_{\nu k} \equiv \sum_j \phi_{\nu j} e^{(2\pi i/J)jk} - \pi J N_g \delta_{\nu\rho}\delta_{k0}$. We thus obtain the discretized effective action as

$$S_0 + S_C = \sum_{\nu=\rho,\sigma} \sum_{k=0}^{J/2} \frac{1}{2{\sigma_{\nu k}}^2} |\tilde{\phi}_{\nu k}|^2, \tag{3.9}$$

$$S_V = V\tau_c \sum_{j=0}^{J-1} \cos\phi_{\rho j}\cos\phi_{\sigma j}, \tag{3.10}$$

where $\tau_c = \beta/J$. Note that the bandwidth $D$ is related to the interval of the time slice as $D = 2\pi/\tau_c$. We adopt two kinds of the update scheme described in the folloing subsections.

### 3.3.1 Local update

In a local update, for each pair of $\nu$ and $k$ a value of $\tilde{\phi}_{\nu k}$ is randomly chosen following a normal distribution $\propto e^{-|\tilde{\phi}_{\nu k}|^2/(2{\sigma_{\nu k}}^2)}$ with variance.

$${\sigma_{\rho 0}}^2 = \frac{J}{2U\tau_c}, \quad {\sigma_{\sigma 0}}^2 = \infty, \tag{3.11}$$

$${\sigma_{\nu J/2}}^2 = \frac{1}{2}\left[\frac{1}{2J} + \frac{U\tau_c}{J}\delta_{\nu\rho}\right]^{-1}, \tag{3.12}$$

$${\sigma_{\nu k}}^2 = \frac{1}{4}\left[\frac{k}{J^2} + \frac{U\tau_c}{J}\delta_{\nu\rho}\right]^{-1} \quad (k \neq 0, J/2). \tag{3.13}$$

Then a new path $\phi_{\nu j}$ is obtained from the inverse Fourier transform, and is accepted with probability $p = \min\{1, e^{-(S_V^{\rm new} - S_V^{\rm old})}\}$.

### 3.3.2 Global update

The basic idea of the cluster algorithm is the same as that explained in Sec. 2.2.2. We rewrite the effective action as

$$S_0 = -\sum_{\nu}\sum_{j<j'} \kappa_{jj'}\phi_{\nu j}\phi_{\nu j'}, \tag{3.14}$$

$$S_C = U\tau_c \sum_{j} [\phi_{\rho j} - \pi N_g]^2, \tag{3.15}$$

$$S_V = V\tau_c \sum_{j} \cos\phi_{\rho j} \cos\phi_{\sigma j}, \tag{3.16}$$

where the kernel is given by

$$\kappa_{jj'} = -\frac{2}{J^2} \sum_{k=-J/2+1}^{J/2} |k| \mathrm{e}^{(2\pi i/J)(j-j')k}. \tag{3.17}$$

We can design two types of cluster update as follows.

In a *single*-field cluster update, clusters for the charge and spin field are constructed separately with the bond probability between the $j$th and $j'$th site

$$p_{\nu jj'} = \max\{0, 1 - \exp(-2\kappa_{jj'}\varphi_{\nu j}\varphi_{\nu j'})\}. \tag{3.18}$$

Here we define the relative field $\varphi_{\nu j} \equiv \phi_{\nu j} - \pi M_\nu$ measured from the mirror located at $\phi_\nu = \pi M_\nu$ with an integer $M_\nu$.

In a *double*-field cluster update, on the other hand, a pair of the $j$th and $j'$th site for both the charge field and the spin field is connected using the probability

$$p_{jj'} = \max\left\{0, 1 - \exp\left(-2\sum_{\nu} \kappa_{jj'}\varphi_{\nu j}\varphi_{\nu j'}\right)\right\}, \tag{3.19}$$

with a half integer $M_\nu$.

Clearly, $S_V$ remains unchanged after these global moves, and the strength of backscattering does not matter. $S_C$ is invariant exceptionally in the single-field case for the spin mode, but it generally changes in the other cases. Then the cluster updates for the latter cases are accepted with the probability $p = \min\{1, \mathrm{e}^{-\Delta S_C}\}$, where the change in $S_C$ has the form

$$\Delta S_C = 4\pi U\tau_c(N_g - M_\rho) \sum_{j\in\text{cluster}} \varphi_{\rho j}. \tag{3.20}$$

The kinks, which run from a potential minimum to an adjacent one of the double-cosine potential in Eq. (3.16), are inserted in the path by these two types of cluster updates.

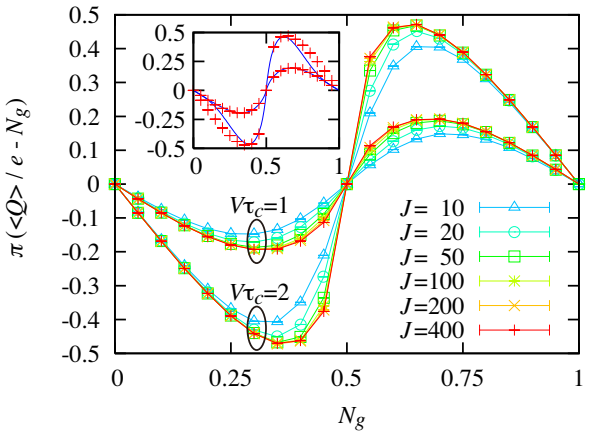


Figure 3.2: Coulomb oscillation of the average charge of the quantum dot for different temperatures $J = 10$, 20, 50, 100, 200, and 400. A bundle of curves with smaller amplitude corresponds to $V\tau_c = 1$, and the other to $V\tau_c = 2$. Inset: Comparison of the average charge for $V\tau_c = 1$ and 2 between our PIMC data at $J = 400$ (crosses) and the analytic result for small $V$ at zero temperature (solid line).

## 3.4 Results and Discussion

In this section, we present our PIMC results. After showing the result of the gate-voltage dependence of the dot charge in Sec. 4.4.1, we examine the logarithmic divergence of the capacitance in Sec. 4.4.2. Finally, we study the channel anisotropy effect ($\delta \neq 0$) in Sec 4.4.3. $U\tau_c = 1/4$ is fixed, and the temperature is varied down to $J = \beta/\tau_c = 400$. Without losing generality, we can restrict the value of $N_g$ in the range $0 \leq N_g \leq 1$.

### 3.4.1 Coulomb oscillation of the dot charge

The average charge in the dot is evaluated as

$$\langle Q \rangle = \frac{e}{\pi} \langle \bar{\phi}_\rho \rangle, \quad \bar{\phi}_\rho \equiv \frac{1}{\beta} \int_0^\beta d\tau \, \phi_\rho(\tau), \tag{3.21}$$

where $\langle O \rangle \equiv Z^{-1} \int \mathcal{D}\phi_\rho \mathcal{D}\phi_\sigma O e^{-S}$ denotes the expectation value of an observable $O$. In Fig. 3.2, we plot $\langle Q \rangle$ for $V\tau_c = 1$ and 2 as a function of the gate voltage $N_g$. As the temperature decreases (the inverse temperature $J$ increases), the Coulomb blockade is enhanced. If we focus on the lowest temperature $J = 400$, the curve appears to converge except near the degeneracy point $N_g = 1/2$. We compare the

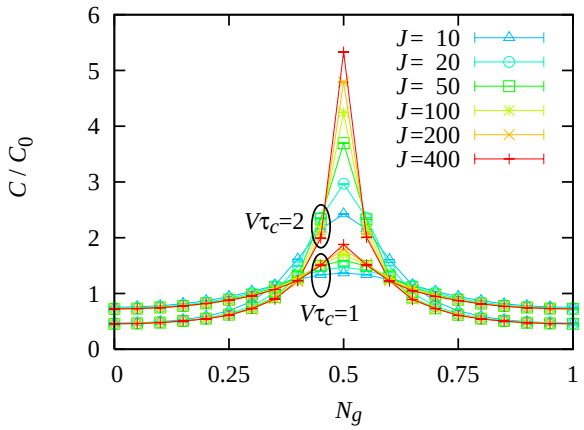


Figure 3.3: Coulomb oscillation of the capacitance of the dot for different temperatures $J = 10$, 20, 50, 100, 200, and 400. A bundle of curves with smaller amplitude corresponds to $V\tau_c = 1$, and the other to $V\tau_c = 2$.

data of $J = 400$ with the analytic result for $T = 0$ in the strong tunneling limit ($V \to 0$). In Ref. [23], the charge field $\phi_\rho$ is pinned down to $\pi N_g$ due to the large charging energy $T \ll E_C < D$, and the backscattering strength $V$ is renormalized by the charge fluctuation. As a result, the average charge is calculated for small $V$ (corresponding to strong tunneling) as

$$\frac{\langle Q \rangle}{e} = N_g + \frac{2\gamma|r|^2}{\pi^2} \log(\mathrm{e}\,|r|^2 \cos^2 \pi N_g) \sin 2\pi N_g, \tag{3.22}$$

where $r = V_0/v_F$ is a reflection coefficient, and $\gamma = \mathrm{e}^{\mathrm{C}}$ with the Euler's constant $\mathrm{C} \simeq 0.5772$. The inset of the Fig. 3.2 shows the comparison for $V\tau_c = 1$ and 2 between our data of $J = 400$ and Eq. (3.22). For $V\tau_c = 1$, the analytic result shown as a solid line is almost superposed on our data points; the expression (3.22) based on the pinning of $\phi_\rho$ describes well the Coulomb oscillation of $\langle Q \rangle$. For $V\tau_c = 2$, on the other hand, our data points away from $N_g = 1/2$ disagree with the analytic expression; the system is no longer in the strong tunneling regime for such a large value of $V$. It should be noted that similar deviation from Eq. (3.22) in the intermediate tunneling regime has been reported in the NRG results. [64]

### 3.4.2 Logarithmic divergence of the capacitance

Near $N_g = 1/2$ the oscillation curve in Fig. 3.2 depends on $J$ even at lower temperatures. This is related to the singularity derived from the two-channel Kondo problem hidden in the Coulomb blockade system at the degeneracy point. To see

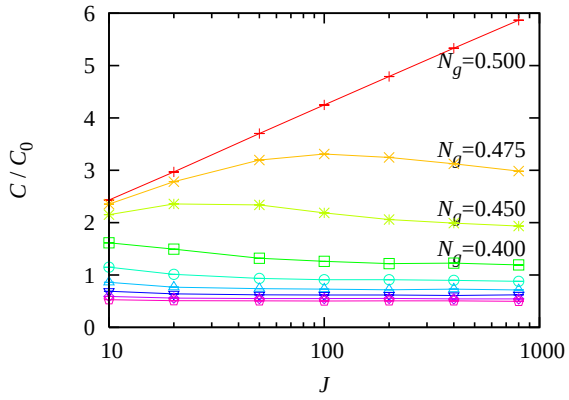


Figure 3.4: Temperature dependence of the capacitance of the dot for $V\tau_c = 2$. The gate voltage $N_g$ is varied from 0.15 to 0.50 (from bottom to top) at intervals of 0.05. The curve for $N_g = 0.475$ is also shown.

the peculiar nature of the system more clearly, we now measure the capacitance of the dot defined as

$$C = -\frac{\partial}{\partial V_g}\langle Q\rangle = \frac{e^2}{\pi^2}\beta[\langle\bar{\phi}_\rho{}^2\rangle - \langle\bar{\phi}_\rho\rangle^2]. \tag{3.23}$$

In Fig. 3.3, we plot the capacitance for $V\tau_c = 1$ and 2 as a function of the gate voltage $N_g$ at low temperatures. The amplitude of the Coulomb oscillation of the capacitance grows larger as $J$ and $V$ increase. The temperature dependence strongly depends on the gate voltage; away from $N_g = 1/2$, the capacitance is convergent at low temperatures whereas the peak at $N_g = 1/2$ keeps growing and sharpening up to the lowest temperature $J = 400$.

In Fig. 3.4, we show the capacitance for intermediate tunneling $V\tau_c = 2$ as a function of the inverse temperature $J$ for different values of the gate voltage $N_g$. In this figure, the temperature dependence of the capacitance is classified into three different types: When the temperature decreases, (I) for $N_g \leq 0.40$, the capacitance decreases monotonically; (II) for $N_g = 0.45$ and 0.475, the capacitance once increases, and decreases below a crossover temperature; (III) for $N_g = 0.50$, the capacitance increases monotonically. In Ref. [23], it is suggested from analytic results that the low-energy property of the Coulomb blockade system near the degeneracy point ($N_g = 1/2$) is governed by the physics of the two-channel Kondo problem for an *arbitrary* strength of tunneling. This prediction is supported by the logarithmic divergence of the capacitance for the type III. The transient increase in the capacitance for the type II is also a sign of the two-channel Kondo physics. For $N_g \neq 1/2$, an intrinsic low energy cutoff in the strong tunneling limit ($V \to 0$)

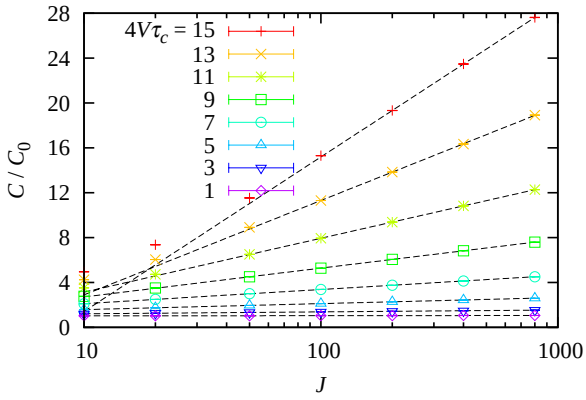


Figure 3.5: Capacitance at a degeneracy point $N_g = 1/2$ plotted as a function of the inverse temperature $J \equiv \beta/\tau_c$ for various values of $V$. Logarithmic fit of the data for each $V$ is shown as a dashed line.

is given by [23]

$$\Gamma = \frac{8\gamma|r|^2}{\pi^2} E_C \cos^2 \pi N_g. \tag{3.24}$$

At low temperatures below $\Gamma$, the logarithmic divergence characteristic of the two-channel Kondo model disappears. One can evaluate the order of the crossover temperatures of the curves in Fig. 3.4 using the expression (3.24). For example, the crossover temperatures for $N_g = 0.475$, 0.45, and 0.4 are estimated as $J \simeq 182$, 46, and 12, respectively.

In order to study in detail the logarithmic divergence of the capacitance, we show the capacitance at the degeneracy point $N_g = 1/2$ in Fig. 3.5 as a function of the inverse temperature $J$. The results for different backscattering strengths from $V\tau_c = 1/4$ to $V\tau_c = 15/4$ are shown. Here, one can estimate the transmission probability through the barrier using the expression $\mathcal{T} = 1/[1 + (V_0/v_F)^2]$ in the noninteracting case ($U = 0$); for example, $V\tau_c = 1/4$ corresponds to $\mathcal{T} \simeq 0.9961$ (strong tunneling), while $V\tau_c = 15/4$ to $\mathcal{T} \simeq 0.5322$ (intermediate tunneling). One can see that our data points diverge logarithmically with decreasing temperature for any value of $V$ as far as our simulation is performed.

Next, we compare this logarithmic behavior of our data with the analytic results for the strong and weak tunneling limit. In Fig. 3.6, the coefficient derived from the logarithmic fit of the capacitance is plotted as a function of $V$. According to the analytic calculation for the strong tunneling limit ($V \to 0$) [23], the

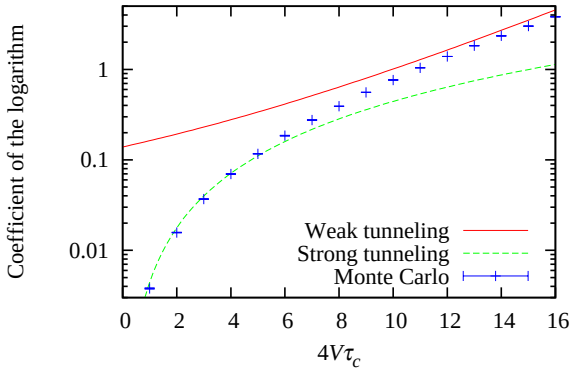


Figure 3.6: Coefficient of logarithm of the capacitance plotted as a function of $V$. The analytic result for strong(weak) tunneling is shown by the dashed(solid) line (see also the text).

capacitance diverges at low temperatures as

$$C = C_0\left[1 + \frac{4\gamma|r|^2}{\pi}\log\left(\frac{E_C}{T}\right)\right]. \tag{3.25}$$

For small $V$, i.e., in the strong tunneling regime, our data points agree well with the analytic result $4\pi\gamma|r|^2C_0/e^2 \simeq 0.004429V^2$ shown as a solid line. For larger values of $V$, on the other hand, they grows faster than the analytic result. Thus, the analytic expression (3.25) fails for intermediate strength of tunneling. Nevertheless, the logarithmic divergence in Fig. 3.5 in this regime clearly indicates that the present system is understood by the physics of the two-channel Kondo model for any value of $V$.

In the present calculation, we could not reach the weak tunneling regime, because exponential decay of the Kondo temperature $T_K$ with respect to $V$ makes it difficult to observe the Kondo effect in the finite-temperature simulation. However, a qualitative discussion is possible by focusing on the asymptotic behavior of the coefficient of the logarithm. The analytical expression for large $V$ is obtained by mapping to the two-channel Kondo model as [23, 66]

$$C \simeq 0.050\frac{e^2}{T_K}\log\left(\frac{T_K}{T}\right), \quad T_K = Dt\nu\exp\left(-\frac{\pi}{4t\nu}\right). \tag{3.26}$$

Here $t$ is the tunneling matrix element and $\nu$ is the density of states in the lead. We can estimate $t\nu$ from the barrier height $V_0$ through the transmission probability $\mathcal{T} = 4(\pi t\nu)^2/[1 + (\pi t\nu)^2]^2$ derived for $U = 0$. We thus obtain the relation $(t\nu)^{-1} = \pi[\sqrt{(V_0/v_F)^2 + 1} + V_0/v_F]$. If we assume that this relation holds also for $U > 0$, we

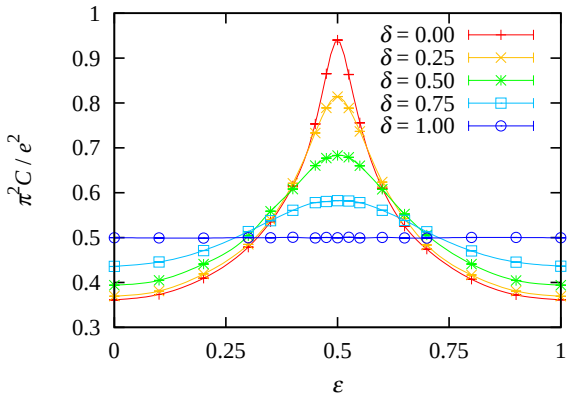


Figure 3.7: Coulomb oscillation of the capacitance in the presence of the in-plane magnetic field for $J = 400$ and $V\tau_c = 2$.

can calculate the coefficient of the logarithm for large $V$ from (3.26). However, we found that the prefactor of $T_K$ given in Eq. (3.26) disagrees with our data as found in the NRG calculation [64]. There seems to be several reasons for this inconsistency. For example, the result (3.26) is obtained for the *isotropic* Kondo model [66], while the present system is described by the *anisotropic* Kondo model [22]; this difference may affect the prefactor quantitatively. On the other hand, the exponent of $T_K$ deduced from our data is asymptotically consistent with Eq. (3.26) in the weak tunneling region ($V \to \infty$). In Fig. 3.6, we also show $\propto A\exp(\pi/4tv)$ as an asymptote (solid line), where its prefactor $A$ is adjusted by hand.

### 3.4.3 Effect of channel anisotropy

In this subsection, we discuss the effect of channel anisotropy in the presence of an in-plane magnetic field ($\delta \neq 0$). The channel anisotropy term proportional to $\delta$ is, together with the gate-voltage difference $\epsilon \equiv N_g - 1/2$ from the degeneracy point, a relevant perturbation to the two-channel Kondo fixed point in the context of the renormalization group. Therefore, the divergence of the capacitance is expected to be suppressed at low temperatures. Actually, the capacitance at zero temperature for strong tunneling ($V \to 0$) is calculated analytically as [63]

$$C = C_0\left[1 + \frac{4\gamma}{\pi}\left(\frac{V_0}{v_F}\right)^2(1-\delta^2)\log\left(\frac{E_C}{\Gamma(N_g)}\right)\cos(2\pi N_g)\right]. \tag{3.27}$$

The low-energy cutoff takes the form $\Gamma(N_g) = (8\gamma E_C/\pi^2)(V_0/v_F)^2\min(\sin^2\pi\epsilon, \cos^2\pi\epsilon)$. Note that the capacitance (3.27) remains finite except for the two-channel Kondo

fixed point $(\epsilon, \delta) = (0, 0)$. Because the above analytic results are obtained only in the two limits ($\epsilon \ll \delta$ and $\epsilon \gg \delta$), the whole Coulomb oscillation of the capacitance $C$ has not been calculated so far. We now show the Monte Carlo result for the gate-dependence of the capacitance for $V\tau_c = 1$ at low temperatures ($J = 400$) in Fig. 3.7. We see that the Coulomb oscillation of $C$ is smoothly suppressed as $\delta$ increases. As $\delta$ approaches 1, one spin-channel shows nearly perfect transmission while the other shows nearly perfect reflection. This is why its capacitance has cosine-like line shape near $\delta = 1$, in good agreement with the spinless case [23].

## 3.5 Summary

In this chapter, we have demonstrated the PIMC simulation of the Coulomb blockade phenomena in a open quantum dot at low temperatures. The Coulomb oscillation of the average charge and capacitance of the dot are studied in the intermediate tunneling regime, where the analytical results for the two limits of strong and weak tunneling are invalid. The amplitude of oscillation monotonically increases with decreasing temperature or increasing the backscattering strength. We confirmed that logarithmic divergence of the capacitance appears at the degeneracy point $N_g = 1/2$ even in the intermediate tunneling regime. This observation indicates that the present system has a two-channel Kondo nature for an *arbitrary* strength of tunneling. We also studied the effect of the channel anisotropy in the presence of the Zeeman energy.

These conclusions agree well with the numerical renormalization group (NRG) calculation by Lebanon *et al.* [64]. The NRG approach based on the tunneling Hamiltonian has several advantages. For example, NRG can access ultra-low temperatures because fine energy-meshes are taken near the Fermi energy. However, this method tends to need heavy calculation if one increases the number of bases of states in quantum dots. Our approach by the PIMC simulation gives an alternative way to treat transport in quantum dots, which is applicable to more complicated models. Our results obtained here indicate that the PIMC method actually provides a powerful method to access low-temperature transport properties. Based on this success, we consider dynamic response of quantum dot systems in the next chapter.

# Chapter 4

# Charge Relaxation Resistance

In this chapter, we study dynamic response of a mesoscopic capacitor composed of a quantum dot and a lead in the presence of strong electron interactions [67]. By means of perturbation theory, renormalization group technique, and the path-integral Monte Carlo method, we analyze the charge relaxation resistance in the whole range of dot-lead coupling. We predict that the charge relaxation resistance is universal even in the presence of strong Coulomb blockade for the Luttinger parameter $K > 1/2$, while the Kosterlitz-Thouless transition dramatically influences the universal nature of the charge relaxation resistance for $K < 1/2$.

This chapter is organized as follows. After stating introduction in Sec. 4.1, we summarize the universal nature of the charge relaxation resistance based on the scattering theory by Büttiker *et al.* in Sec. 4.2. In Sec. 4.3, we introduce our model for a mesoscopic capacitor, and explain its basic property. The update scheme in the PIMC method is described in Sec. 4.4, and our results are presented in Sec. 4.5.

## 4.1 Introduction

There is renewed interest in a dynamical aspect of mesoscopic systems stimulated by recent experiments observing low-frequency response of a mesoscopic capacitor [9], which is schematically shown in the left panel of Fig. 4.1. The mesoscopic capacitor is a quantum analog of classical *RC* circuit as shown in the right panel of the figure; reflection on the point contact between the dot and the lead acts as a resistor $R_q$, while capacitive coupling between the dot charge and the gate voltage plays the role of a capacitor $C_\mu$. In a classical *RC* circuit, the admittance is given by the Kirchhoff's law

$$G(\omega) = \frac{1}{R - (i\omega C)^{-1}}, \tag{4.1}$$

where the ac resistance $R$ equals the dc resistance. However, the latter equality is not the case in the mesoscopic capacitor. In their pioneering work [19], Büttiker *et al.* have extended the Kirchhoff's law (4.1) to the mesoscopic capacitor, replacing $C$ and $R$ with their quantum counterparts $C_\mu$ and $R_q$, respectively. In the low-frequency expansion of the admittance

$$G(\omega) = -i\omega C_\mu + \omega^2 {C_\mu}^2 R_q + O(\omega^3), \qquad (\omega \ll 1/R_q C_\mu), \tag{4.2}$$

they have proved that $R_q$ equals half a resistance quantum $h/2e^2$ irrespective of transmission through the point contact. A recent experiment supports this theoretical prediction [9]. $R_q$ measured at such a low frequency region is named *charge relaxation resistance* after the condition $\omega \ll 1/R_q C_\mu$, which clearly guarantees charge relaxation in the dot. The universal quantization of the charge relaxation resistance is remarkable because it contradicts a naive conjecture based on the additive nature of impedance in classical ac circuits. Indeed, if the "resistor" and the "capacitor" in the quantum $RC$ circuit were independent building blocks as in the classical case, the resistance would be described by the Landauer's formula for the point contact, explicitly dependent on the transmission probability through the constriction.

So far the charge relaxation resistance has been studied theoretically within mean-field-type approximation. As the size of the mesoscopic capacitor is reduced, however, we need to examine whether the electron interaction influences the universal nature of the charge relaxation resistance. In this chapter, we study the charge relaxation resistance in the presence of electron interactions, employing both analytical and numerical methods.

## 4.2 Universal charge relaxation resistance

In this section, we briefly summarize the self-consistent scattering theory by Büttiker *et al.* [19] and derive the universal quantization of the charge relaxation resistance

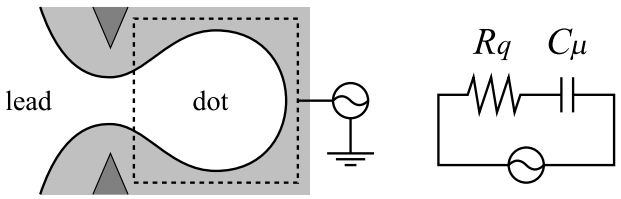


Figure 4.1: Mesoscopic capacitor and its equivalent $RC$ circuit. Reflection on the point contact corresponds to $R_q$ and capacitive coupling between the dot charge and the gate voltage to $C_\mu$.

$R_q = h/2e^2$. The essence of their theory is that the charging effect in the quantum dot is taken into account self-consistently by considering an effective time-dependent electric potential inside the dot denoted by $U_g(t)$, which may differ from the external ac gate voltage $V_g(t)$. For simplicity, the electric potential of the lead is fixed to zero. Then the dot charge can be expressed in three ways. First, focusing on the capacitive coupling coupling between the gate electrode and the dot, variation in the dot charge reads

$$-\mathrm{d}\langle Q\rangle = C_g(\mathrm{d}V_g - \mathrm{d}U_g), \tag{4.3}$$

where $C_g$ denotes the geometrical capacitance. Next we can also express the charge using the density of states in the dot $\mathcal{D}(\epsilon)$:

$$-\mathrm{d}\langle Q\rangle = e^2\mathcal{D}(\epsilon)\mathrm{d}U_g \equiv C_q\mathrm{d}U_g, \tag{4.4}$$

which implies that the dot charge is capatively coupled to the lead by the capacitance $C_q \equiv e^2\mathcal{D}(\epsilon)$. Combining the definition of the electrochemical capacitance $C_\mu \equiv -\mathrm{d}\langle Q\rangle/\mathrm{d}V_g$, i.e., $-\mathrm{d}\langle Q\rangle = C_\mu\mathrm{d}V_g$ with Eqs. (4.3) and (4.4), we arrive at

$$C_\mu\mathrm{d}V_g = C_g(\mathrm{d}V_g - \mathrm{d}U_g) = C_q\mathrm{d}U_g, \qquad \therefore \frac{1}{C_\mu} = \frac{1}{C_g} + \frac{1}{C_q} \tag{4.5}$$

Thus the introduction of the effective potential $U_g$ results in the electrochmical capacitance $C_\mu$ split into $C_g$ and $C_q$ in series as depicted in Fig. 4.2.

In the same way, when the gate voltage is oscillating with frequency $\omega$, the current through the circuit can be expressed in three ways:

$$I(\omega) = -\frac{\mathrm{d}\langle Q\rangle}{\mathrm{d}t} = G(\omega)V_g(\omega) = -i\omega C_g[V_g(\omega) - U_g(\omega)] = g(\omega)U_g(\omega) \tag{4.6}$$

$$\therefore \frac{1}{G(\omega)} = \frac{1}{g(\omega)} + \frac{1}{-i\omega C_g}, \tag{4.7}$$

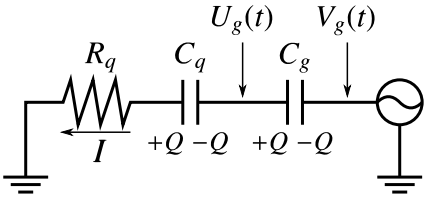


Figure 4.2: Equivalent circuit of a mesoscpic capacitor in the self-consistent scattering theory. The serial combination of the geometrical capacitance $C_g$ and the quantum capacitance $C_q$ results from the effective electric potential $U_g$ associated with the charging effect.

where $G(\omega)$ and $g(\omega)$ are the total admittance and the admittance through the point contact, respectively. Note that the scattering theory predicts

$$g(\omega) = \frac{e^2}{h}\int \mathrm{d}E\,\mathrm{Tr}[\mathbf{1} - \mathbf{S}^\dagger(E)\mathbf{S}(E+\omega)]\frac{f(E) - f(E+\omega)}{\omega}, \tag{4.8}$$

where $\mathbf{S}(E)$ is the scattering matrix of the point contact and $f(E)$ is the Fermi distribution. By substitute Eq. (4.8) into Eq. (4.7) and expanding $G(\omega)$ in $\omega$, we obtain a low-frequency expression of the total admittance similar to Eq. (4.2). Then comparison of each term in the the two expressions up to second order in $\omega$ leads to

$$C_q = \frac{1}{2\pi i}\int \mathrm{d}E\left(-\frac{\mathrm{d}f}{\mathrm{d}E}\right)\mathbf{S}^\dagger\frac{\partial\mathbf{S}}{\partial E}, \tag{4.9}$$

$$R_q = \frac{h}{2e^2}\frac{\int \mathrm{d}E(-\mathrm{d}f/\mathrm{d}E)\mathrm{Tr}[\mathbf{S}^\dagger(E)\partial\mathbf{S}(E)/\partial E]^2}{\{\int \mathrm{d}E(-\mathrm{d}f/\mathrm{d}E)\mathrm{Tr}[\mathbf{S}^\dagger(E)\partial\mathbf{S}(E)/\partial E]\}^2}. \tag{4.10}$$

At finite temperature, the charge relaxation resistance $R_q$ depends on transmission probability of the point contact, as well as the gate voltage, through the scattering matrix $\mathbf{S}$. At zero temperature, on the other hand, $\mathbf{S}$'s in Eq. (4.10) are canceled out due to $-\mathrm{d}f/\mathrm{d}E = \delta(E)$. As a result, the charge relaxation resistance $R_q$ defined at low frequencies $\omega \ll 1/R_qC_\mu$ is quantized to $h/2e^2$ per channel at $T = 0$. This is the remarkable result Büttiker *et al.* obtained in their pioneering work [19].

We should note that the two-capacitor picture for the total capacitance (4.5) breaks down when the charge fluctuation becomes large and the charging effect cannot be well-described with the mean field $U_g$. This can be seen from, e.g., the obvious inequality resulting from Eq. (4.5):

$$C_\mu = \frac{C_gC_q}{C_g + C_q} \le C_g. \tag{4.11}$$

At zero temperature, $C_q$ can be estimated from Eq. (4.9) as [9]

$$C_q = \frac{e^2}{\Delta}\frac{1 - r^2}{1 - 2r\cos(2\pi\epsilon/\Delta) + r^2}, \tag{4.12}$$

where $r$ is the reflection coefficient and $\epsilon$ denotes the gate voltage relative to a degeneracy point of two neighboring charge states. From Eq. (4.12), $C_q$ oscillates as a function of the gate voltage $V_g$ and has sharp peaks at degeneracy points. The peak height should be enhanced infinitely as $r \to 1$, whereas Eq. (4.11) indicates that it is saturated at $C_g$. If the latter were true, we could not any more expect a sharp Coulomb staircase in the dot charge, which clearly contradicts our intuition. In this sense, the self-consistent scattering theory cannot describe the degeneracy points exactly. In the rest of this chapter, we develop a theory beyond the mean field approximation and show that the effect of electron interaction is prominent at the degeneracy points.

## 4.3 Model

In this section, we first derive a bosonized model for the mesoscopic capacitor in the presence of strong electron interaction. Then we explain the way of estimating the charge relaxation resistance in the Matsubara formalizm. For comparison to the self-consistent scattering theory [19], the mean-field approximation for our bosonized model is also shown.

### 4.3.1 Bosonization

The mesoscopic capacitor of interest is shown in the left panel of Fig. 4.3. We first assume that the transport property of the system is mainly determined by the one-dimensionality near the center of the constriction. Then it is not necessary to treat exactly the two-dimensional regions in the quantum dot and the lead, so that we can consider the whole mesoscopic capacitor as a semi-infinite one-dimensional system, which is described by the (non-chiral) Tomonaga-Luttinger model. The present system is formulated by considering the open boundary condition on the closed end of the quantum dot [68]. Here, we instead derive the effective action in a different way; we consider a 1D quantum dot system with *two* point contacts and pinch off one of the point contacts later so that the boundary condition is satisfied. The bulk Hamiltonian for an *infinite* Tomonaga-Luttinger liquid is given by

$$H_0 = \int_{-\infty}^{\infty} \frac{\mathrm{d}x}{2\pi} \left[ \frac{v}{K} \left( \frac{\partial \phi}{\partial x} \right)^2 + vK \left( \frac{\partial \theta}{\partial x} \right)^2 \right]. \tag{4.13}$$

Here the canonically conjugated fields $\phi$ and $\theta$ satisfy the bosonic commutation relation $[\phi(x), \theta(x')] = (i\pi/2)\mathrm{sgn}(x - x')$, the Luttinger parameter $K$ describes short-range electron interaction around the constriction, and $v \equiv v_F/K$ denotes the sound velocity. We define a quantum dot in the range of $x_1 < x < x_2$ by locating point contacts at $x_1 = 0$ and $x_2 = L$ with barrier height $V_1$ and $V_2$, respectively. The electron scattering on the point contacts is expressed by the field operators of

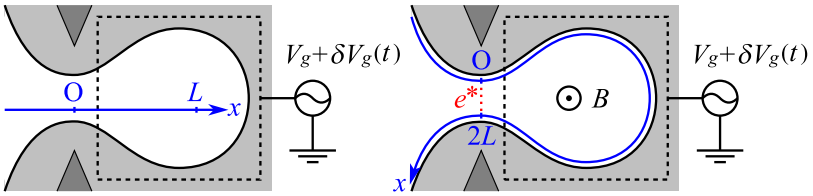


Figure 4.3: Schematic illustration of an open quantum dot (left panel) and a quantum Hall edge state (right panel).

a right(left)-moving electron $\psi_{+(-)}$ as

$$H_V = -\sum_{i=1,2} V_i[{\psi_+}^\dagger(x_i)\psi_-(x_i) + \text{H.c.}], \tag{4.14}$$

whose bosonized expression is given by

$$H_V = -\sum_i \frac{V_i}{\pi v_F} D\cos[2\{\phi(x_i) - k_F x_i\}], \tag{4.15}$$

with the bandwidth $D$. We take into account charging effect in the dot and capacitive coupling between the dot charge $Q$ and the (static) gate voltage $V_g$ by adding the Hamiltonian

$$H_C = \frac{Q^2}{2C_g} + QV_g \qquad \left(Q \equiv \frac{e}{\pi}[\phi(0) - \phi(L)]\right), \tag{4.16}$$

where $C_g$ is the geometrical capacitance within $x_1 < x < x_2$. By integrating out the fields away from $x_1$ and $x_2$, we arrive at the effective action in terms of $\phi_\pm \equiv \phi(x_1) \pm \phi(x_2)$ as in Ref. [33]:

$$\begin{aligned} S = &\frac{1}{2\pi K\beta}\sum_{\nu=\pm}\sum_{\omega_n}\frac{|\omega_n|}{1+\nu \mathrm{e}^{-\pi K|\omega_n|/\Delta}}|\tilde{\phi}_\nu(\omega_n)|^2 + \frac{1}{\pi^2}\frac{e^2}{2C_g}\int \mathrm{d}\tau\left[\phi_-(\tau) - \frac{\pi C_g V_g}{|e|}\right]^2 \\ &- \sum_i \frac{V_i D}{\pi v_F}\int \mathrm{d}\tau\cos[2\{\phi(x_i,\tau) - k_F x_i\}], \qquad (x_1 = 0,\ x_2 = L) \end{aligned} \tag{4.17}$$

where the Fourier transform of $\phi_\nu$ reads

$$\phi_\pm(\tau) \equiv \frac{1}{\beta}\sum_{\omega_n}\tilde{\phi}_\pm(\omega_n)\mathrm{e}^{-i\omega_n\tau}, \qquad \tilde{\phi}_\nu(\omega_n) = \int_0^\beta \mathrm{d}\tau\phi_\nu(\tau)\mathrm{e}^{i\omega_n\tau}. \tag{4.18}$$

Now we return to the problem of the mesoscopic capacitor with a single lead by pinching off the point contact at $x = x_2$, i.e., $V_2 \to \infty$. As a result, $\phi(x_2,\tau)$ is pinned at one of the minima of the cosine potential as

$$\phi(x_2,\tau) = k_F x_2 + m\pi \qquad (m = 0, \pm1, \pm2, \cdots). \tag{4.19}$$

We thus obtain the effective action for the mesoscopic capacitor written with a new field $\phi \equiv \phi_- + k_F x_2 = \phi_- + k_F L$:

$$S = S_{\text{kin}} + S_C + S_V \tag{4.20}$$

$$S_{\text{kin}} = \frac{1}{\pi K\beta}\sum_{\omega_n}\frac{|\omega_n|}{1-\mathrm{e}^{-2\pi K|\omega_n|/\Delta}}|\tilde{\phi}(\omega_n)|^2 \tag{4.21}$$

$$S_C = \frac{1}{\pi^2}E_C\int \mathrm{d}\tau[\phi(\tau) - \pi N_g]^2 \tag{4.22}$$

$$S_V = -V\int \mathrm{d}\tau\cos[2\phi(\tau)] \tag{4.23}$$

where $\Delta \equiv \pi v_F/L$ and $E_C \equiv e^2/2C_g$ are respectively the level spacing and the charging energy in the quantum dot. $V \equiv V_1 D/\pi v_F$ denotes the reflection strength of the point contact. $N_g \equiv {E_C}^{-1}[|e|V_g/2 + (k_F L/\pi)(E_C + \Delta/2K^2)]$ is the dimensionless gate voltage. We note that the above effective action can be also obtained in fractional quantum Hall edges shown in the right panel of Fig. 4.3 (see also Appendix A). We have already seen a model similar to Eq. (4.20) in Chapter 4, where the effective action (3.4) describes a *large* ($\Delta = 0$) quantum dot system with *spinful* electrons. Here we consider a quantum dot with finite size ($\Delta \neq 0$) in order to ensure coherent transport in the quantum dot, which is necessary for the half-quantization of the charge relaxation resistance.

It is worthwhile examining the frequency-dependence of the factor $\gamma(\omega_n) \equiv [1 - \mathrm{e}^{-2\pi K|\omega_n|/\Delta}]^{-1}$ in $S_{\rm kin}$, which is approximated in the high- and low-frequency regions as [33]

$$\gamma(\omega_n) \equiv \frac{1}{1 - \mathrm{e}^{-2\pi K|\omega_n|/\Delta}} \simeq \begin{cases} 1, & |\omega_n| \gg \Delta \\ \frac{\Delta}{2\pi K|\omega_n|} + \frac{1}{2}, & |\omega_n| \ll \Delta \end{cases} \tag{4.24}$$

For $\omega_1 = 2\pi T \gg \Delta$, discretization of the energy levels in the dot is smeared out by the thermal fluctuations, hence incoherent transport in the dot. Indeed the effective action for $\gamma(\omega_n) = 1$ takes the same form as that for a large quantum dot ($\Delta = 0$) with spinless electrons [23]. For $\omega_1 \ll \Delta$, on the other hand, the low-frequency behavior of $\gamma(\omega_n)$ gives two effects; shift of the charging energy $E_C$ by $\Delta/2K^2$ and multiplication of the interaction parameter $K$ by 2. It is in such a low-frequency regime that the half quantization of charge relaxation resistance is observed. Indeed the doubled interaction parameter is the origin of the prefactor $1/2$ in $R_q$ as we see in the following sections.

### 4.3.2 Linear admittance

We formulate admittance within the linear response theory by applying an oscillating gate voltage $V_g + \delta V_g(t)$ to the quantum dot. By calculating the dynamics of the dot charge $Q = (e/\pi)\phi_-$ under the oscillating field $H'(t) = Q\delta V_g(t)$, we obtain the admittance at frequency $\omega$

$$G(\omega) = G(i\omega_n \to \omega + i\delta) \tag{4.25}$$

$$G(i\omega_n) = \frac{e^2}{h}\frac{2|\omega_n|}{\pi}\int_0^\beta \mathrm{d}\tau \langle\phi(\tau)\phi(0)\rangle \mathrm{e}^{i\omega_n\tau} = \frac{e^2}{h}\frac{2|\omega_n|}{\pi\beta}\langle\phi(-\omega_n)\phi(\omega_n)\rangle. \tag{4.26}$$

In analogy to the classical $RC$ circuit, we split the impedance into the real part and the imaginary part

$$\frac{1}{G(\omega)} = R(\omega) + \frac{1}{-i\omega C(\omega)}. \tag{4.27}$$

Here we assumed that both the resistance $R$ and the capacitance $C$ in general depend on $\omega$. The $RC$ time defined as $\tau_{RC}(\omega) \equiv R(\omega)C(\omega)$ is the time scale of charge relaxation in the dot. If the the condition $\omega \ll 1/\tau_{RC}(\omega)$ holds, which is required for charge relaxation at frequency $\omega$, then the admittance can be expanded at low frequencies:

$$G(\omega) = -i\omega C(0) + \omega^2[\{C(0)\}^2 R(0) - iC'(0)] + \mathcal{O}(\omega^3). \tag{4.28}$$

Comparing this with the expansion (4.2), we find the relations

$$C_\mu = C(0), \qquad R_q = R(0)\left[1 - i\frac{C'(0)}{\tau_{RC}(0)C(0)}\right]. \tag{4.29}$$

If we assume that the ratio $C'(\omega)/C(\omega)$ diminishes faster than $\tau_{RC}(\omega)$ as $\omega \to 0$, we can estimate the charge relaxation resistance as $R_q \simeq R(\omega \to 0)$. In what follows we adopt this assumption. We should note that the expansion (4.28) is not always available because it is possible that $\tau_{RC}(\omega)$ diverges faster than $1/\omega$ with lowering $\omega$. In such a situation, $R(\omega \to 0)$ can not be interpreted as charge relaxation resistance in the sense that the gate voltage oscillates faster than charge relaxation occurs in the dot. Instead let us call $R(\omega \to 0)$ just *low-frequency resistance* so that it is well-defined whether the dot charge relaxes or not. We can estimate the low-frequency resistance using Eq. (4.27), or equivalently analytical continuation from the Matsubara representation:

$$R(\omega \to 0) = \lim_{i\omega_n \to 0} R(i\omega_n) \qquad \text{with} \qquad R(i\omega_n) \equiv \frac{1}{G(i\omega_n)} - \frac{1}{\omega_n C(i\omega_n)}. \tag{4.30}$$

Here $G(i\omega_n)$ has been already defined in Eq. (4.26), while we evaluate $C(i\omega_n \to 0)$ with the static capacitance, i.e.,

$$C_\mu = C(i\omega_n \to 0) = \frac{e^2}{\pi^2}\beta[\langle\bar{\phi}^2\rangle - \langle\bar{\phi}\rangle^2] \qquad \left(\bar{\phi} \equiv \frac{1}{\beta}\int_0^\beta \mathrm{d}\tau\phi(\tau)\right). \tag{4.31}$$

### 4.3.3 Mean field theory

To confirm that the effective action (4.20) correctly describe the mesoscopic capacitor, we here calculate the electrochemical capacitance $C_\mu$ within the Hartree approximation to reproduce the results obtained in the self-consistent scattering theory [19, 20]. In the Hartree approximation, it is assumed that fluctuation of the dot charge $\propto \phi(\tau) - \langle\phi\rangle$ is small enough that the term $\propto [\phi(\tau) - \langle\phi\rangle]^2$ is negligible. We thus obtain the mean-field effective action (4.20)

$$S_{\mathrm{MF}} = S_{\mathrm{kin}} + S_V + \frac{eU_g}{\pi}\int \mathrm{d}\tau\phi(\tau), \tag{4.32}$$

where

$$U_g \equiv V_g + \frac{2\langle\phi\rangle}{\pi e}E_C - \frac{2k_F L}{\pi^2}\left(E_C + \frac{\Delta}{2K^2}\right) \tag{4.33}$$

is the effective gate voltage coupled to the dot charge $\langle Q\rangle = (e/\pi)\langle\phi\rangle$. If the density of states in the quantum dot is denoted by $\mathcal{D}(\epsilon)$, variation of the dot charge is given by $\mathrm{d}\langle Q\rangle = -e^2\mathcal{D}(\epsilon)\mathrm{d}U_g$, so that Eq. (4.33) leads to the self-consistent condition for the effective gate voltage $U_g$:

$$-e^2\mathcal{D}(\epsilon)\mathrm{d}U_g = C_g(\mathrm{d}U_g - \mathrm{d}V_g), \tag{4.34}$$

By using this condition, one can easily reproduce the electrochemical capacitance in Refs. [19, 20]

$$C_\mu \equiv -\frac{\partial\langle Q\rangle}{\partial V_g} = \left(1 - \frac{C_\mu}{C_g}\right)e^2\mathcal{D}(\epsilon) \qquad \therefore \frac{1}{C_\mu} = \frac{1}{C_g} + \frac{1}{C_q}, \tag{4.35}$$

where $C_q \equiv e^2\mathcal{D}(\epsilon)$. If $K = 1$, the present model can be put back to the noninteracting electron system. Then the self-consistent scattering theory [19, 20] with the effective gate voltage $U_g$ defined in Eq. (4.33) leads to Eqs. (4.9) and (4.10). The reflection coefficient in the point contact is expressed using the parameter in the bosonized model (4.20) as $r = \pi V/D$ with the bandwidth $D$.

## 4.4 The path-integral Monte Carlo method

The setup of the path-integral Monte Carlo method that we describe here is similar to that for the impurity problem in a spinless TLL illustrated in Sec. 2.2. Using the discretized path $\phi_j \equiv \phi(j\beta/J)$ ($j = 0, 1, \cdots, J-1$) and its Fourier transform $\tilde{\phi}_k \equiv \sum_j \phi_j e^{(2\pi i/J)jk} - \pi J N_g(1 + \Delta/2K^2E_C)$, we obtain the discretized action

$$S = \sum_{k=0}^{J/2} \frac{1}{2{\sigma_k}^2}|\tilde{\phi}_k|^2 - V\tau_c \sum_{j=0}^{J} \cos[2\phi_j], \tag{4.36}$$

where $\tau_c \equiv \beta/J$ is the short time cutoff.

### 4.4.1 Local update

In a local update, for each $k$ a value of $\tilde{\phi}_k$ is randomly chosen following a normal distribution $\mathrm{e}^{-|\tilde{\phi}_k|^2/2{\sigma_k}^2}$ with variance

$$ {\sigma_0}^2 = \frac{\pi^2 J}{2(E_C + \Delta/2K^2)\tau_c}, \tag{4.37} $$

$$ {\sigma_{J/2}}^2 = \frac{1}{2}\left[\frac{1}{KJ}\frac{1}{1-\mathrm{e}^{-2\pi^2 K/\Delta\tau_c}} + \frac{E_C\tau_c}{\pi^2 J}\right]^{-1}, \tag{4.38} $$

$$ {\sigma_k}^2 = \frac{1}{4}\left[\frac{2k}{KJ^2}\frac{1}{1-\mathrm{e}^{-(2\pi)^2 K|k|/J\Delta\tau_c}} + \frac{E_C\tau_c}{\pi^2 J}\right]^{-1} \qquad (k \neq 0, J/2), \tag{4.39} $$

Then a new path $\phi_j$ is obtained from the inverse Fourier transform and is accepted with probability $p = \{1, \mathrm{e}^{-({S_V}^{\mathrm{new}} - {S_V}^{\mathrm{old}})}\}$.

### 4.4.2 Global update

The basic idea of the cluster algorithm is the same as that explained in Sec. 2.2.2 except that the present model has the charging energy. We rewrite the effective action in the imaginary-time representation

$$ S_{\mathrm{kin}} = -\sum_{j<j'} \kappa_{jj'}\phi_j\phi_{j'}, \tag{4.40} $$

$$ S_C = \frac{1}{\pi^2}E_C\tau_c\sum_{j=0}^{J-1}[\phi_j - \pi N_g]^2, \tag{4.41} $$

$$ S_V = -V\tau_c\sum_{j=0}^{j-1}\cos[2\phi_j], \tag{4.42} $$

where the interaction kernel $\kappa_{jj'}$ is defined as

$$ \kappa_{jj'} = -\frac{4}{KJ^2}\sum_{k=-J/2+1}^{J/2}\frac{|k|}{1-\mathrm{e}^{-(2\pi)^2 K|k|/J\Delta\tau_c}}\mathrm{e}^{-\frac{2\pi i}{J}k(j-j')}. \tag{4.43} $$

Each pair of $j$th and $j'$th sites is connected with bond probability

$$ p_{jj'} = \max\{0, 1-\mathrm{e}^{-2\kappa_{jj'}(\phi_j-\pi/2)(\phi_{j'}-\pi/2)}\}, \tag{4.44} $$

and then all the sites $\phi_j$ are flipped with respect to $\phi^{\mathrm{mirror}} = \pi/2$, i.e., ${\phi_j}^{(\mathrm{new})} = \pi - {\phi_j}^{(\mathrm{old})}$.

## 4.5 Results and discussion

In this section, we investigate the dynamic response of the mesoscopic capacitor described by the effective action (4.20) using analytical and numerical approaches. In the small barrier limit $V \to 0$, the capacitance $C_\mu$ and the charge relaxation resistance $R_q$ is calculated perturbatively in $V$ [1]. In the large barrier limit $V \to \infty$, on the other hand, we consider the tunneling of an electron through the point contact as perturbation and discuss scaling of tunneling strength and charge fluctuation. Finally, we demonstrate the path-integral Monte Carlo simulation to study the intermediate region directly.

### 4.5.1 Weak barrier limit: Perturbation theory

It is clear from Eq. (4.26) that if we can estimate the correlation function $c(\omega_n) \equiv \langle\phi(-\omega_n)\phi(\omega_n)\rangle$, we can calculate the linear admittance of the mesoscopic capacitor as

$$G(i\omega_n) = \frac{e^2}{h}\frac{2|\omega_n|}{\pi\beta}c(\omega_n). \tag{4.45}$$

However, estimation of correlation functions is in general not an easy task. In our case, reflection of electrons on the point contact causes a cosine potential for the field $\phi$, which makes it difficult to solve the problem exactly. Here we focus on the weak barrier limit $V \to 0$ and develop a perturbation theory. We calculate the admittance up to second order in $V$ and evaluate the electrochemical capacitance $C_\mu = {C_\mu}^{(0)} + {C_\mu}^{(1)} + {C_\mu}^{(2)}$ and the charge relaxation resistance $R_q = {R_\mu}^{(0)} + {R_q}^{(1)} + {R_q}^{(2)}$.

We begin with the partition function in the path-integral representation

$$Z[\xi] = \int \mathscr{D}\phi \exp\left[-S - \frac{1}{\beta}\sum_{\omega_n}\xi(-\omega_n)\tilde{\phi}(\omega_n)\right], \tag{4.46}$$

where $S$ is the effective action (4.20). $\xi$ is the counting field and will be set to zero in the end of the calculation. One can check that the correlation function $c(\omega_n)$ is expressed in terms of the partition function (4.46) as

$$c(\omega_n) \equiv \langle\phi(-\omega_n)\phi(\omega_n)\rangle = \beta^2\frac{1}{Z[\xi]}\frac{\partial^2 Z[\xi]}{\partial\xi(\omega_n)\partial\xi(-\omega_n)}\bigg|_{\xi\to 0}. \tag{4.47}$$

[1] The results in 4.5.1 are based on calculation by one of the collaborators, T. Jonckheere.

The perturbative expansion of the right hand side in orders of $V$ reads

$$\beta^2 \frac{1}{Z^{(0)}+Z^{(1)}+Z^{(2)}+\cdots} \frac{\partial^2 (Z^{(0)}+Z^{(1)}+Z^{(2)}+\cdots)}{\partial\xi(\omega_n)\partial\xi(-\omega_n)} \tag{4.48}$$

$$\begin{aligned}
&= \beta^2 \frac{1}{Z^{(0)}} \frac{\partial^2 Z^{(0)}}{\partial\xi(\omega_n)\partial\xi(-\omega_n)} \\
&\quad + \beta^2 \frac{1}{Z^{(0)}} \left[ \frac{\partial^2 Z^{(1)}}{\partial\xi(\omega_n)\partial\xi(-\omega_n)} - \frac{Z^{(1)}}{Z^{(0)}} \frac{\partial^2 Z^{(0)}}{\partial\xi(\omega_n)\partial\xi(-\omega_n)} \right] \\
&\quad + \beta^2 \frac{1}{Z^{(0)}} \left[ \frac{\partial^2 Z^{(2)}}{\partial\xi(\omega_n)\partial\xi(-\omega_n)} - \frac{Z^{(2)}}{Z^{(0)}} \frac{\partial^2 Z^{(0)}}{\partial\xi(\omega_n)\partial\xi(-\omega_n)} \right. \\
&\qquad \left. - \frac{Z^{(1)}}{Z^{(0)}} \left\{ \frac{\partial^2 Z^{(1)}}{\partial\xi(\omega_n)\partial\xi(-\omega_n)} - \frac{Z^{(1)}}{Z^{(0)}} \frac{\partial^2 Z^{(0)}}{\partial\xi(\omega_n)\partial\xi(-\omega_n)} \right\} \right] + \cdots ,
\end{aligned} \tag{4.49}$$

where $Z^{(m)}$ denotes $m$th order contribution to the partition function. From this, we obtain perturbative contributions to the correlation function up to second order:

$$c^{(0)}(\omega_n) \equiv \beta^2 \frac{1}{Z^{(0)}} \frac{\partial^2 Z^{(0)}}{\partial\xi(\omega_n)\partial\xi(-\omega_n)} \tag{4.50}$$

$$c^{(1)}(\omega_n) \equiv \beta^2 \frac{1}{Z^{(0)}} \frac{\partial^2 Z^{(1)}}{\partial\xi(\omega_n)\partial\xi(-\omega_n)} - \frac{Z^{(1)}}{Z^{(0)}} c^{(0)}(\omega_n) \tag{4.51}$$

$$c^{(2)}(\omega_n) \equiv \beta^2 \frac{1}{Z^{(0)}} \frac{\partial^2 Z^{(2)}}{\partial\xi(\omega_n)\partial\xi(-\omega_n)} - \frac{Z^{(2)}}{Z^{(0)}} c^{(0)}(\omega_n) - \frac{Z^{(1)}}{Z^{(0)}} c^{(1)}(\omega_n). \tag{4.52}$$

To calculate each contribution $c^{(m)}$, we need to evaluate $Z^{(m)}$ and its second derivative $\partial^2 Z^{(m)}/\partial\xi(-\omega_n)\partial\xi(\omega_n)$. For this purpose, let us first express the total action in the following form

$$S_{\rm kin} + S_C + S_V + \frac{1}{\beta} \sum_{\omega_n} \xi(-\omega_n)\tilde{\phi}(\omega_n) \tag{4.53}$$

$$\begin{aligned}
&= \frac{1}{\beta} \sum_{\omega_n} \left[ \tilde{\phi}(-\omega_n) A(\omega_n) \tilde{\phi}(\omega_n) + \left\{ \xi(-\omega_n) - \frac{2N_g\delta_{n0}}{\pi} \beta E_C \right\} \tilde{\phi}(\omega_n) \right] \\
&\quad - \frac{V}{2} \sum_{\sigma=\pm} \int {\rm d}\tau \exp\left[ \frac{2i\sigma}{\beta} \sum_{\omega_n} \tilde{\phi}(\omega_n) {\rm e}^{-i\omega_n\tau} \right]
\end{aligned} \tag{4.54}$$

with

$$A(\omega_n) \equiv \frac{1}{\pi K} \frac{|\omega_n|}{1-{\rm e}^{-2\pi K|\omega_n|/\Delta}} + \frac{1}{\pi^2} E_C. \tag{4.55}$$

Expanding $Z[\xi]$ in $V$ and performing the path integral in $\phi$, we obtain

$$Z^{(m)}[\xi] = \frac{1}{m!}\left(\frac{V}{2}\right)^m \sum_{\sigma_1=\pm}\cdots\sum_{\sigma_m=\pm}\int \mathrm{d}\tau_1\cdots\mathrm{d}\tau_m \times \mathrm{e}^{-\frac{1}{\beta}\sum_{\omega_n}\left[\frac{1}{2}\xi(-\omega_n)-\frac{N_g\delta_{n0}\beta E_C}{\pi}-i\sum_{l=1}^m\sigma_l\mathrm{e}^{-i\omega_n\tau_l}\right]\frac{1}{A(\omega_n)}\left[\frac{1}{2}\xi(\omega_n)-\frac{N_g\delta_{n0}\beta E_C}{\pi}-i\sum_{l=1}^m\sigma_l\mathrm{e}^{i\omega_n\tau_l}\right]} \tag{4.56}$$

$$\xrightarrow{\xi\to 0} \frac{1}{m!}\left(\frac{V}{2}\right)^m \sum_{\sigma_1\cdots\sigma_m}\int \mathrm{d}\tau_1\cdots\mathrm{d}\tau_m \times \mathrm{e}^{-\frac{1}{\beta}\sum_{\omega_n}\left[\frac{N_g\delta_{n0}\beta E_C}{\pi}+i\sum_l\sigma_l\mathrm{e}^{-i\omega_n\tau_l}\right]\frac{1}{A(\omega_n)}\left[\frac{N_g\delta_{n0}\beta E_C}{\pi}+i\sum_l\sigma_l\mathrm{e}^{i\omega_n\tau_l}\right]}. \tag{4.57}$$

Then the second derivative of $Z^{(m)}[\xi]$ reads

$$\frac{\partial^2 Z^{(m)}[\xi]}{\partial\xi(\omega_n)\partial\xi(-\omega_n)} \tag{4.58}$$

$$= \frac{Z^{(m)}[\xi]}{2\beta A(\omega_n)} + \frac{1}{m!}\left(\frac{V}{2}\right)^m \sum_{\sigma_1\cdots\sigma_m}\int \mathrm{d}\tau_1\cdots\mathrm{d}\tau_m \frac{1}{[A(\omega_n)]^2} \times\left[\frac{1}{2}\xi(-\omega_n)-\frac{N_g\delta_{n0}}{\pi}\beta E_C - i\sum_l\sigma_l\mathrm{e}^{-i\omega_n\tau_l}\right]\left[\frac{1}{2}\xi(\omega_n)-\frac{N_g\delta_{n0}}{\pi}\beta E_C - i\sum_l\sigma_l\mathrm{e}^{i\omega_n\tau_l}\right] \times \mathrm{e}^{\frac{1}{\beta}\sum_{\omega_n}\left[\frac{1}{2}\xi(-\omega_n)-\frac{N_g\delta_{n0}\beta E_C}{\pi}-i\sum_l\sigma_l\mathrm{e}^{-i\omega_n\sigma_l}\right]\frac{1}{A(\omega_n)}\left[\frac{1}{2}\xi(\omega_n)-\frac{N_g\delta_{n0}\beta E_C}{\pi}-i\sum_l\sigma_l\mathrm{e}^{i\omega_n\sigma_l}\right]} \tag{4.59}$$

$$\xrightarrow{\xi\to 0} \frac{Z^{(m)}[0]}{2\beta A(\omega_n)} + \frac{1}{m!}\left(\frac{V}{2}\right)^m \sum_{\sigma_1\cdots\sigma_m}\int \mathrm{d}\tau_1\cdots\mathrm{d}\tau_m \frac{1}{[A(\omega_n)]^2} \times\left[\frac{N_g\delta_{n0}}{\pi}\beta E_C + i\sum_l\sigma_l\mathrm{e}^{-i\omega_n\tau_l}\right]\left[\frac{N_g\delta_{n0}}{\pi}\beta E_C + i\sum_l\sigma_l\mathrm{e}^{i\omega_n\tau_l}\right] \times \mathrm{e}^{\frac{1}{\beta}\sum_{\omega_n}\left[\frac{N_g\delta_{n0}}{\pi}\beta E_C+i\sum_l\sigma_l\mathrm{e}^{-i\omega_n\sigma_l}\right]\frac{1}{A(\omega_n)}\left[\frac{N_g\delta_{n0}}{\pi}\beta E_C+i\sum_l\sigma_l\mathrm{e}^{i\omega_n\sigma_l}\right]}. \tag{4.60}$$

Substituting Eqs. (4.57) and (4.60) into the the correlation functions in each order (4.50)-(4.52), we can expand perturbatively the admittance (4.45) as

$$G^{(0)}(\omega_n) = \frac{e^2}{h}\frac{|\omega_n|}{\pi}\frac{1}{A(\omega_n)}, \tag{4.61}$$

$$G^{(1)}(\omega_n) = -\frac{e^2}{h}\frac{|\omega_n|}{\pi}\frac{2V}{[A(\omega_n)]^2}\sqrt{F_+(0)}\cos 2\pi N, \tag{4.62}$$

$$G^{(2)}(\omega_n) = \frac{e^2}{h}\frac{|\omega_n|}{\pi}\frac{2V^2}{[A(\omega_n)]^2}F_+(0)I(\omega_n), \tag{4.63}$$

where we have defined two functions

$$F_{\pm}(\tau) \equiv \exp\left[-\frac{1}{\beta}\sum_{\omega_n}\frac{\pm 2}{A(\omega_n)}\cos\omega_n\tau\right], \tag{4.64}$$

$$I(\omega_n) \equiv \int_0^{\beta/2} \mathrm{d}\tau[\{1-F_+(\tau)(1+\cos\omega_n\tau)\}\cos 2\pi N + \{1-F_-(\tau)(1-\cos\omega_n\tau)\}] \tag{4.65}$$

and redefined the dimensionless gate voltage $N$ as

$$N \equiv \frac{E_C}{E_T}N_g = \frac{|e|V_g}{2E_T} + \frac{k_F L}{2} \qquad \text{with} \qquad E_T = E_C + \frac{\Delta}{2K^2}. \tag{4.66}$$

The fact that Eqs. (4.61)-(4.63) are analytic at $\omega_n \to 0$ means that one can always expand the admittance at low frequency as Eq. (4.2) in the small barrier limit $V \to 0$. As a result the charge relaxation resistance is well-defined as the factor $R_q$ in the term proportional to ${\omega_n}^2$. Performing the Maclaurin expansion for the admittance, we obtain perturbative contributions up to second order to the electrochemical capacitance

$${C_\mu}^{(0)} = \frac{e^2}{h}\frac{\pi}{E_T} \tag{4.67}$$

$${C_\mu}^{(0)} = -{C_\mu}^{(0)}\frac{2\pi^2}{E_T}V\sqrt{F_+(0)}\cos 2\pi N \tag{4.68}$$

$${C_\mu}^{(0)} = {C_\mu}^{(0)}\frac{2\pi^2}{E_T}V^2F_+(0)I(\omega_n \to 0)\cos 4\pi N \tag{4.69}$$

and the charge relaxation resistance

$${R_q}^{(0)} = \frac{h}{2Ke^2}, \qquad {R_q}^{(1)} = 0, \qquad {R_q}^{(2)} = 0. \tag{4.70}$$

It is clear from Eqs. (4.67)-(4.69) that one Coulomb oscillation occurs in the electrochemical capacitance ${C_\mu}^{(0)} + {C_\mu}^{(1)} + {C_\mu}^{(2)}$ while $N$ is shifted by 1, i.e., the electrochemical potential $eV_g$ is shifted by the expanded level spacing $2E_T = 2E_C + \Delta/K^2$. Thus we focus on the interval $0 \le N < 1$ in the rest of this chapter. At zero temperature, the sums and the integration of Eqs. (4.64) and (4.65) can be done analytically in certain cases. For example, in the case of $K = 1$ one has $F_+(0) = (E_T/\pi D)^2$ if $E_C, \Delta \ll D$, so that one can show that

$$C_\mu = \frac{e^2}{2E_T}\lambda(N) \tag{4.71}$$

where $\lambda(N) = 1 - 2r\cos 2\pi N + 2r^2 \cos 4\pi N$ is the oscillating factor with the reflection coefficient $r \simeq \pi V/D$. Eq. (4.71) suggests that the electrochemical capacitance is the serial combination of two capacitances

$$C_g\lambda(N) \qquad \text{and} \qquad C_q \equiv \frac{e^2}{\Delta}\lambda(N), \tag{4.72}$$

both of which similarly oscillate as $\lambda(N)$. It is instructive to compare this result with that of the mean field theory [19], where the electrochemical capacitance $C_\mu$ is split into a *constant* geometrical capacitance $C_g$ and an oscillating quantum capacitance $C_q$, unlike in Eq. (4.72). $C_q$ in Eq. (4.72) coincides with the development of the noninteracting formula (4.12) in powers of $r$. Thus the inconsistency between the perturbation theory and the mean field theory is that the geometrical capacitance $C_g$ is multiplied by the oscillating factor $\lambda(N)$ in the former case. This reflects the fact that the mean field theory neglects charge fluctuations due to charging effect, which is in fact enhanced near the degeneracy point $N = 1/2$, i.e., $\langle Q\rangle \simeq e/2$. Indeed, in the weak barrier limit $r \to 0$, the deviation of $\lambda(N)$ from 1 remains small for $N \neq 1/2$, whereas it becomes large for $N = 1/2$.

Eq. (4.70) indicates that the charge relaxation resistance $R_q$ is quantized at $h/2Ke^2$ per channel irrespective of the barrier height $V$ and the gate voltage $V_g$ (at least in the weak barrier limit $V \to 0$). In particular at $K = 1$ we reproduces $R_q = h/2e^2$ predicted in Refs.[19, 21]. Surprisingly, the universal quantization is exact up to second order in $V$, which implies that this behavior is preserved in higher orders. In addition, we can see from Eq. (4.70) that the long-range interaction in the dot $E_C$ has no influence on $R_q$, while the bulk short-range interaction described by $K$ explicitly modifies the quantized value of $R_q$.

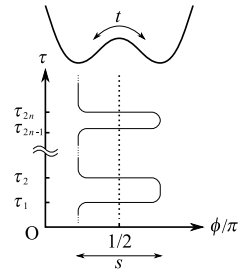


Figure 4.4: Typical path of $\phi$ near the degeneracy point $\langle Q\rangle \simeq e/2$ in the strong barrier limit $V \to \infty$. $s$ and $t$ denotes the width and the tunneling coefficient between the potential minima, respectively.

### 4.5.2 Strong barrier limit: Renormalization group

In the strong barrier limit, the lead and the quantum dot are almost disconnected, so that most of electrons incident to the point contact are reflected. In this limit, we can treat the transmission coefficient $t$ perturbatively. Near the degeneracy point $\langle Q\rangle \simeq e/2$ the bosonic field $\phi$ is subject to a double well potential whose minima corresponds to the two charge states $\langle Q\rangle \simeq 0$ and $\langle Q\rangle \simeq e/2$ as shown in Fig. 4.4. $\phi$ spends most of the time in either of the minima and sometimes a kink structure between them appears for infinitesimally short time. In such a situation, we can employ the dilute instanton gas approximation (DIGA) [46] and express the path with $n$ pairs of instanton and anti-instanton as

$$\phi(\tau) \simeq \pi \sum_{j=1}^{2n} s_j \Theta(\tau - \tau_j) + \frac{\pi}{2}(1 - s) \tag{4.73}$$

where $\Theta(\tau - \tau_j)$ is the step function describing a kink structure at the imaginary time $\tau_j$. $s$ is the width between the well minima ($0 \le s \le 1$) as shown in Fig. 4.4, and $s_j \equiv s(-1)^{j-1}$ represents the "charge" of an (anti-)instanton. Note that the expression (4.73) has reduced the degrees of freedom of the path to a set of $(s_j, \tau_j)$'s, and as a result the perpendicular parts of the path in Fig. 4.4 are of less importance. We will take into account the shape of an instanton later. Let us derive the effective action in the DIGA representation by substituting Eq. (4.73) to Eq. (4.20). First, the Fourier transform of the step function $\Theta(\tau) = (i/\beta)\sum_{\omega_n} \mathrm{e}^{-i\omega_n\tau}/(\omega_n + i\eta)$ leads to the kinetic term written with $s_j$ and $\tau_j$:

$$S_{\mathrm{kin}} = \frac{\pi}{K\beta} \sum_{j\neq k} s_j s_k \sum_{\omega_n} \frac{\mathrm{e}^{i\omega_n(\tau_j - \tau_k)}}{|\omega_n|(1 - \mathrm{e}^{-2\pi K|\omega_n|/\Delta})}. \tag{4.74}$$

Since the long-time property of the system is important at low energy, the high-frequency terms in $\sum_{\omega_n}$ contribute little to the sum, hence a high-energy cutoff $\sim |\tau_j - \tau_k|^{-1}$. Then recalling the relation (4.24), we can split the kinetic term into two parts at low frequencies $|\omega_n| \ll |\tau_j - \tau_k|^{-1} \ll \Delta$:

$$S_{\mathrm{kin}} \simeq \frac{\pi}{K\beta} \sum_{j\neq k} s_j s_k \sum_{\omega_n} \left( \frac{1}{2|\omega_n|} + \frac{\Delta}{2\pi K} \frac{1}{{\omega_n}^2} \right) \mathrm{e}^{i\omega_n(\tau_j - \tau_k)} \tag{4.75}$$

$$= -\frac{1}{2K} \sum_{j\neq k} s_j s_k \log \left| \frac{\tau_j - \tau_k}{\tau_c} \right| - \frac{\Delta}{2K^2} \sum_j s_j \tau_j. \tag{4.76}$$

With respect to $S_V$ and $S_C$, on the other hand, we can make most of the fact that $\cos[2\phi(\tau)]$ and $[\phi(\tau) - \pi/2]^2$ are approximately independent of $\tau$. Therefore $S_V$ is

almost constant, while $S_C$ can be rewritten as

$$S_C \simeq (2N_g - 1)E_C \sum_j s_j \tau_j, \tag{4.77}$$

where we have neglected some constant terms. Finally, we assume that the detailed shapes of instantons are characterized by a single parameter, i.e., tunneling amplitude $t \sim \mathrm{e}^{-S_{\mathrm{inst}}}$. We thus complete the DIGA of the effective action for the path with $2n$ (anti-)instantons. The partition function of the system is given by

$$\begin{aligned} Z = \sum_{n=0}^{\infty} \left(\frac{t}{\tau_c}\right)^{2n} \int_0^{\beta} \mathrm{d}\tau_{2n} \int_0^{\tau_{2n}} \mathrm{d}\tau_{2n-1} \cdots \int_0^{\tau_2} \mathrm{d}\tau_1 \\ \times \exp\left[\frac{s^2}{2K} \sum_{j\neq k} (-1)^{j-k} \log\left|\frac{\tau_j - \tau_k}{\tau_c}\right| - us \sum_j (-1)^{j-1} \tau_j\right] \end{aligned} \tag{4.78}$$

where $u \equiv (2N - 1)E_T$ denotes the small deviation from the degeneracy point. Note that partition functions similar to Eq. (4.46) also appear in the context of the Kondo problem [46], one-dimensional long-range Ising chains [47], and dissipative Josephson junctions [49], which suggests a potential phase transition in the mesoscopic capacitor. Indeed, if we assume that $t$ is perturbatively small, we can identify the scaling equations using the renormalization group technique [46, 49]:

$$\frac{\mathrm{d}t}{\mathrm{d}l} = \left(1 - \frac{s^2}{2K}\right)t, \qquad \frac{\mathrm{d}s^2}{\mathrm{d}l} = -4s^2t^2, \tag{4.79}$$

$$\frac{\mathrm{d}us}{\mathrm{d}l} = us(1 - 2t^2) \tag{4.80}$$

which are familiar in the context of a Kosterlitz Thouless transition in the two-dimensional XY model.

Let us first focus on Eq. (4.80), which suggests that no further arguments are needed when one deviates from the degeneracy point, i.e., $u \neq 0$. The double-well potential due to $S_C + S_V$ approximates near the degeneracy point $N \simeq 1/2$ as

$$-\frac{1}{\pi} u \left[\phi(\tau) - \frac{\pi}{2}\right] - V \cos[2\phi(\tau)], \tag{4.81}$$

so that the difference between the two lowest minima is of the order of $u$ as shown in the left panned of Fig. 4.5. At high temperatures, this difference is blurred by thermal fluctuations and the two charge states remain almost degenerate. Upon decreasing temperature, however, the difference between the two minima further increases because Eq. (4.80) predicts that $u \neq 0$ is always relevant. Thus, a crossover occurs around some temperature $\sim u$, below which excitations from

the lower minimum ($\phi \sim \pi$) to the higher ($\phi \sim 0$) are exponentially suppressed. As a result, the system reaches a fixed point with an integral number of dot electrons at $T = 0$. At the fixed point, $\phi$ is trapped in an effective harmonic potential shown as a dotted curve in Fig. 4.5. This situation is quite similar to the case of zero backscattering $V = 0$, which we have already discussed in Sec. 4.5.1. Therefore we can conclude from Eq. (4.70) that the charge relaxation resistance is always

$$R_q = \frac{h}{2Ke^2} \qquad (u \neq 0). \tag{4.82}$$

Note that this result is independent of Eqs. (4.79), and only the flow of $u$ is important for its universality. In addition, the effective harmonic potential suppresses the charge fluctuation as $T \to 0$ and, as a result, always validates the two-capacitor picture in Fig. 4.2 except for $u = 0$.

For the charge degenerate case $N = 1/2 (u = 0)$, $u$ is marginal and therefore Eqs. (4.79), called the Kosterlitz equations, determine the low-energy properties of the mesoscopic capacitor. This case is related to the Kondo problem in the sense that the neighboring two charge states act as a pseudo spin. It is well-known that for small $B \equiv 1 - s^2/2K$, the solution of Eqs. (4.79) is a set of hyperbolic curves shown in Fig. 4.5:

$$B^2 - 4t^2 = \text{const.} \tag{4.83}$$

and the system undergoes the Kosterlitz-Thouless (KT) transition when crossing the separatrix $2t + B = 0$. One can see from Fig. 4.5 that if $2t + B > 0$, $t \to \infty$ and $s^2 \to 0$, while otherwise $t \to 0$ and $s^2 \to$ const. For $K > 1/2$, the tunneling strength $t$ always grows upon reducing the temperature, and the system reaches the Kondo fixed point where the dot is strongly coupled to the reservoir. An electron freely tunnels in and out of the dot irrespective of the initial barrier height $V$.

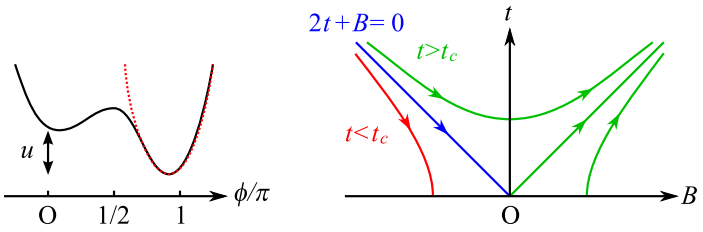


Figure 4.5: (left) Double-well potential away from the degeneracy point $N = 1/2$. The difference between the two minima is of the order of $u$. (right) Flow diagram for the tunneling amplitude $t$ and $B \equiv 1 - s^2/2K$. The tendency of the flow changes on the separatrix $2t + B = 0$.

We again arrive at the case where $V = 0$ is effectively achieved as in the non-degenerate case $u \neq 0$ [2] and therefore

$$R_q = \frac{h}{2Ke^2} \qquad (u = 0, K > 1/2). \tag{4.84}$$

In particular at $K = 1$, by combining Eq. (4.82) and Eq. (4.84), we can reproduce the quantized charge relaxation resistance $R_q = h/2e^2$ irrespective of the barrier height $V$ nor the gate voltage $V_g$ [19, 21]. However we should emphasize that in the present picture the universal $R_q$ at $u = 0$ is due to the Kondo effect associated with the pseudo spin. In the mean field theories [19, 21], on the other hand, the universality results from the mean field approximation, which is generally invalid at the degeneracy point $u = 0$ ($N = 1/2$) doe to large charge fluctuations. However at $K = 1 (> 1/2)$ the Kondo effect also suppresses the charge fluctuation $\sim s^2 \to 0$, and the mean field approximation is validated accidentally. This suggests that if $s^2$ remains finite at $T = 0$, the charge relaxation resistance may not be universal at $u = 0$. Indeed, for $K < 1/2$ there is the possibility that at sufficiently weak transmission $t$ (large $V$), the RG flow always drives the system into a weak coupling configuration with specified charge. Then the charge fluctuation remains finite, so that the capacitance diverges as $C_\mu \sim \beta s^2 \propto T^{-1}$. This situation corresponds to the region $2t + B < 0$ in Fig. 4.5. The KT transition of a static occupation $\langle Q \rangle / e$ in a similar setup has been predicted in Ref. [69]. We will discuss how the KT transition influences a dynamic property of the mesoscopic capacitor in the next section.

### 4.5.3 Intermediate region: The PIMC method

In the weak barrier limit (Sec. 4.5.1), the perturbation theory has proved that the charge relaxation resistance is universal ($R_q = h/2e^2$) even in the presence of interactions. In the strong barrier limit (Sec. 4.5.2), on the other hand, the RG treatment indicates that, if $K < 1/2$, the system undergoes the KT transition at the degeneracy point. To study the non-perturbative regime, we apply the path-integral Monte Carlo to the action for the discretized path $\phi(\tau = j\tau_c)$ ($j = 0, 1, \cdots, J - 1$) with the short-time cutoff $\tau_c$. In what follows, we use the parameters $D\tau_c = 2\pi$ and $E_C\tau_c = \Delta\tau_c/2K^2 = (\pi/2)^2$. The top (bottom) row of Fig. 4.6 shows the calculated capacitance $C_\mu$ as a function of $V$ at $J = 100$ and $K = 1$ ($K = 1/3$). The left and right columns correspond to the non-degenerate case ($N = 0$) and the charge degenerate case ($N = 1/2$), respectively. With increasing $V$ the Coulomb staircase becomes sharper, which results in the decrease (increase) in $C_\mu \equiv -\partial\langle Q \rangle / \partial V_g$ in

[2] However, the present case is different from the case of $u \neq 0$ in that the universality is essentially due to the renormalization of $t$ or $V$, not that of $u$.

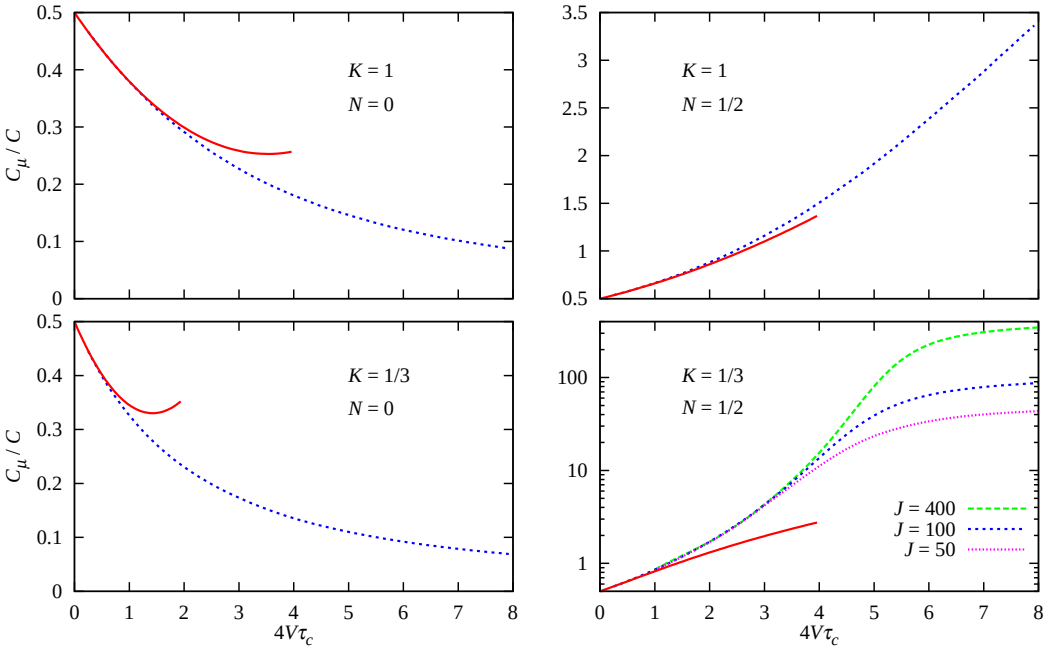


Figure 4.6: Capacitance $C_\mu$ as a function of the backscattering strength $V$ obtained as inverse temperature $J = 100$ with Monte Carlo computations (dashed lines). The solid lines show the predictions of the perturbative calculations up to second order. Temperature dependence is shown in the bottom right panel, where the vertical axis is measured on a logarithmic scale.

the case of $N = 0$ ($N = 1/2$). The second-order perturbation theory, shown as solid lines, displays an excellent agreement for small $V$. Especially, it is remarkable that only for the case of $K = 1/3$ and $N = 1/2$ (the right bottom panel of Fig. 4.6), $C_\mu$ exhibits an abrupt increase at a finite $V$, signaling the KT transition mentioned in Sec. 4.5.2. Indeed, one can see that $C_\mu$ grows as $\propto 1/T$ in the large barrier region, reflecting finite charge fluctuation $\sim s^2$.

We now describe the effect of the KT transition on the dynamical properties. As described in Sec. 4.3.2, the low-frequency resistance $R(\omega \to 0)$ of the point contact can be estimated from analytical continuation of the impedance in the Matsubara representation:

$$R(i\omega_n) \equiv \frac{1}{G(i\omega_n)} - \frac{1}{\omega_n C_\mu}, \tag{4.85}$$

where $G(i\omega_n)$ and $C_\mu$ are defined in Eqs. (4.26) and (4.31), respectively. To obtain the value of $R(\omega \to 0) = R(i\omega_n \to 0)$ by analytical continuation, we plot $R(i\omega_n)$ as a function of $\omega_n$ and extrapolate first five points into $\omega_n \to 0$. Note that $\tau_{RC} =$

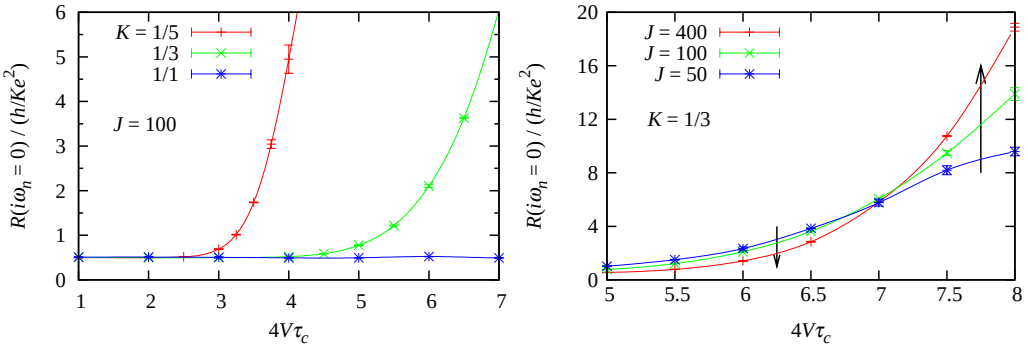


Figure 4.7: Extrapolated value $R(i\omega_n \to 0)$ as a function of $V$ at inverse temperature $J = 100$ in the degenerate case. The results at $J = 100$ for $K = 1$, 1/3, and 1/5 are shown in the left panel, while those at $J = 50$, 100, and 400 for $K = 1/3$ are shown in the right panel. The arrows represents the temperature dependence as $T \to 0$ ($J \to \infty$).

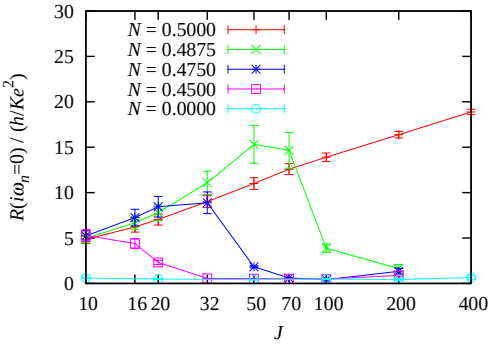


Figure 4.8: Temperature dependence of $R(i\omega_n \to 0)$ at $4V\tau_c = 8$ and $K = 1/3$. The results at the degenerate case $N = 0.5$ and the non-degenerate cases $N = 0, 0.45, 0.475$ and $0.4875$ are shown.

$R(0)C_\mu$. In the left panel of Fig. 4.7, we plot $R(0)$ for $K = 1, 1/3$ and $1/5$ as a function of $V$ at temperature $J = 100$. For $K = 1$, $R(0)$ equals $h/2e^2$ irrespective of $V$, in agreement with the universal charge relaxation resistance [19, 21]. For $K = 1/3$ and $1/5$, the same behavior is observed in the weak barrier region, whereas $R(0)$ is abruptly enhanced with increasing $V$, reflecting the RG flow to the weak coupling regime due to the KT transition. The temperature dependence of $R(0)$ for $K = 1/3$ is shown in the right panel of Fig 4.7, which indicates that $R(0)$ diverges as $T \to 0$ ($J \to \infty$) in the strong barrier region.

As mentioned in the previous subsection, in the non-generate case $u \neq 0$, the divergence of $R(0)$ stops at some temperature and the system crossovers to a fixed point with an integral number of dot electrons. In Fig. 4.8, we plot temperature dependence of $R(0)$ for $4V\tau_c = 8$ and $K = 1/3$ in the non-degenerate cases $N = 0, 0.45, 0.475$ and $0.4875$. For comparison, monotonic increase in $R(0)$ in the degenerate case $N = 0.5$ is also shown. the large error bars reflect the fact that

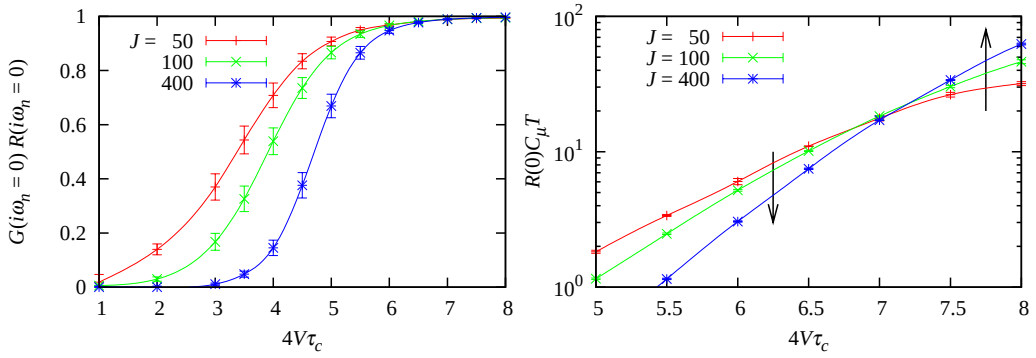


Figure 4.9: Product $G(i\omega_n = 0)R(i\omega_n = 0)$ and ratio $\tau_{RC}/\tau_{\rm coh} = R(i\omega_n = 0)C_\mu T$ for $K = 1/3$ as a function of the backscattering strength $V$, for different inverse temperatures $J$. The crossing of the curves in the right panel gives a good estimate of the transition point.

the cluster algorithm is not suitable to asymmetric potentials especially near the corssover temperature. The crossover temperatures can be estimated from $T_c \sim u$, i.e., $J_c \sim 1/|2N-1|E_T\tau_c = 1/\pi^2|N-1/2|$. One can see from the data for $N = 0.45, 0.475$ and $0.4875$ that the starting points of crossover shifts as $\propto 1/|N-1/2|$ as expected.

The KT transition plays a crucial role in the relevance of the universal charge relaxation resistance. If $2t + B > 0$, the system scales to the weak barrier limit, where $\tau_{RC}$ is independent of temperature. If $2t + B < 0$, on the other hand, the scaling equations (4.79) predict $s^2 \to$ const. and $t \propto T^{-B}$, so that $\tau_{RC}$ roughly scales as $\propto T^{-1}(T^{2B} + \text{const.})$, which grows faster than the (thermal) coherence time $\tau_{\rm coh} \propto 1/T$ as temperature is lowered. These observations suggest that if $2t + B > 0$ coherent transport can be realized by lowering temperature to guarantee $\tau_{RC} < \tau_{\rm coh}$, while if $2t + B < 0$ electronic transport in the dot decoheres before charge relaxation is achieved. In the latter case, the quantum dot effectively acts as a reservoir and consequently the dynamical property of the system is governed by transport through the point contact between the two "reservoirs". Therefore the $V$-dependent low-frequency resistance observed in the inset of Fig. 4.7 reflects the revival of the Landauer-type transport. To see this behavior more clearly, we plot in Fig. 4.9 the product $G(i\omega_n \to 0)R(i\omega_n \to 0)$ for $K = 1/3$ as a function of $V$. In the strong barrier region, $G(0)$ is finite and equal to $[R(0)]^{-1}$, which is a familiar property of transport through a point contact. Upon decreasing $V$, however, $G(0)R(0)$ is suppressed since $G(0)$ decays to zero because of charging up, although $R(0) \to R_q$ is finite. Moreover, we see that the coherent region $G(0)R(0) = 0$ extends to larger $V$ upon lowering temperature. Finally, we determine the phase

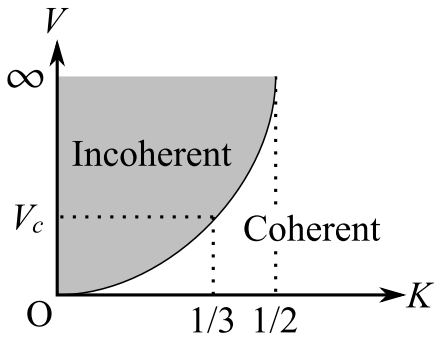


Figure 4.10: Schematic phase diagram in the degenerate case. $V_c$ denotes the critical backscattering strength for $K = 1/3$.

boundary of the coherent-incoherent transition by tracing the temperature dependence of the ratio $\tau_{RC}/\tau_{\rm coh} = R(0)C_\mu T$. The above discussion suggests that there exists a critical backscattering strength $V_c$, below which $\tau_{RC}/\tau_{\rm coh}$ decays to zero, while it diverges otherwise. (see Fig. 4.10). From the inset of Fig. 4.9, the critical value is estimated as $4V_c\tau_c \simeq 7$.

## 4.6 Summary

In this chapter, we have studied dynamic response of a mesoscopic capacitor in the presence of strong electron interactions. Unlike the prior theories based on mean field type approximations, we have employed the bosonization technique to take into account interactions exactly. By combining perturbation theory, renormalization group, and the PIMC simulation, we treat whole parameter range of dot-lead coupling. Our results show that the relaxation resistance for a dot connected to a Luttinger liquid is universal $R = h/(2e^2K)$ as long as interactions are sufficiently weak. Below $K < 1/2$, this resistance is governed by the strength of the dot-lead coupling: at the charge degeneracy point, there is a critical coupling strength, governed by a KT type phase transition, below which the dot acts as an incoherent reservoir and the low-frequency resistance exceeds the universal value. In this incoherent regime, the charge relaxation resistance cannot be defined anymore due to the divergence of $RC$ time. These behaviors are expected to be observed experimentally in the same setup as in Ref. [9], if a sufficiently high magnetic field $\sim$ 10 T is applied in order to realize the fractional quantum Hall effect at $\nu = 1/3$.

# Summary

In this thesis, we have investigated theoretically transport phenomena in mesoscopic systems based on numerical and analytical approaches. Our main goal is to reveal how the charge relaxation resistance in a mesoscopic capacitor, which is composed of a quantum dot and a lead, is affected by strong electron interactions. We have formulated the mesoscopic capacitor using the bosonization technique in order to treat exactly the interaction effects, which has been so far handled only approximately based on mean-field type methods in prior studies. The bosonized model is not only tractable analytically, but it has an expression suitable to numerical simulation based on the path-integral Monte Carlo (PIMC) method. In addition, the cluster algorithm recently developed by Werner and Troyer in the context of resistively shunted Josephson junctions [18] is extensible to our numerical approach, which makes it possible to analyze the nonperturbative region. In order to check the performance of the cluster algorithm, we have applied the PIMC method to the single impurity problem in a spinful Tomonaga-Luttinger liquid. The phase diagram we obtained at finite impurity strength has been compared with the results of renormalization group calculations in the weak and strong impurity limits [32, 33].

To establish the PIMC method in the Coulomb blockade regime, we have investigate the static properties of a large quantum dot with spinful electrons in Chap. 3. By measuring the capacitance of dot, we have confirmed that the capacitance at the degeneracy point diverges logarithmically with decreasing temperature for arbitrary tunneling between the dot and the lead. This phenomenon is a sign of the two-channel Kondo effect and has been predicted by Matveev based on the analytical calculations in the weak and strong tunneling limits [22, 23]. Our results are consistent with a prior study with numerical renormalization group by Lebanon *et al.* based on a tunneling model [64]. We have also confirmed that anisotropy between up and down spin channels due to the Zeeman effect blurs the divergence as analytically predicted by Le Hur [63].

In Chap. 4, which is the main part of this thesis, we have analyzed dynamic response of a mesoscopic capacitor using analytical calculations and the PIMC simulation. We have assumed spinless electrons and taken into account as two types

of interaction; short-range interactions described with the Luttinger parameter $K$ and long-range interactions leading to the charging energy $E_C$ in the quantum dot. In the weak barrier limit, where the dot and the lead are strongly connected, we have treated reflection strength $V$ as perturbation up to second order and shown that the charge relaxation resistance is quantized at $h/2Ke^2$ irrespective of $V$, the gate voltage, or the charging energy. We have also shown that the electrochemical capacitance $C_\mu$ can be expressed as a serial combination of two capacitances as in the self-consistent scattering theory by Büttiker *et al* [19]. An important difference is that the capacitance associated to $E_C$ displays Coulomb oscillation in our theory reflecting the exact treatment of electron interactions, while it does not in the latter. In the strong barrier limit $V \to \infty$, on the other hand, we have performed perturbative renormalization group and shown that, if $K < 1/2$ and $V$ is sufficiently large, the charge relaxation time $\tau_{RC}$ diverges faster than $T^{-1}$ as $T \to 0$ due to the Kosterlitz-Thouless transition. As a result, one observes Landauer-type dc resistance dependent on $V$, instead of the universal charge relaxation resistance. In the intermediate regime of $V$, we have applied the PIMC method to the present problem to confirm the above predictions. For this purpose, we have contrived a new scheme to measure the charge relaxation resistance in the PIMC method: Calculates the linear admittance $G(i\omega_n)$ and the electrochemical capacitance $C_\mu$ in the PIMC simulation and substitute them to

$$R(i\omega_n) = \frac{1}{G(i\omega_n)} - \frac{1}{\omega_n C_\mu}.$$

Then, the extrapolation $i\omega_n \to 0$ gives the quantized charge relaxation resistance $h/2Ke^2$ as long as the system lies in the normal phase. In the case of $K < 1/2$, we have numerically observed abrupt increase in $R(i\omega_n \to 0)$ upon increasing $V$. We stress that this behavior can be observed experimentally in fractional quantum Hall edges if the filling is equal to an inverse odd number and $|u| < T$.

# Outlooks

Finally, we mention some possible extensions of the present work.

- By performing the analytic continuation $i\omega_n \to \omega + i\delta$ numerically with, e.g., the padé approximation or the maximum extropy method, one can obtain the charge relaxation resistance at finite frequency. It is expected that $\omega$-dependence of the charge relaxation resistance is characterized by $K$, reflecting the orthogonality catastrophe.

- The Kosterlitz-Thouless (KT) transition discussed in Chap. 4 also occurs due to a noisy gate voltage. This situation can be realized by connecting the

gate to a transmission line with a finite impedance. Le Hur has discussed the KT transition in such a quantum dot system from the viewpoint of the Bose-Fermi Kondo model [70].

- Charge relaxation resistance in the Kondo regime can be investigated by extending the spinful model we have treated in Chap. 3 to a mesoscopic capacitor with finite size. The relation between the Kondo effect and spin-charge separation has been studied by Glazman *et al.* [71]

# Appendix A

# Chiral Luttinger liquid in a mesoscopic capacitor

In this appendix, we formulate the fractional quantum Hall edge state with filling $g$ realized along a mesoscopic capacitor in a perpendicular magnetic field. For simplicity, $g = 1/m$ with an odd number $m$ is assumed, which allows us to describe the edge state in terms of a chiral Luttinger liquid (CLL) [72, 73, 74]. We consider an edge state along a mesoscopic capacitor dipicted in Fig. A.1 and begin with the Euclidean action for the bulk CLL

$$S_0[\phi] = \frac{1}{4\pi g}\int \mathrm{d}x\mathrm{d}\tau(\partial_x\phi)(i\partial_\tau\phi + v\partial_x\phi). \tag{A.1}$$

In our notation, the electron density is given by $\rho = \partial_x\phi/2\pi$, and the field operator of an electron can be written in terms of the bosonic filed $\phi$ in Eq. (4.20) as

$$\Psi(x) \propto \exp\left[-i\theta(x) + i\phi(x)\right], \tag{A.2}$$

where $\theta(x)$ is the phase a quasiparticle gains in the range of $(-\infty, x]$, i.e., the sum of $k_F x$ and the Peierls phase. On the point contact, we take into account tunneling of a quasiparticle $e^*(= ge)$ between $x = x_1$ and $x = x_2$ with the tunneling matrix

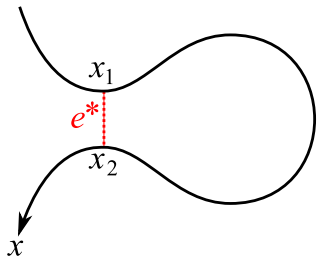


Figure A.1: A mesoscopic capacitor and a chiral Luttinger liquid running along its edge. Electrons in the dot region $x_1 \le x \le x_2$ is capacitively coupled to an oscillating gate voltage $V_g(t)$. A quasiparticle $e^* = ge$ tunnels between $x_1$ and $x_2$, where the two edges become closest.

element $\Gamma_0$. The action corresponding to this process is given by

$$S_V[\phi] = \Gamma_0 \int \mathrm{d}\tau[\Psi^\dagger(x_2,\tau)\Psi(x_1,\tau) + \mathrm{H.c.}] \tag{A.3}$$

$$= V \int \mathrm{d}\tau \cos[\theta + \{\phi(x_1,\tau) - \phi(x_2,\tau)\}], \tag{A.4}$$

where $V$ is a constant proportional to $\Gamma_0$ and $\theta \equiv \theta(x_2) - \theta(x_1)$. Moreover, we add the terms describing the charging effect and coupling between the gate voltage and the charges in the region $x_1 \le x \le x_2$;

$$S_C = \int \mathrm{d}\tau \left[\frac{1}{2C}\{Q(\tau)\}^2 + Q(\tau)V_g\right], \qquad Q(\tau) = \frac{e}{2\pi}[\phi(x_2,\tau) - \phi(x_1,\tau)]. \tag{A.5}$$

In the rest of this appendix, we derive an effective action from $S_0 + S_V + S_C$ and show that it is equivalent to Eq. (4.20).

## A.1 Effective action

The total action $S_0 + S_V + S_C$ is quadratic in $\phi$ except for $x = x_1$ and $x = x_2$. Thus we can derive an effective action by integrating out $\phi$ away from $x_1$ and $x_2$ in the path integral picture as descried bellow. To perform this integration, we first replace the $\phi$ in the argument of $S_V$ and $S_C$ with local fields $\phi_1$ and $\phi_2$ as

$$Z \propto \int \mathscr{D}\phi \mathscr{D}\phi_1 \mathscr{D}\phi_2 \mathscr{D}\lambda_1 \mathscr{D}\lambda_2 \mathrm{e}^{-S_0[\phi] - S_V[\phi_1,\phi_2] - S_C[\phi_1,\phi_2] - S_\lambda{}^{(1)}[\phi,\lambda_1,\lambda_2] - S_\lambda{}^{(2)}[\phi_1,\phi_2,\lambda_1,\lambda_2]}. \tag{A.6}$$

Here the auxiliary fields $\lambda_1$ and $\lambda_2$ has been introduced to relate $\phi_1$ and $\phi_2$ indirectly to $\phi$ through the additional actions

$$S_\lambda{}^{(1)}[\phi,\lambda_1,\lambda_2] = i \sum_{j=1,2} \int \mathrm{d}\tau \lambda_j(\tau)\phi(x_j,\tau), \tag{A.7}$$

$$S_\lambda{}^{(2)}[\phi_1,\phi_2,\lambda_1,\lambda_2] = -i \sum_{j=1,2} \int \mathrm{d}\tau \lambda_j(\tau)\phi_j(\tau). \tag{A.8}$$

Now the routine work to do is to perform the Gaussian integrations in $\phi, \lambda_1$ and $\lambda_2$, which appear in $S_0, S_\lambda{}^{(1)}$ and $S_\lambda{}^{(1)}$. So here we focus on these actions for a while and express them in the Fourier space;

$$\phi(x,\tau) = \frac{1}{L\beta} \sum_k \sum_{\omega_n} \tilde{\phi}(k,\omega_n)\mathrm{e}^{ikx - i\omega_n\tau}, \tag{A.9}$$

$$\phi_j(\tau) = \frac{1}{\beta}\sum_{\omega_n}\tilde{\phi}_j(\omega_n)\mathrm{e}^{-i\omega_n\tau}, \qquad \lambda_j(\tau) = \frac{1}{\beta}\sum_{\omega_n}\tilde{\lambda}_j(\omega_n)\mathrm{e}^{-i\omega_n\tau}, \tag{A.10}$$

$$S_0[\phi] = \frac{1}{4\pi g}\int \mathrm{d}x\mathrm{d}\tau\frac{1}{L^2\beta^2}\sum_{kq}\sum_{\omega_n\omega_m} k(i\omega_m - vq)\tilde{\phi}(k,\omega_n)\tilde{\phi}(q,\omega_m)\mathrm{e}^{i(k+q)x - i(\omega_n+\omega_m)\tau} \tag{A.11}$$

$$= \frac{1}{L\beta}\sum_{k(\neq 0)}\sum_{\omega_n}\frac{k(vk - i\omega_n)}{4\pi g}|\tilde{\phi}(k,\omega_n)|^2 \tag{A.12}$$

$$= \frac{1}{L\beta}\sum_{k(\neq 0)}\sum_{\omega_n} A_{kn}|\tilde{\phi}(k,\omega_n)|^2 \qquad \left(A_{kn} = \frac{k(vk - i\omega_n)}{4\pi g} = A_{-k,-n}\right), \tag{A.13}$$

$$S_\lambda{}^{(1)}[\phi,\lambda_1,\lambda_2] = i\sum_j\frac{1}{L\beta}\sum_k\sum_{\omega_n}\tilde{\lambda}_j{}^*(\omega_n)\tilde{\phi}(k,\omega_m)\mathrm{e}^{ikx_j}, \tag{A.14}$$

$$S_\lambda{}^{(2)}[\phi_1,\phi_2,\lambda_1,\lambda_2] = -i\sum_j\frac{1}{\beta}\sum_{\omega_n}\tilde{\lambda}_j{}^*(\omega_n)\tilde{\phi}_j(\omega_m). \tag{A.15}$$

For simplicity, we write only the part related to each integration in the followings. First, the Gaussian integral in $\phi$ can be calculated as

$$\int \mathscr{D}\phi\mathrm{e}^{-S_0[\phi]-S_\lambda{}^{(1)}[\phi,\lambda_1,\lambda_2]} \tag{A.16}$$

$$= \int \mathscr{D}\phi\exp\left[-\frac{1}{L\beta}\sum_{k(\neq 0)}\sum_{\omega_n}\left\{A_{kn}|\tilde{\phi}(k,\omega_n)|^2 + i\sum_j\tilde{\lambda}_j{}^*(\omega_n)\tilde{\phi}(k,\omega_n)\mathrm{e}^{ikx_j}\right\}\right] \tag{A.17}$$

$$\propto \exp\left[-\frac{1}{L\beta}\sum_{k(\neq 0)}\sum_{\omega_n}\frac{1}{4A_{kn}}|\tilde{\lambda}_1(\omega_n)\mathrm{e}^{ikx_1} + \tilde{\lambda}_2(\omega_n)\mathrm{e}^{ikx_2}|^2\right] \tag{A.18}$$

$$\begin{aligned}= \exp\Bigg[-\frac{1}{L\beta}\sum_{k(\neq 0)}\sum_{\omega_n}\frac{1}{4A_{kn}}&[|\tilde{\lambda}_1(\omega_n)|^2 + |\tilde{\lambda}_2(\omega_n)|^2 \\ &+ \{\lambda_1(\omega_n)\lambda_2{}^*(\omega_n) + \lambda_1{}^*(\omega_n)\lambda_2(\omega_n)\}\cos kL \\ &-i\{\lambda_1(\omega_n)\lambda_2{}^*(\omega_n) - \lambda_1{}^*(\omega_n)\lambda_2(\omega_n)\}\sin kL]\Bigg],\end{aligned} \tag{A.19}$$

and the summations over $k$ are estimated as

$$\frac{1}{L}\sum_{k(\neq 0)}\frac{1}{4A_{kn}} = \frac{2\pi vg}{L}\sum_{k>0}\frac{1}{v^2k^2 + {\omega_n}^2} \tag{A.20}$$

$$= \frac{g}{v}\int_0^\infty\frac{\mathrm{d}k}{k^2 + (\omega_n/v)^2} = \frac{\pi g}{2|\omega_n|}, \tag{A.21}$$

$$\frac{1}{L}\sum_{k(\neq 0)}\frac{\cos kL}{4A_{kn}} = \frac{2\pi vg}{L}\sum_{k>0}\frac{\cos kL}{v^2k^2 + {\omega_n}^2} \tag{A.22}$$

$$= \frac{g}{v}\int_0^\infty \mathrm{d}k \frac{\cos kL}{k^2+(\omega_n/v)^2} = \frac{\pi g}{2|\omega_n|}\mathrm{e}^{-|\omega_n|L/v}, \tag{A.23}$$

$$\frac{1}{L}\sum_{k(\neq 0)} \frac{\sin kL}{4A_{kn}} = \frac{2\pi i g\omega_n}{Lv^2}\sum_{k>0}\frac{\sin kL}{k[k^2+(\omega_n/v)^2]} \tag{A.24}$$

$$= \frac{ig\omega_n}{v^2}\int_0^\infty \mathrm{d}k \frac{\sin kL}{k[k^2+(\omega_n/v)^2]} = \frac{i\pi g}{2\omega_n}(1-\mathrm{e}^{-|\omega_n|L/v}). \tag{A.25}$$

Then, the path integral over $\phi$ is summarized as

$$\therefore \int \mathscr{D}\phi \mathrm{e}^{-S_0[\phi]-S_\lambda{}^{(1)}[\phi,\lambda_1,\lambda_2]} \tag{A.26}$$

$$= \exp\Bigg[-\frac{1}{\beta}\sum_{\omega_n}\frac{\pi g}{2|\omega_n|}\Big\{|\tilde{\lambda}_1(\omega_n)|^2+|\tilde{\lambda}_2(\omega_n)|^2 + \{\lambda_1(\omega_n)\lambda_2{}^*(\omega_n)+\lambda_1{}^*(\omega_n)\lambda_2(\omega_n)\}\mathrm{e}^{-|\omega_n|L/v} + \{\lambda_1(\omega_n)\lambda_2{}^*(\omega_n)-\lambda_1{}^*(\omega_n)\lambda_2(\omega_n)\}\mathrm{sgn}(\omega_n)(1-\mathrm{e}^{-|\omega_n|L/v})\Big\}\Bigg] \tag{A.27}$$

$$= \exp\left[-\frac{1}{\beta}\sum_{\omega_n}\frac{\pi g}{2|\omega_n|}\{|\tilde{\lambda}_1(\omega_n)|^2+|\tilde{\lambda}_2(\omega_n)|^2+2B(\omega_n)\tilde{\lambda}_1(\omega_n)\tilde{\lambda}_2{}^*(\omega_n)\}\right], \tag{A.28}$$

where

$$B(\omega_n) = \mathrm{e}^{-|\omega_n|L/v}+\mathrm{sgn}(\omega_n)(1-\mathrm{e}^{-|\omega_n|L/v}) \quad \left[\overset{L\to\infty}{\longrightarrow} \mathrm{sgn}(\omega_n)\right]. \tag{A.29}$$

Next, the Gaussian integral in $\lambda_1$ is performed in the same way;

$$\int \mathscr{D}\lambda_1[\mathrm{Eq}\,(A.28)]\exp\left[\frac{i}{\beta}\sum_{\omega_n}\tilde{\phi}_1{}^*(\omega_n)\tilde{\lambda}_1(\omega_n)\right] \tag{A.30}$$

$$= \int \mathscr{D}\lambda_1 \exp\Bigg[-\frac{1}{\beta}\sum_{\omega_n}\frac{\pi g}{2|\omega_n|}\{|\tilde{\lambda}_1(\omega_n)|^2+|\tilde{\lambda}_2(\omega_n)|^2\} - \frac{1}{\beta}\sum_{\omega_n}\left\{\frac{\pi g}{|\omega_n|}B(\omega_n)\tilde{\lambda}_2{}^*(\omega_n)-i\tilde{\phi}_1{}^*(\omega_n)\right\}\tilde{\lambda}_1(\omega_n)\Bigg] \tag{A.31}$$

$$= \exp\Bigg[-\frac{1}{\beta}\sum_{\omega_n}\frac{\pi g}{2|\omega_n|}|\tilde{\lambda}_2(\omega_n)|^2+\sum_{\omega_n}\frac{|\omega_n|}{2\pi g\beta}\left\{\frac{\pi g}{|\omega_n|}B(\omega_n)\tilde{\lambda}_2{}^*(\omega_n)-i\tilde{\phi}_1{}^*(\omega_n)\right\} \times\left\{\frac{\pi g}{|\omega_n|}B(-\omega_n)\tilde{\lambda}_2(\omega_n)-i\tilde{\phi}_1(\omega_n)\right\}\Bigg] \tag{A.32}$$

$$= \exp\Bigg[-\frac{1}{\beta}\sum_{\omega_n}\frac{\pi g}{2|\omega_n|}\{1-B(\omega_n)B(-\omega_n)\}|\tilde{\lambda}_2(\omega_n)|^2$$

$$-\frac{i}{\beta}\sum_{\omega_n} B(-\omega_n)\tilde{\phi}_1{}^*(\omega_n)\tilde{\lambda}_2(\omega_n) - \sum_{\omega_n}\frac{|\omega_n|}{2\pi g\beta}|\tilde{\phi}_1(\omega_n)|^2\Bigg]. \tag{A.33}$$

Finally, the Gaussian integral in $\lambda_2$ leads to the Boltzmann factor in $\phi_1$ and $\phi_2$

$$\int \mathscr{D}\lambda_2[\text{Eq. } (A.33)]\exp\left[\frac{i}{\beta}\sum_{\omega_n}\tilde{\phi}_2{}^*(\omega_n)\tilde{\lambda}_2(\omega_n)\right] \tag{A.34}$$

$$\begin{aligned}
&= \int \mathscr{D}\lambda_2 \exp\Bigg[-\frac{1}{\beta}\sum_{\omega_n}\frac{\pi g}{2|\omega_n|}\{1 - B(\omega_n)B(-\omega_n)\}|\tilde{\lambda}_2(\omega_n)|^2 \\
&\qquad - \frac{i}{\beta}\sum_{\omega_n}\{B(-\omega_n)\tilde{\phi}_1{}^*(\omega_n) - \tilde{\phi}_2{}^*(\omega_n)\}\tilde{\lambda}_2(\omega_n) \\
&\qquad -\frac{1}{2\pi g\beta}\sum_{\omega_n}|\omega_n||\tilde{\phi}_1(\omega_n)|^2\Bigg]
\end{aligned} \tag{A.35}$$

$$\begin{aligned}
&= \exp\Bigg[-\sum_{\omega_n}\frac{|\omega_n|}{2\pi g\beta}\frac{1}{1 - B(\omega_n)B(-\omega_n)} \\
&\qquad \times\left\{B(-\omega_n)\tilde{\phi}_1{}^*(\omega_n) - \tilde{\phi}_2{}^*(\omega_n)\right\}\left\{B(\omega_n)\tilde{\phi}_1(\omega_n) - \tilde{\phi}_2(\omega_n)\right\} \\
&\qquad -\frac{1}{2\pi g\beta}\sum_{\omega_n}|\omega_n||\tilde{\phi}_1(\omega_n)|^2\Bigg]
\end{aligned} \tag{A.36}$$

$$\begin{aligned}
&= \exp\Bigg[-\frac{1}{2\pi g\beta}\sum_{\omega_n}\frac{|\omega_n|}{1 - B(\omega_n)B(-\omega_n)}\{|\tilde{\phi}_1(\omega_n)|^2 \\
&\qquad -2B(-\omega_n)\tilde{\phi}_1{}^*(\omega_n)\tilde{\phi}_2(\omega_n) + |\tilde{\phi}_2(\omega_n)|^2\}\Bigg]
\end{aligned} \tag{A.37}$$

Recall the fact that the tunneling term $S_V$ and the charging term $S_C$ couple only to the asymmetric combination of the local fields, i.e., $\phi_1 - \phi_2$, which means the symmetric combination $\phi_1 + \phi_2$ can be also integrated out. To see this, we redefine new bosonic fields and perform the last Gaussian integral in the symmetric field;

$$\phi_1 = \phi_s + \phi_a, \quad \phi_2 = \phi_s - \phi_a, \quad 2\phi_a = \phi_1 - \phi_2, \quad 2\phi_s = \phi_1 + \phi_2, \tag{A.38}$$

$$|\tilde{\phi}_2(\omega_n)|^2 + |\tilde{\phi}_2(\omega_n)|^2 = 2[|\tilde{\phi}_s(\omega_n)|^2 + |\tilde{\phi}_a(\omega_n)|^2], \tag{A.39}$$

$$\tilde{\phi}_1(\omega_n)\tilde{\phi}_2{}^*(\omega_n) = [\tilde{\phi}_s(\omega_n) + \tilde{\phi}_a(\omega_n)][\tilde{\phi}_s{}^*(\omega_n) - \tilde{\phi}_a{}^*(\omega_n)] \tag{A.40}$$

$$= |\tilde{\phi}_s(\omega_n)|^2 + \tilde{\phi}_s{}^*(\omega_n)\tilde{\phi}_a(\omega_n) - \tilde{\phi}_s(\omega_n)\tilde{\phi}_a{}^*(\omega_n) - |\tilde{\phi}_a(\omega_n)|^2, \tag{A.41}$$

$$\tilde{\phi}_1{}^*(\omega_n)\tilde{\phi}_2(\omega_n) = [\tilde{\phi}_s{}^*(\omega_n) + \tilde{\phi}_a{}^*(\omega_n)][\tilde{\phi}_s(\omega_n) - \tilde{\phi}_a(\omega_n)] \tag{A.42}$$

$$= |\tilde{\phi}_s(\omega_n)|^2 - \tilde{\phi}_s{}^*(\omega_n)\tilde{\phi}_a(\omega_n) + \tilde{\phi}_s(\omega_n)\tilde{\phi}_a{}^*(\omega_n) - |\tilde{\phi}_a(\omega_n)|^2, \tag{A.43}$$

$$Z = \int \mathscr{D}\phi_s\mathscr{D}\phi_a \exp\left[-\frac{1}{2\pi g\beta}\sum_{\omega_n}\frac{|\omega_n|}{1 - B(\omega_n)B(-\omega_n)}\right. \tag{A.44}$$

$$\times [\{2 - B(\omega_n) - B(-\omega_n)\}|\tilde{\phi}_s(\omega_n)|^2 + \{2 + B(\omega_n) + B(-\omega_n)\}|\tilde{\phi}_a(\omega_n)|^2 \tag{A.45}$$

$$+ 2\{B(\omega_n) - B(-\omega_n)\}\tilde{\phi}_a{}^*(\omega_n)\tilde{\phi}_s(\omega_n)]\Big] \mathrm{e}^{-S_V[\phi_a]-S_C[\phi_a]} \tag{A.46}$$

$$= \int \mathscr{D}\phi_a \exp\left[-\frac{1}{2\pi g\beta}\sum_{\omega_n}\frac{2 + B(\omega_n) + B(-\omega_n)}{1 - B(\omega_n)B(-\omega_n)}|\omega_n||\tilde{\phi}_a(\omega_n)|^2\right. \tag{A.47}$$

$$\left. -\frac{1}{2\pi g\beta}\sum_{\omega_n}\frac{\{B(\omega_n) - B(-\omega_n)\}^2|\omega_n||\tilde{\phi}_a(\omega_n)|^2}{\{2 - B(\omega_n) - B(-\omega_n)\}\{1 - B(\omega_n)B(-\omega_n)\}}\right] \mathrm{e}^{-S_V[\phi_a]-S_C[\phi_a]} \tag{A.48}$$

$$= \int \mathscr{D}\phi_a \exp\left[-\frac{1}{\pi g\beta}\sum_{\omega_n}\frac{2}{2 - B(\omega_n)B(-\omega_n)}|\omega_n||\tilde{\phi}_a(\omega_n)|^2\right] \mathrm{e}^{-S_V[\phi_a]-S_C[\phi_a]} \tag{A.49}$$

$$= \int \mathscr{D}\phi_a \exp\left[-\frac{1}{\pi g\beta}\sum_{\omega_n}\frac{|\omega_n|}{1 - \mathrm{e}^{-|\omega_n|L/v}}|\tilde{\phi}_a(\omega_n)|^2\right] \mathrm{e}^{-S_V[\phi_a]-S_C[\phi_a]}. \tag{A.50}$$

Then we arrive at the effective action in terms of $\phi_a$

$$S_{\text{eff}} = \frac{1}{\pi g\beta}\sum_{\omega_n}\frac{|\omega_n|}{1 - \mathrm{e}^{-|\omega_n|L/v}}|\tilde{\phi}_a(\omega_n)|^2 + V\int \mathrm{d}\tau \cos[\theta + 2\phi_a(\tau)]$$

$$+ \int \mathrm{d}\tau\left[\frac{1}{\pi^2}\frac{e^2}{2C}\{\phi_a(\tau)\}^2 - \frac{eV_g}{\pi}\phi_a(\tau)\right], \tag{A.51}$$

which is clearly equivalent to the effective action in the non-chiral case [see Eq. (4.20)].

# Bibliography


[1] S. Datta, *Electronic Transport in Mesoscopic Systems* (Cambridge University Press, Cambridge, 1995).

[2] Y. Imry, *Introduction to Mesoscopic Physics*, 2nd ed. (Oxford Univ Press, Oxford, 2008).

[3] D. K. Ferry, S. M. Goodnick, and J. Bird, *Transport in Nanostructures*, 2nd ed. (Cambridge University Press, Cambridge, 2009).

[4] *Quantum Entanglement and Information Processing, Volume Session LXXIX: Lecture Notes of the Les Houches Summer School 2003*, edited by D. Esteve, J.-M. Raimond, and J. Dalibard (Elsevier Science, Amsterdam, 2004).

[5] M. A. Nielsen and I. L. Chuang, *Quantum Computation and Quantum Information* (Cambridge University Press, Cambridge, 2000).

[6] T. Hayashi *et al.*, Phys. Rev. Lett. **91**, 226804 (2003).

[7] G. Shinkai, T. Hayashi, T. Ota, and T. Fujisawa, Phys. Rev. Lett. **103**, 56802 (2009).

[8] G. Feve *et al.*, Science **316**, 1169 (2007).

[9] J. Gabelli *et al.*, Science **313**, 499 (2006).

[10] R. Landauer, IBM J. Res. Dev. **1**, 233 (1957).

[11] R. Landauer, Phil. Mag. **21**, 863 (1970).

[12] M. Büttiker, Phys. Rev. Lett. **57**, 1761 (1986).

[13] *Single Charge Tunneling: Coulomb Blockade Phenomena in Nanostructures*, edited by H. Grabert and M. H. Devoret (Springer, New York, 1992).

[14] A. O. Gogolin, A. A. Nersesyan, and A. M. Tsvelik, *Bosonization and Strongly Correlated Systems* (Cambridge University Press, Cambridge, 1999).

[15] H. J. Schulz, G. Cuniberti, and P. Pieri, in *Field Theories for Low-Dimensional Condensed Matter Systems: Spin Systems and Strongly Correlated Electrons*, edited by G. Morandi, P. Sodano, A. Tagliacozzo, and V. Tognetti (Springer, New York, 2000).

[16] A. M. Chang, Rev. Mod. Phys. **75**, 1449 (2003).

[17] T. Giamarchi, *Quantum Physics in One Dimension* (Oxford University Press, Oxford, 2004).

[18] P. Werner and M. Troyer, Phys. Rev. Lett. **95**, 60201 (2005).

[19] M. Büttiker, H. Thomas, and A. Pretre, Phys. Lett. A **180**, 364 (1993).

[20] A. Prêtre, H. Thomas, and M. Büttiker, Phys. Rev. B **54**, 8130 (1996).

[21] S. E. Nigg, R. López, and M. Büttiker, Phys. Rev. Lett. **97**, 206804 (2006).

[22] K. A. Matveev, Zh. Eksp. Teor. Fiz. **99**, 1598 (1991).

[23] K. A. Matveev, Phys. Rev. B **51**, 1743 (1995).

[24] F. Milliken, Sol. Stat. Commun. **97**, 309 (1996).

[25] A. M. Chang, L. N. Pfeiffer, and K. W. West, Phys. Rev. Lett. **77**, 2538 (1996).

[26] M. Grayson *et al.*, Phys. Rev. Lett. **80**, 1062 (1998).

[27] M. Bockrath *et al.*, Nature **397**, 598 (1999).

[28] H. Ishii *et al.*, Nature **426**, 540 (2003).

[29] B. Gao *et al.*, Phys. Rev. Lett. **92**, 216804 (2004).

[30] D. L. Maslov and M. Stone, Phys. Rev. B **52**, R5539 (1995).

[31] C. L. Kane and M. P. A. Fisher, Phys. Rev. Lett. **68**, 1220 (1992).

[32] C. L. Kane and M. P. A. Fisher, Phys. Rev. B **46**, 15233 (1992).

[33] A. Furusaki and N. Nagaosa, Phys. Rev. B **47**, 3827 (1993).

[34] A. Furusaki and N. Nagaosa, Phys. Rev. B **47**, 4631 (1993).

[35] M. P. A. Fisher and W. Zwerger, Phys. Rev. B **32**, 6190 (1985).

[36] K. Moon *et al.*, Phys. Rev. Lett. **71**, 4381 (1993).

[37] P. Fendley, A. W. W. Ludwig, and H. Saleur, Phys. Rev. Lett. **74**, 3005 (1995).

[38] D. V. Averin and K. K. Likharev, in *Mesoscopic Phenomena in Solids*, edited by B. A. *et al*. (Elsevier, Amsterdam, 1991), p. 173.

[39] J. Kondo, Prog. Theor. Phys. **32**, 37 (1964).

[40] A. C. Hewson, *The Kondo Problem to Heavy Fermions* (Cambridge University Press, Cambridge, 1993).

[41] T. K. Ng and P. A. Lee, Phys. Rev. Lett. **61**, 1768 (1988).

[42] L. I. Glazman and M. É. Raĭkh, JETP Lett. **47**, 452 (1988).

[43] D. Goldhaber-Gordon *et al.*, Nature **391**, 156 (1998).

[44] W. G. van der Wiel *et al.*, Science **289**, 2105 (2000).

[45] P. W. Anderson, J. Phys. C **3**, 2436 (1970).

[46] P. W. Anderson, G. Yuval, and D. R. Hamann, Phys. Rev. B **1**, 4464 (1970).

[47] P. W. Anderson and G. Yuval, J. Phys. C **4**, 607 (1971).

[48] A. J. Bray and M. A. Moore, Phys. Rev. Lett. **49**, 1545 (1982).

[49] S. Chakravarty, Phys. Rev. Lett. **49**, 681 (1982).

[50] A. J. Leggett *et al.*, Rev. Mod. Phys. **59**, 1 (1987).

[51] S. Chakravarty and J. Rudnick, Phys. Rev. Lett. **75**, 501 (1995).

[52] K. Völker, Phys. Rev. B **58**, 1862 (1998).

[53] T. A. Costi and C. Kieffer, Phys. Rev. Lett. **76**, 1683 (1996).

[54] T. A. Costi, Phys. Rev. Lett. **80**, 1038 (1998).

[55] F. Lesage, H. Saleur, and S. Skorik, Phys. Rev. Lett. **76**, 3388 (1996).

[56] L. Capriotti *et al.*, Phys. Rev. Lett. **91**, 247004 (2003).

[57] L. Capriotti *et al.*, Phys. Rev. Lett. **94**, 157001 (2005).

[58] R. H. Swendsen and J.-S. Wang, Phys. Rev. Lett. **58**, 86 (1987).

[59] E. Luijten and H. Blöte, Int. J. Mod. Phys. C **6**, 359 (1995).

[60] Y. Hamamoto, K.-I. Imura, and T. Kato, Phys. Rev. B **77**, 165402 (2008).

[61] P. Werner and M. Troyer, Prog. Theor. Phys. Suppl. **160**, 395 (2005).

[62] Y. Hamamoto and T. Kato, Phys. Rev. B **77**, 245325 (2008).

[63] K. Le Hur, Phys. Rev. B **64**, 161302 (2001).

[64] E. Lebanon, A. Schiller, and F. B. Anders, Phys. Rev. B **68**, 041311 (2003).

[65] D. L. Cox and A. Zawadowski, *Exotic Kondo Effects in Metals: Magnetic Ions in a Crystalline Electric Field and Tunnelling Centres* (Taylor & Francis, London, 1999).

[66] P. D. Sacramento and P. Schlottmann, Phys. Lett. A **142**, 245 (1989).

[67] Y. Hamamoto, T. Jonckheere, T. Kato, and T. Martin, arXiv:0911.4101 (unpublished).

[68] M. Fabrizio and A. O. Gogolin, Phys. Rev. B **51**, 17827 (1995).

[69] A. Furusaki and K. A. Matveev, Phys. Rev. Lett. **88**, 226404 (2002).

[70] K. Le Hur, Phys. Rev. Lett. **92**, 196804 (2004).

[71] L. I. Glazman, F. W. J. Hekking, and A. I. Larkin, Phys. Rev. Lett. **83**, 1830 (1999).

[72] X. G. Wen, Phys. Rev. Lett. **64**, 2206 (1990).

[73] X. G. Wen, Phys. Rev. B **43**, 11025 (1991).

[74] X.-G. Wen, Phys. Rev. B **44**, 5708 (1991).